

## Studies of Gauge Boson Pair Production and Trilinear Couplings

S. Abachi,<sup>14</sup> B. Abbott,<sup>28</sup> M. Abolins,<sup>25</sup> B.S. Acharya,<sup>43</sup> I. Adam,<sup>12</sup> D.L. Adams,<sup>37</sup> M. Adams,<sup>17</sup> S. Ahn,<sup>14</sup> H. Aihara,<sup>22</sup> G.A. Alves,<sup>10</sup> E. Amidi,<sup>29</sup> N. Amos,<sup>24</sup> E.W. Anderson,<sup>19</sup> R. Astur,<sup>42</sup> M.M. Baarmand,<sup>42</sup> A. Baden,<sup>23</sup> V. Balamurali,<sup>32</sup> J. Balderston,<sup>16</sup> B. Baldin,<sup>14</sup> S. Banerjee,<sup>43</sup> J. Bantly,<sup>5</sup> J.F. Bartlett,<sup>14</sup> K. Bazizi,<sup>39</sup> A. Belyaev,<sup>26</sup> S.B. Beri,<sup>34</sup> I. Bertram,<sup>31</sup> V.A. Bezzubov,<sup>35</sup> P.C. Bhat,<sup>14</sup> V. Bhatnagar,<sup>34</sup> M. Bhattacharjee,<sup>13</sup> N. Biswas,<sup>32</sup> G. Blazey,<sup>30</sup> S. Blessing,<sup>15</sup> P. Bloom,<sup>7</sup> A. Boehnlein,<sup>14</sup> N.I. Bojko,<sup>35</sup> F. Borchering,<sup>14</sup> J. Borders,<sup>39</sup> C. Boswell,<sup>9</sup> A. Brandt,<sup>14</sup> R. Brock,<sup>25</sup> A. Bross,<sup>14</sup> D. Buchholz,<sup>31</sup> V.S. Burtovoi,<sup>35</sup> J.M. Butler,<sup>3</sup> W. Carvalho,<sup>10</sup> D. Casey,<sup>39</sup> H. Castilla-Valdez,<sup>11</sup> D. Chakraborty,<sup>42</sup> S.-M. Chang,<sup>29</sup> S.V. Chekulaev,<sup>35</sup> L.-P. Chen,<sup>22</sup> W. Chen,<sup>42</sup> S. Choi,<sup>41</sup> S. Chopra,<sup>9</sup> B.C. Choudhary,<sup>9</sup> J.H. Christenson,<sup>14</sup> M. Chung,<sup>17</sup> D. Claes,<sup>27</sup> A.R. Clark,<sup>22</sup> W.G. Cobau,<sup>23</sup> J. Cochran,<sup>9</sup> W.E. Cooper,<sup>14</sup> C. Cretsinger,<sup>39</sup> D. Cullen-Vidal,<sup>5</sup> M.A.C. Cummings,<sup>16</sup> D. Cutts,<sup>5</sup> O.I. Dahl,<sup>22</sup> K. Davis,<sup>2</sup> K. De,<sup>44</sup> K. Del Signore,<sup>24</sup> M. Demarteau,<sup>14</sup> D. Denisov,<sup>14</sup> S.P. Denisov,<sup>35</sup> H.T. Diehl,<sup>14</sup> M. Diesburg,<sup>14</sup> G. Di Loreto,<sup>25</sup> P. Draper,<sup>44</sup> J. Drinkard,<sup>8</sup> Y. Ducros,<sup>40</sup> L.V. Dudko,<sup>26</sup> S.R. Dugad,<sup>43</sup> D. Edmunds,<sup>25</sup> J. Ellison,<sup>9</sup> V.D. Elvira,<sup>42</sup> R. Engelmann,<sup>42</sup> S. Eno,<sup>23</sup> G. Eppley,<sup>37</sup> P. Ermolov,<sup>26</sup> O.V. Eroshin,<sup>35</sup> V.N. Evdokimov,<sup>35</sup> T. Fahland,<sup>8</sup> M. Fatyga,<sup>4</sup> M.K. Fatyga,<sup>39</sup> J. Featherly,<sup>4</sup> S. Feher,<sup>14</sup> D. Fein,<sup>2</sup> T. Ferbel,<sup>39</sup> G. Finocchiaro,<sup>42</sup> H.E. Fisk,<sup>14</sup> Y. Fisyak,<sup>7</sup> E. Flattum,<sup>25</sup> G.E. Forden,<sup>2</sup> M. Fortner,<sup>30</sup> K.C. Frame,<sup>25</sup> S. Fuess,<sup>14</sup> E. Gallas,<sup>44</sup> A.N. Galyaev,<sup>35</sup> P. Gartung,<sup>9</sup> T.L. Geld,<sup>25</sup> R.J. Genik II,<sup>25</sup> K. Genser,<sup>14</sup> C.E. Gerber,<sup>14</sup> B. Gibbard,<sup>4</sup> S. Glenn,<sup>7</sup> B. Gobbi,<sup>31</sup> M. Goforth,<sup>15</sup> A. Goldschmidt,<sup>22</sup> B. Gómez,<sup>1</sup> G. Gómez,<sup>23</sup> P.I. Goncharov,<sup>35</sup> J.L. González Solís,<sup>11</sup> H. Gordon,<sup>4</sup> L.T. Goss,<sup>45</sup> A. Goussiou,<sup>42</sup> N. Graf,<sup>4</sup> P.D. Grannis,<sup>42</sup> D.R. Green,<sup>14</sup> J. Green,<sup>30</sup> H. Greenlee,<sup>14</sup> G. Grim,<sup>7</sup> S. Grinstein,<sup>6</sup> N. Grossman,<sup>14</sup> P. Grudberg,<sup>22</sup> S. Grünendahl,<sup>39</sup> G. Guglielmo,<sup>33</sup> J.A. Guida,<sup>2</sup> J.M. Guida,<sup>5</sup> A. Gupta,<sup>43</sup> S.N. Gurzhev,<sup>35</sup> P. Gutierrez,<sup>33</sup> Y.E. Gutnikov,<sup>35</sup> N.J. Hadley,<sup>23</sup> H. Haggerty,<sup>14</sup> S. Hagopian,<sup>15</sup> V. Hagopian,<sup>15</sup> K.S. Hahn,<sup>39</sup> R.E. Hall,<sup>8</sup> S. Hansen,<sup>14</sup> J.M. Hauptman,<sup>19</sup> D. Hedin,<sup>30</sup> A.P. Heinson,<sup>9</sup> U. Heintz,<sup>14</sup> R. Hernández-Montoya,<sup>11</sup> T. Heuring,<sup>15</sup> R. Hirosky,<sup>15</sup> J.D. Hobbs,<sup>14</sup> B. Hoeneisen,<sup>1,†</sup> J.S. Hoftun,<sup>5</sup> F. Hsieh,<sup>24</sup> Ting Hu,<sup>18</sup> Tong Hu,<sup>18</sup> T. Huehn,<sup>9</sup> A.S. Ito,<sup>14</sup> E. James,<sup>2</sup> J. Jaques,<sup>32</sup> S.A. Jerger,<sup>25</sup> R. Jesik,<sup>18</sup> J.Z.-Y. Jiang,<sup>42</sup> T. Joffe-Minor,<sup>31</sup> H. Johari,<sup>29</sup> K. Johns,<sup>2</sup> M. Johnson,<sup>14</sup> A. Jonckheere,<sup>14</sup> M. Jones,<sup>16</sup> H. Jöstlein,<sup>14</sup> S.Y. Jun,<sup>31</sup> C.K. Jung,<sup>42</sup> S. Kahn,<sup>4</sup> G. Kalbfleisch,<sup>33</sup> J.S. Kang,<sup>20</sup> R. Kehoe,<sup>32</sup> M.L. Kelly,<sup>32</sup> C.L. Kim,<sup>20</sup> S.K. Kim,<sup>41</sup> A. Klatchko,<sup>15</sup> B. Klima,<sup>14</sup> C. Klopfenstein,<sup>7</sup> V.I. Klyukhin,<sup>35</sup> V.I. Kochetkov,<sup>35</sup> J.M. Kohli,<sup>34</sup> D. Koltick,<sup>36</sup> A.V. Kostritskiy,<sup>35</sup> J. Kotcher,<sup>4</sup> A.V. Kotwal,<sup>12</sup> J. Kourlas,<sup>28</sup> A.V. Kozelov,<sup>35</sup> E.A. Kozlovski,<sup>35</sup> J. Krane,<sup>27</sup> M.R. Krishnaswamy,<sup>43</sup> S. Krzywdzinski,<sup>14</sup> S. Kunori,<sup>23</sup> S. Lami,<sup>42</sup> H. Lan,<sup>14,\*</sup> R. Lander,<sup>7</sup> F. Landry,<sup>25</sup> G. Landsberg,<sup>14</sup> B. Lauer,<sup>19</sup> A. Leflat,<sup>26</sup> H. Li,<sup>42</sup> J. Li,<sup>44</sup> Q.Z. Li-Demarteau,<sup>14</sup> J.G.R. Lima,<sup>38</sup> D. Lincoln,<sup>24</sup> S.L. Linn,<sup>15</sup> J. Linnemann,<sup>25</sup> R. Lipton,<sup>14</sup> Q. Liu,<sup>14,\*</sup> Y.C. Liu,<sup>31</sup> F. Lobkowicz,<sup>39</sup> S.C. Loken,<sup>22</sup> S. Lökös,<sup>42</sup> L. Lueking,<sup>14</sup> A.L. Lyon,<sup>23</sup> A.K.A. Maciel,<sup>10</sup> R.J. Madaras,<sup>22</sup> R. Madden,<sup>15</sup> L. Magaña-Mendoza,<sup>11</sup> S. Mani,<sup>7</sup> H.S. Mao,<sup>14,\*</sup> R. Markeloff,<sup>30</sup> L. Markosky,<sup>2</sup> T. Marshall,<sup>18</sup> M.I. Martin,<sup>14</sup> K.M. Mauritz,<sup>19</sup> B. May,<sup>31</sup> A.A. Mayorov,<sup>35</sup> R. McCarthy,<sup>42</sup> J. McDonald,<sup>15</sup> T. McKibben,<sup>17</sup> J. McKinley,<sup>25</sup> T. McMahon,<sup>33</sup> H.L. Melanson,<sup>14</sup> M. Merkin,<sup>26</sup> K.W. Merritt,<sup>14</sup> H. Miettinen,<sup>37</sup> A. Mincer,<sup>28</sup> J.M. de Miranda,<sup>10</sup> C.S. Mishra,<sup>14</sup> N. Mokhov,<sup>14</sup> N.K. Mondal,<sup>43</sup> H.E. Montgomery,<sup>14</sup> P. Mooney,<sup>1</sup> H. da Motta,<sup>10</sup> C. Murphy,<sup>17</sup> F. Nang,<sup>2</sup> M. Narain,<sup>14</sup> V.S. Narasimham,<sup>43</sup> A. Narayanan,<sup>2</sup> H.A. Neal,<sup>24</sup> J.P. Negret,<sup>1</sup> P. Nemethy,<sup>28</sup> D. Nešić,<sup>5</sup> M. Nicola,<sup>10</sup> D. Norman,<sup>45</sup> L. Oesch,<sup>24</sup> V. Oguri,<sup>38</sup> E. Oltman,<sup>22</sup> N. Oshima,<sup>14</sup> D. Owen,<sup>25</sup> P. Padley,<sup>37</sup> M. Pang,<sup>19</sup> A. Para,<sup>14</sup> Y.M. Park,<sup>21</sup> R. Partridge,<sup>5</sup> N. Parua,<sup>43</sup> M. Paterno,<sup>39</sup> J. Perkins,<sup>44</sup> M. Peters,<sup>16</sup> R. Piegaia,<sup>6</sup> H. Piekarz,<sup>15</sup> Y. Pischalnikov,<sup>36</sup> V.M. Podstavkov,<sup>35</sup> B.G. Pope,<sup>25</sup> H.B. Prosper,<sup>15</sup> S. Protopopescu,<sup>4</sup> D. Pušeljčić,<sup>22</sup> J. Qian,<sup>24</sup> P.Z. Quintas,<sup>14</sup> R. Raja,<sup>14</sup> S. Rajagopalan,<sup>4</sup> O. Ramirez,<sup>17</sup> P.A. Rapidis,<sup>14</sup> L. Rasmussen,<sup>42</sup> S. Reucroft,<sup>29</sup> M. Rijssenbeek,<sup>42</sup> T. Rockwell,<sup>25</sup> N.A. Roe,<sup>22</sup> P. Rubinov,<sup>31</sup> R. Ruchti,<sup>32</sup> J. Rutherford,<sup>2</sup> A. Sánchez-Hernández,<sup>11</sup> A. Santoro,<sup>10</sup> L. Sawyer,<sup>44</sup> R.D. Schamberger,<sup>42</sup> H. Schellman,<sup>31</sup> J. Sculli,<sup>28</sup> E. Shabalina,<sup>26</sup> C. Shaffer,<sup>15</sup> H.C. Shankar,<sup>43</sup> R.K. Shivpuri,<sup>13</sup> M. Shupe,<sup>2</sup> H. Singh,<sup>9</sup> J.B. Singh,<sup>34</sup> V. Sirotenko,<sup>30</sup> W. Smart,<sup>14</sup> A. Smith,<sup>2</sup> R.P. Smith,<sup>14</sup> R. Snihur,<sup>31</sup> G.R. Snow,<sup>27</sup> J. Snow,<sup>33</sup> S. Snyder,<sup>4</sup> J. Solomon,<sup>17</sup> P.M. Sood,<sup>34</sup> M. Sosebee,<sup>44</sup> N. Sotnikova,<sup>26</sup> M. Souza,<sup>10</sup> A.L. Spadafora,<sup>22</sup> R.W. Stephens,<sup>44</sup> M.L. Stevenson,<sup>22</sup> D. Stewart,<sup>24</sup> D.A. Stoianova,<sup>35</sup> D. Stoker,<sup>8</sup> M. Strauss,<sup>33</sup> K. Streets,<sup>28</sup> M. Strovink,<sup>22</sup> A. Sznajder,<sup>10</sup> P. Tamburello,<sup>23</sup> J. Tarazi,<sup>8</sup> M. Tartaglia,<sup>14</sup> T.L.T. Thomas,<sup>31</sup> J. Thompson,<sup>23</sup> T.G. Trippe,<sup>22</sup> P.M. Tuts,<sup>12</sup> N. Varelas,<sup>25</sup> E.W. Varnes,<sup>22</sup> D. Vitito,<sup>2</sup> A.A. Volkov,<sup>35</sup> A.P. Vorobiev,<sup>35</sup> H.D. Wahl,<sup>15</sup> G. Wang,<sup>15</sup> J. Warchol,<sup>32</sup> G. Watts,<sup>5</sup> M. Wayne,<sup>32</sup> H. Weerts,<sup>25</sup> A. White,<sup>44</sup> J.T. White,<sup>45</sup> J.A. Wightman,<sup>19</sup> S. Willis,<sup>30</sup> S.J. Wimpenny,<sup>9</sup> J.V.D. Wirjawan,<sup>45</sup> J. Womersley,<sup>14</sup> E. Won,<sup>39</sup> D.R. Wood,<sup>29</sup> H. Xu,<sup>5</sup> R. Yamada,<sup>14</sup> P. Yamin,<sup>4</sup> C. Yanagisawa,<sup>42</sup> J. Yang,<sup>28</sup> T. Yasuda,<sup>29</sup> P. Yepes,<sup>37</sup> C. Yoshikawa,<sup>16</sup> S. Youssef,<sup>15</sup> J. Yu,<sup>14</sup> Y. Yu,<sup>41</sup> Q. Zhu,<sup>28</sup> Z.H. Zhu,<sup>39</sup> D. Zieminska,<sup>18</sup> A. Zieminski,<sup>18</sup> E.G. Zverev,<sup>26</sup> and A. Zylberstein<sup>40</sup>

(DØ Collaboration)

- <sup>1</sup> *Universidad de los Andes, Bogotá, Colombia*
- <sup>2</sup> *University of Arizona, Tucson, Arizona 85721*
- <sup>3</sup> *Boston University, Boston, Massachusetts 02215*
- <sup>4</sup> *Brookhaven National Laboratory, Upton, New York 11973*
- <sup>5</sup> *Brown University, Providence, Rhode Island 02912*
- <sup>6</sup> *Universidad de Buenos Aires, Buenos Aires, Argentina*
- <sup>7</sup> *University of California, Davis, California 95616*
- <sup>8</sup> *University of California, Irvine, California 92697*
- <sup>9</sup> *University of California, Riverside, California 92521*
- <sup>10</sup> *LAFEX, Centro Brasileiro de Pesquisas Físicas, Rio de Janeiro, Brazil*
- <sup>11</sup> *CINVESTAV, Mexico City, Mexico*
- <sup>12</sup> *Columbia University, New York, New York 10027*
- <sup>13</sup> *Delhi University, Delhi, India 110007*
- <sup>14</sup> *Fermi National Accelerator Laboratory, Batavia, Illinois 60510*
- <sup>15</sup> *Florida State University, Tallahassee, Florida 32306*
- <sup>16</sup> *University of Hawaii, Honolulu, Hawaii 96822*
- <sup>17</sup> *University of Illinois at Chicago, Chicago, Illinois 60607*
- <sup>18</sup> *Indiana University, Bloomington, Indiana 47405*
- <sup>19</sup> *Iowa State University, Ames, Iowa 50011*
- <sup>20</sup> *Korea University, Seoul, Korea*
- <sup>21</sup> *Kyungshung University, Pusan, Korea*
- <sup>22</sup> *Lawrence Berkeley National Laboratory and University of California, Berkeley, California 94720*
- <sup>23</sup> *University of Maryland, College Park, Maryland 20742*
- <sup>24</sup> *University of Michigan, Ann Arbor, Michigan 48109*
- <sup>25</sup> *Michigan State University, East Lansing, Michigan 48824*
- <sup>26</sup> *Moscow State University, Moscow, Russia*
- <sup>27</sup> *University of Nebraska, Lincoln, Nebraska 68588*
- <sup>28</sup> *New York University, New York, New York 10003*
- <sup>29</sup> *Northeastern University, Boston, Massachusetts 02115*
- <sup>30</sup> *Northern Illinois University, DeKalb, Illinois 60115*
- <sup>31</sup> *Northwestern University, Evanston, Illinois 60208*
- <sup>32</sup> *University of Notre Dame, Notre Dame, Indiana 46556*
- <sup>33</sup> *University of Oklahoma, Norman, Oklahoma 73019*
- <sup>34</sup> *University of Panjab, Chandigarh 16-00-14, India*
- <sup>35</sup> *Institute for High Energy Physics, 142-284 Protvino, Russia*
- <sup>36</sup> *Purdue University, West Lafayette, Indiana 47907*
- <sup>37</sup> *Rice University, Houston, Texas 77005*
- <sup>38</sup> *Universidade Estadual do Rio de Janeiro, Brazil*
- <sup>39</sup> *University of Rochester, Rochester, New York 14627*
- <sup>40</sup> *CEA, DAPNIA/Service de Physique des Particules, CE-SACLAY, Gif-sur-Yvette, France*
- <sup>41</sup> *Seoul National University, Seoul, Korea*
- <sup>42</sup> *State University of New York, Stony Brook, New York 11794*
- <sup>43</sup> *Tata Institute of Fundamental Research, Colaba, Mumbai 400005, India*
- <sup>44</sup> *University of Texas, Arlington, Texas 76019*
- <sup>45</sup> *Texas A&M University, College Station, Texas 77843*

The gauge boson pair production processes  $W\gamma$ ,  $WW$ ,  $WZ$ , and  $Z\gamma$  were studied using  $p\bar{p}$  collisions corresponding to an integrated luminosity of approximately  $14 \text{ pb}^{-1}$  at a center-of-mass energy of  $\sqrt{s} = 1.8 \text{ TeV}$ . Analysis of  $W\gamma$  production with subsequent  $W$  boson decay to  $\ell\nu$  ( $\ell = e, \mu$ ) is reported, including a fit to the  $p_T$  spectrum of the photons which leads to limits on anomalous  $WW\gamma$  couplings. A search for  $WW$  production with subsequent decay to  $\ell\bar{\ell}\nu\bar{\nu}$  ( $\ell = e, \mu$ ) is presented, leading to an upper limit on the  $WW$  production cross section and limits on anomalous  $WW\gamma$  and  $WWZ$  couplings. A search for high  $p_T$   $W$  bosons in  $WW$  and  $WZ$  production is described, where one  $W$  boson decays to an electron and a neutrino and the second  $W$  boson or the  $Z$  boson decays to two jets. A maximum likelihood fit to the  $p_T$  spectrum of  $W$  bosons resulted in limits on anomalous  $WW\gamma$  and  $WWZ$  couplings. A combined fit to the three data sets which provided the tightest limits on anomalous  $WW\gamma$  and  $WWZ$  couplings is also described. Limits on anomalous  $ZZ\gamma$  and  $Z\gamma\gamma$  couplings are presented from an analysis of the photon  $E_T$  spectrum in  $Z\gamma$  events in the decay

channels ( $ee$ ,  $\mu\mu$ , and  $\nu\nu$ ) of the  $Z$  boson.

## I. INTRODUCTION

Interactions between gauge bosons, the  $W$  boson,  $Z$  boson and photon, are a consequence of the non-Abelian gauge symmetry of the Standard Model (SM). The gauge boson self-interactions are described by the trilinear gauge boson vertices and contribute to gauge boson pair production in  $p\bar{p}$  collisions. The cross sections of these processes are relatively small within the SM. The inclusion of non-SM (anomalous) couplings at the trilinear gauge boson vertices enhances the production cross sections of gauge boson pairs, especially at large values of the gauge boson transverse momentum  $p_T$ , and at large values of the invariant mass of the gauge boson pair system. Observation of anomalous gauge boson pair production would indicate physics beyond the SM. Feynman diagrams for gauge boson pair production are shown in Figs. 1(a)–(c), where  $V_0, V_1$  and  $V_2$  are the  $W$  boson, the  $Z$  boson, or the photon. Figures 1(a) and (b) are described by well-known couplings between the gauge bosons and quarks. Figure 1(c) shows the trilinear coupling diagram. Numerous phenomenological studies [1] of the characteristics of gauge boson self-interactions have been performed in anticipation of hadron and  $e^+e^-$  collider experiments where direct measurements of the coupling parameters are possible by studying gauge boson pair production processes.

This paper describes studies of gauge boson pair production and the corresponding trilinear gauge boson coupling parameters using data from  $\sqrt{s} = 1.8$  TeV  $p\bar{p}$  collisions taken with the DØ detector during the 1992-1993 Tevatron collider run at the Fermi National Accelerator Laboratory. Four processes were studied:  $W\gamma$  production, where the  $W$  boson decayed into  $e\nu$  or  $\mu\nu$ ;  $W$  boson pair production, where both of the  $W$  bosons decayed into  $e\nu$  or  $\mu\nu$ ;  $WW$  and  $WZ$  production, where one  $W$  boson decayed into  $e\nu$  and the second boson decayed hadronically; and  $Z\gamma$  production, where the  $Z$  boson decayed into  $e^+e^-$ ,  $\mu^+\mu^-$ , or  $\nu\bar{\nu}$ .

This paper presents the details of analyses whose results have already been published [2–6]. In addition, it presents limits on anomalous trilinear couplings from the combined  $W\gamma$ ,  $WW$ , and  $WZ$  analyses.

### A. $WW\gamma$ and $WWZ$ Trilinear Gauge Boson Couplings

A formalism has been developed [7] to describe the  $WW\gamma$  and  $WWZ$  interactions for models beyond the SM using an effective Lagrangian. The  $WW\gamma$  and  $WWZ$  vertices that satisfy Lorentz invariance and conservation of C and P can be described by a Lagrangian with two overall coupling strengths  $g_{WW\gamma} = -e$  and  $g_{WWZ} = -e \cot \theta_w$  and six coupling parameters  $g_1^V, \kappa_V$  and  $\lambda_V$ , where  $V = \gamma, Z$ . In the SM,  $\Delta g_1^V = g_1^V - 1 = 0$ ,  $\Delta \kappa_V = \kappa_V - 1 = 0$ , and  $\lambda_V = 0$ . The anomalous couplings are parameterized as form factors with a scale,  $\Lambda$ , in order to avoid unitarity violation of the gauge boson pair cross section at asymptotically high energies: e.g.,  $\lambda_\gamma(\hat{s}) = \lambda_\gamma/(1 + \hat{s}/\Lambda^2)^2$ . The  $WW\gamma$  and  $WWZ$  coupling parameters, in the static limit, are related to the magnetic dipole moments ( $\mu_W$ ) and electric quadrupole moments ( $Q_W^e$ ) of the  $W$  boson:  $\mu_W = \frac{e}{2M_W}(1 + \kappa + \lambda)$  and  $Q_W^e = -\frac{e}{M_W^2}(\kappa - \lambda)$  [8], where  $e$  and  $M_W$  are the charge and the mass of the  $W$  boson. A more detailed discussion of the effective Lagrangian for the  $WW\gamma$  and  $WWZ$  interactions can be found in Appendix 1.

The  $W\gamma$  production process has the highest cross section among the gauge boson pair production processes at the Tevatron. Feynman diagrams for the  $q\bar{q}' \rightarrow W\gamma$  process are obtained by substituting  $V_0 = V_1 = W$  and  $V_2 = \gamma$  in Figs. 1(a)–(c). A delicate cancellation takes place between the amplitudes [9] that correspond to the  $u$  and  $t$ -channel quark exchange, shown in Figs. 1(a) and (b), and  $s$ -channel production with a  $W$  boson as the mediating particle, shown in Fig. 1(c). A  $W$  boson is identified by its leptonic decay products: a high  $p_T$  charged lepton  $\ell$  ( $\ell = e, \mu$ ); and large missing transverse energy ( $\cancel{E}_T$ ) due to the undetected neutrino. Single  $W$  boson production, followed by radiation of a photon from the charged lepton from the  $W$  boson decay, also contributes to the  $\ell\nu\gamma$  final state. This process is shown in Fig. 2. The photon from the radiative decay is preferentially emitted along the direction of the charged lepton; the process can be suppressed by imposing a minimum separation requirement,  $\Delta R_{\ell\gamma}$ , between the charged lepton and the photon where  $\Delta R_{\ell\gamma}$  is the distance in pseudorapidity and azimuth. For  $\sqrt{s} = 1.8$  TeV  $p\bar{p}$  collisions, the predicted cross section times branching fraction for  $W \rightarrow e\nu$  or  $\mu\nu$  for  $W\gamma$  final states with photon

transverse energy ( $E_T^\gamma$ )  $> 10$  GeV and  $\Delta R_{\ell\gamma} > 0.7$  is 12.5 pb. Figure 3 shows the  $E_T$  spectrum of photons for the SM and non-SM production processes predicted by the leading order theory [10]. The distributions for non-SM  $WW\gamma$  couplings exhibit a large increase in the cross section at high  $E_T^\gamma$ . The  $W\gamma$  process is sensitive only to  $WW\gamma$  couplings, not to  $WWZ$  couplings. It is more sensitive to  $\lambda_\gamma$  than to  $\Delta\kappa_\gamma$ , since the amplitudes related to  $\lambda_\gamma$  and  $\Delta\kappa_\gamma$  are proportional to  $\hat{s}$  and  $\sqrt{\hat{s}}$ , respectively.

Limits on the  $WW\gamma$  trilinear couplings from studies of  $W\gamma$  production have been reported [11,12,2] previously by the UA2, CDF, and DØ Collaborations. In this paper, the results from the DØ Collaboration, with the most restrictive  $WW\gamma$  limits, are presented in more detail than in the recent publication [2].

The process  $p\bar{p} \rightarrow WW + X$  is predicted to have a cross section of 9.5 pb [13] at next-to-leading order at  $\sqrt{s} = 1.8$  TeV. The Feynman diagrams for the  $WW$  production processes are obtained by substituting  $V_0 = \gamma$  or  $Z$ ,  $V_1 = W^+$  and  $V_2 = W^-$  in Figs. 1(a)–(c). Destructive interference, similar to that occurring in  $W\gamma$  production, occurs between the  $u$  and  $t$ -channel amplitudes and the  $s$ -channel amplitude [14] with a photon or a  $Z$  boson as the mediating particle. The former processes contain the well-known couplings between the  $W$  bosons and quarks and the latter the  $WW\gamma$  and  $WWZ$  trilinear couplings.  $W$  boson pair production is sensitive to both of the  $WW\gamma$  and  $WWZ$  couplings. It is approximately a factor of two more sensitive to the  $WWZ$  couplings, due to the higher value of the overall coupling  $g_{WWZ} = -e \cot\theta_w$ , than to the  $WW\gamma$  couplings with  $g_{WW\gamma} = -e$  and is therefore complementary to  $W\gamma$  production. The predicted [15] cross section for  $WW$  production, as a function of anomalous coupling parameters  $\lambda \equiv \lambda_\gamma = \lambda_Z$  and  $\Delta\kappa \equiv \Delta\kappa_\gamma = \Delta\kappa_Z$ , where the  $WW\gamma$  and  $WWZ$  couplings are assumed to be equal and  $\Lambda = 1000$  GeV, is shown in Fig. 4.

The details of the recently published analysis [3], in which an upper limit on the  $WW$  cross section was obtained from the observed number of signal events in the dilepton decay modes, are presented. The limit on the cross section was translated into the limits on anomalous coupling parameters.

For  $p\bar{p}$  collisions at  $\sqrt{s} = 1.8$  TeV, the cross section predicted [16] at next-to-leading order for  $WZ$  production is 2.5 pb. The Feynman diagrams for  $WZ$  production are obtained by substituting  $V_0 = V_1 = W$  and  $V_2 = Z$  in Figs. 1(a)–(c). While  $WW$  production is sensitive to both the  $WW\gamma$  and  $WWZ$  couplings,  $WZ$  production depends only on the  $WWZ$  couplings. The  $WW$  and  $WZ$  decay channels in which one  $W$  boson decays into an electron and a neutrino and the second  $W$  boson or the  $Z$  boson decays hadronically were studied in order to obtain an upper limit on the cross section and to restrict possible anomalies in the coupling parameters. In these processes, the  $W$  and  $Z$  bosons that decay hadronically to produce two jets in the detector cannot be differentiated due to the limitations of jet energy resolution. Figure 5 shows the  $p_T$  spectrum for  $W$  bosons in  $WW$  and  $WZ$  production from the leading-order theoretical prediction [15]. This paper describes in detail an analysis summarized in Ref. [4], in which the  $E_T$  spectrum of the  $W$  bosons, produced with two or more jets which could have come from a hadronic  $W$  or  $Z$  boson decay, was compared to the expected SM signal plus background to set limits on anomalous  $WW\gamma$  and  $WWZ$  couplings. The CDF Collaboration has studied the  $l\nu$  jet-jet decay mode and reported [17] limits on anomalous  $WW\gamma$  and  $WWZ$  couplings.

A new result on the anomalous couplings from a combined fit is presented. Since the  $W\gamma$ ,  $WW$  to dileptons, and  $WW/WZ$  to electron plus jets analyses measured the same coupling parameters, a combined fit to all three data sets was performed, yielding improved limits on the anomalous couplings compared to the individual analyses.

## B. $Z\gamma\gamma$ and $ZZ\gamma$ Trilinear Gauge Boson Couplings

The interactions of pairs of neutral gauge bosons, the  $Z$  boson and the photon, can be studied through the  $Z\gamma$  production process. The Feynman diagrams for the  $q\bar{q}' \rightarrow Z\gamma$  processes are obtained by substituting  $V_0 = \gamma$  or  $Z$ ,  $V_1 = Z$  and  $V_2 = \gamma$  in Figs. 1(a)–(c). There are no  $ZZ\gamma$  and  $Z\gamma\gamma$  couplings of the type shown in Fig. 1(c) in the SM; thus, there is no destructive interference of the  $u$  and  $t$ -channel amplitudes, such as occurs in  $W\gamma$ ,  $WW$ , and  $WZ$  production. A  $Z$  boson is identified by its leptonic decay products, a pair of high  $p_T$  leptons ( $\ell = e$  or  $\mu$ ), or by the imbalance of momentum in the event due to not detecting the neutrino pair. The Drell-Yan production of a  $Z$  boson or virtual photon, followed by radiation of a photon off the charged lepton from the  $Z$  boson or virtual photon decay products, also contributes to the charged lepton final states, as shown in Fig. 6. As with the final state radiation from  $W$  boson decay products, the photon from the  $Z$  boson decay products is preferentially emitted along the charged lepton direction; the process can be suppressed by imposing a cut on the separation between the charged lepton and the photon. The most general Lorentz and gauge invariant  $ZV\gamma$  vertex is described by eight coupling parameters  $h_i^V$  ( $i = 1, \dots, 4$ ) [18]. The anomalous couplings are parameterized as form factors  $h_i^V = h_{i0}^V/(1 + \hat{s}/\Lambda^2)^n$ , where  $\hat{s}$  is the square of the invariant mass of the  $Z\gamma$  system,  $n = 3$  for  $h_{1,3}^V$ , and  $n = 4$  for  $h_{2,4}^V$ . This is discussed in more detail in Appendix 1. Figure 7 shows the  $E_T$  spectra of photons predicted for the SM and the non-SM model

production processes. The distributions for the non-SM  $ZZ\gamma$  and  $Z\gamma\gamma$  couplings exhibit a large increase of the cross section at high  $E_T$ . Limits on the anomalous coupling parameters are obtained from a maximum likelihood fit to the  $E_T$  spectrum of the photons, as in  $W\gamma$  production. Previously, CDF has published limits on the  $ZZ\gamma$  and  $Z\gamma\gamma$  anomalous couplings [19] using the  $ee$  and  $\mu\mu$  final states. Recent results from the DØ experiment are presented here in more detail than in the previous [5,6] summaries and include the  $ee$ ,  $\mu\mu$ , and neutrino final states.

### C. Outline of Paper

The paper is organized as follows. In Section II the DØ detector and the techniques used to identify particles from the collisions are discussed. Section III is a summary of various Monte Carlo modelling tools used in these analyses. Section IV discusses the 1992-1993 collider run and data samples. Section V describes a measurement of the  $WW\gamma$  coupling parameters using  $W\gamma$  events where the  $W$  boson decays into a high  $p_T$  electron or muon and a neutrino. In Section VI the results of a search of  $WW \rightarrow (\ell\bar{\nu})(\bar{\ell}'\nu')$  process are presented. This is followed by a description and the results of the analysis for  $WW$  and  $WZ$  production with subsequent decay to  $e\nu$  and at least two jets in Section VII. Section VIII describes the combined limits on the anomalous couplings from all of the  $W\gamma$  and  $WW/WZ$  analyses. Section IX presents a measurement of  $ZZ\gamma$  and  $Z\gamma\gamma$  coupling parameters using  $Z\gamma$  production events where the  $Z$  boson decays into  $ee$ ,  $\mu\mu$  or  $\nu\bar{\nu}$ . The results are summarized and reviewed in Section X. Appendix 1 contains a detailed review of trilinear gauge boson couplings and the effective Lagrangian. Finally, Appendix 2 contains a discussion of the binned likelihood fitting procedure used in determining the anomalous couplings limits.

## II. DETECTOR

The major components of the DØ detector [20] were a nonmagnetic central tracking detector system, a hermetic liquid-argon uranium calorimeter and a muon spectrometer system with a toroidal magnetic field. A perspective view of the detector is shown in Fig. 8, depicting the three major systems.

The central tracking detectors (CD), shown in Fig. 9, included the Vertex Drift Chamber (VTX), the Transition Radiation Detector (TRD), the Central Drift Chamber (CDC) and two Forward Drift Chambers (FDC's). The VTX, TRD and CDC were arranged in three concentric layers around the beamline, from the beampipe out to the central calorimeter. The wires in the FDC's were oriented perpendicular to the beamline. The entire CD was contained in the cylindrical volume ( $r = 76$  cm,  $z = \pm 135$  cm) bounded by the calorimeter cryostats. The CD measured the trajectory of charged particles with a resolution of 2.5 mrad in  $\phi$  and 28 mrad in  $\theta$ , where  $\phi$  and  $\theta$  are the azimuthal and polar angles of the track, respectively, and covered the region  $|\eta| \leq 3.2$  in pseudorapidity, where  $\eta = -\ln(\tan\frac{\theta}{2})$ . From these measurements, the position of the interaction vertex along the beam direction was determined with a resolution of 8 mm. The presence of a CD track or hits pointing towards a shower was the key element for distinguishing electrons from photons. The CDC and FDC's also provided ionization energy loss measurement for separating single electrons from closely-spaced photon conversion pairs where the photon converted before it reached the tracking detector.

The calorimeter was divided into three parts, each enclosed in a steel cryostat to contain the liquid argon: the central calorimeter (CC) and two end calorimeters (EC's) as shown in Fig. 10. Each consisted of an inner electromagnetic (EM) section, a finely-segmented hadronic section (FH) and a coarsely-segmented hadronic section (CH). The scintillator-based intercryostat detectors (ICD's), which improved the energy resolution for jets that straddled the central and end calorimeters, were inserted into the space between the cryostats. The calorimeter covered the pseudorapidity range  $|\eta| \leq 4.2$ . The boundaries between the CC and EC's were chosen to be approximately perpendicular to the beam direction and to match the transition between the CDC and FDC's.

Each EM section was divided into four longitudinal layers forming a thickness of 21 radiation lengths. The hadronic sections were divided into four (CC) or five (EC) layers and were 7–10 nuclear interaction lengths thick. The calorimeter was transversely segmented into projective towers with  $\Delta\eta \times \Delta\phi = 0.1 \times 0.1$ , where  $\phi$  is the azimuthal angle. The third layer of the EM calorimeters, where the maximum energy deposition from EM showers was expected to occur, was segmented more finely into cells with  $\Delta\eta \times \Delta\phi = 0.05 \times 0.05$ . The azimuthal position resolution for electrons with energy above 50 GeV was approximately 2.5 mm.

The calorimeter provided the energy measurement for electrons, photons, charged hadrons, and jets. The energy resolution of the DØ calorimeter was measured in a test beam for electrons and pions. The energy resolution for electrons and photons was  $\sigma_E/E = 15\%/\sqrt{E(\text{GeV})} \oplus 0.4\%$ . For charged pions and jets the resolutions were approximately  $50\%/\sqrt{E(\text{GeV})}$  and  $80\%/\sqrt{E(\text{GeV})}$ , respectively [20,21]. The transverse energy of a neutrino was inferred from the undetected transverse energy,  $\cancel{E}_T$ , which is the negative of the vector sum of all the transverse energies in

the calorimeter cells. Using a minimum bias data sample, the resolution for each component of the missing transverse energy,  $\cancel{E}_x$  and  $\cancel{E}_y$ , was measured to be  $1.1 \text{ GeV} + 0.02(\sum E_T)$ , where  $\sum E_T$  is the scalar sum of transverse energies in all calorimeter cells. For one analysis (see Section IX C) the  $\cancel{E}_T$  was calculated from the negative of the vector sum of the transverse energies in towers with  $E_T > 200(400) \text{ MeV}$  in the EM (FH1) calorimeters. The hadronic calorimeter scale was determined by comparing the transverse energy of the recoil against that of the electron pair in  $Z \rightarrow ee + X$  events. The resolution of the  $x$  and  $y$  components of the  $\cancel{E}_T$  was  $\sigma = \sqrt{(4.88 \text{ GeV})^2 + (1.34 \cdot P_T^{\text{recoil}})^2}$ .

The muon spectrometer system, shown in Fig. 8, consisted of solid-iron toroidal magnets and sets of proportional drift tubes (PDT's). It provided identification of muons and determination of their trajectories and momenta. Since muons from decays of  $W$  and  $Z$  bosons are primarily in the central region, the analyses presented here used only the wide angle muon spectrometer (WAMUS) which subtended the region  $|\eta| \leq 2.5$ . The WAMUS system consisted of three layers: the "A-layer" with four planes of PDT's, located between the calorimeter and the toroid magnets; and the "B-" and "C-layers" each with three planes of PDT's, located outside the toroid magnets. The toroids were magnetized to  $\pm 1.9 \text{ T}$ . The wires in the drift tubes and the magnetic field lines in the toroids were oriented transversely to the beam direction. The muon system mounted on the central (forward) muon toroid, covering approximately  $|\eta| < 1$  ( $1 < |\eta| < 1.7$ ) is referred to as the "CF (EF)" region.

The total material in the calorimeter and iron toroids varied from 13 to 19 interaction lengths, making background from hadronic punchthrough negligible. Because of the small tracking volume, the background to prompt muons from in-flight decays of  $\pi$  and  $K$  mesons was also negligible.

The muon momentum  $p$  was determined from its deflection angle in the magnetic field of the toroid. The momentum resolution was limited by multiple scattering in the calorimeter and toroid, knowledge of the magnetic field integral, and the accuracy of the deflection angle measurement. The momentum resolution, determined from  $J/\psi \rightarrow \mu\mu$  and  $Z \rightarrow \mu\mu$  events, was  $\sigma(1/p) = 0.18(p - 2)/p^2 \oplus 0.008$  ( $p$  in  $\text{GeV}/c$ ), where  $\oplus$  indicates addition in quadrature.

## A. Trigger

A multi-level, multi-detector trigger system was used for selecting interesting events and recording them to tape. A coincidence between hits in two hodoscopes of scintillation counters (level 0), centered around the beampipe, was required in order to register the presence of an inelastic collision. These counters also served as the luminosity monitor for the experiment. The level 1 and level 1.5 triggers were programmable hardware triggers which made decisions based on combinations of detector-specific algorithms. The level 2 trigger was a farm of 48 Vax 4000/60 and 4000/90 computers which filtered the events based on reconstruction of the information available from the front-end electronics. Losses from the Main Ring beam, usually involved in the production of antiprotons, caused backgrounds in the muon system and calorimeter. In the analyses presented here, triggers which occurred at the times when a Main Ring proton bunch passed through the detector were not used. Similarly, triggers which occurred during the first 0.4 seconds of the 2.4 second antiproton production cycle were vetoed. These "Main Ring vetoes" accounted for approximately 25% trigger deadtime.

At each level of the trigger, the  $D\bar{O}$  trigger system gathered the results from each of the detector-specific triggers and filters. In this way, trigger decisions could be made from combinations of different detector-specific results. Table I is a compilation of the triggers used in the various analyses presented in this paper.

### 1. Calorimeter Trigger

The level 1 triggers for electromagnetic showers were based on analog sums of transverse energy in calorimeter towers with  $\Delta\eta \times \Delta\phi = 0.2 \times 0.2$  and with two longitudinal sections, EM and FH. The level 1 EM trigger required transverse energy in the EM section of a trigger tower to be above preselected thresholds. The level 2 EM algorithm identified electrons and photons by forming clusters, around level 1 trigger towers, of transverse energy read out from the four layers of the EM calorimeter and the first layer of the FH calorimeter. The clusters were of size  $\Delta\eta \times \Delta\phi = 0.3 \times 0.3$ , centered on the highest  $E_T$  tower in the cluster. The longitudinal and transverse profile of the cluster had to satisfy the following requirements which were designed to discriminate electrons and photons from hadronic showers. The fraction of the cluster energy in the EM section had to exceed a value which depended on the energy and location of the cluster in the calorimeter. The transverse shape classification was based on the energy deposition pattern in the third EM layer. The difference of the energy depositions in two regions, of size  $\Delta\eta \times \Delta\phi = 0.25 \times 0.25$  and  $0.15 \times 0.15$  and centered around the cell with highest  $E_T$ , had to be within a range which depended on the total cluster energy.

Another calorimeter based trigger was the “Missing  $E_T$ ” trigger. At level 2 the  $\cancel{E}_T$  was formed from the negative of the vector sum of the  $E_T$  deposited in the calorimeter and ICD cells, corrected for the vertex position.

## 2. Muon Trigger

The muon level 1 and level 1.5 triggers required coincidences of hits in the PDT’s consistent with a muon originating from the collision region. The level 1 algorithm combined coincidences of hits in PDT cells into 60 cm-wide hodoscopic elements. If a combination of hodoscopic elements matched a preprogrammed pattern of a muon track, the event was accepted. In the central region, three layers of PDT’s, each with at least two hit planes, were required except in regions where detector services and support limited the coverage of the one of the layers. In the forward region, defined approximately as  $1.0 \leq |\eta| \leq 2.5$ , three layers of PDT’s were required, with at least three hit planes in the A-layer and two hit planes in both the B- and C-layers. The trigger required a minimum  $p_T$  of 3 GeV/c and became fully efficient at about 6 GeV/c. The level 1 trigger efficiency was  $(79 \pm 3)\%$  for the central region and  $(36 \pm 12)\%$  for the forward region. At level 1.5, the hodoscopic elements had half-cell resolution, providing a sharper  $p_T$  turn-on. A three-layer requirement made at this trigger level reduced the acceptance of the central muon system by approximately 15%.

At level 2, the first stage of the muon reconstruction algorithm, which consisted of the pattern recognition and initial track fit, was performed. To minimize processing time, the search for muon candidates in the forward region was restricted to the sectors which had a level 1 trigger. A valid level 2 trigger was a three-dimensional muon track with hits in at least two planes of two PDT’s. The level 2 muon trigger program calculated several quantities that provided information on the quality of the muon track including: the goodness of track fit in the PDT drift view and along the PDT wire, the projections of the track to the interaction point in both views and the number of hits used to fit the track. A track quality variable was defined as the number of these quantities that failed the standard criteria. In addition, in the forward region, muon candidates formed with less than six hits on the track were discarded, since they were likely to be random background hits in coincidence. In the central region, cosmic ray muons were identified if there was evidence of a single muon penetrating the entire detector; muon candidates with a track within 20 deg in  $\phi$  and 5 deg in  $\theta$  or hits within 60 cm (roughly 5 deg) of the projection of the muon track into the opposite side PDT’s were rejected. The muon was accepted by level 2 if the  $p_T$  was above the desired threshold and if the track quality variable was zero (“tight” standards), or one (“loose” standards). The muon level 2 trigger efficiency was determined to be  $(95 \pm 3)\%$  excluding effects of the chamber efficiencies and geometrical acceptance for the “loose” muon requirements of the MU-ELE trigger (see Table I).

Trigger Name	Level 1	Level 1.5	Level 2	Analyses
MU-MAX	$1 \mu,  \eta  \leq 1.7$	$1 \mu,  \eta  \leq 1.7$	$1 \mu$ (tight), $p_T \geq 15$ GeV	$WW \rightarrow \mu\mu$
MU-ELE	1 EM tower, $E_T \geq 7$ GeV $1 \mu,  \eta  \leq 1.7$	-	1 e or $\gamma$ , $E_T \geq 7$ GeV $1 \mu$ (loose), $p_T \geq 5$ GeV/c	$WW \rightarrow e\mu$ $W\gamma \rightarrow \mu\nu\gamma$ $Z\gamma \rightarrow \mu\mu\gamma$
ELE-HIGH	1 EM tower, $E_T \geq 14$ GeV	-	1 e or $\gamma$ , $E_T \geq 20$ GeV	$WW/WZ \rightarrow$ $e\nu$ jet jet $Z\gamma \rightarrow \nu\nu\gamma$
ELE-MAX	1 EM tower, $E_T \geq 10$ GeV	-	1 e or $\gamma$ , $E_T \geq 20$ GeV $\cancel{E}_T \geq 20$ GeV	$W\gamma \rightarrow e\nu\gamma$
ELE-2-HIGH	2 EM towers, $E_T \geq 7$ GeV	-	2 e and/or $\gamma$ , $E_T \geq 10$ GeV	$WW \rightarrow ee$
ELE-2-MAX	2 EM towers, $E_T \geq 7$ GeV	-	2 e and/or $\gamma$ , $E_T \geq 20$ GeV	$Z\gamma \rightarrow ee\gamma$

TABLE I. Triggers used in the analyses presented in this paper. The ELE-2-MAX trigger was a subset of the ELE-2-HIGH trigger which included shower shape cuts on the EM candidates.

## B. Muon Identification

Muons were identified as tracks in the muon PDT’s in association with tracks in the CD and energy deposits in the calorimeter. The momentum of the muon was computed from the deflection of the track in the magnetized toroid. The track fit used a least-squares calculation which considered seven parameters: four describing the position and angle of the track before the calorimeter, two describing the effects due to multiple Coulomb scattering, and the inverse of

the muon momentum,  $1/p$ . This seven parameter fit was applied to 16 data points: vertex position measurements in the  $x$  and  $y$  directions, the angles and positions of the track segments before and after the calorimeter and outside of the toroid magnet, and two angles representing the multiple scattering of the muon in the calorimeter. The fit determined the charge of the muon and which CD track, if any, matched the muon. The muon momentum was then corrected for the energy lost in the calorimeter using a GEANT-based [22] detector model.

In the following, the quantities used to describe the muon tracks are presented. The definitions for muons differ slightly among the various analyses because of the nature and magnitude of the backgrounds. Table II lists the five different definitions of muons in the analyses described in this paper.

### 1. Muon Track Quality

The muon reconstruction algorithm defined a muon track quality, similar to that used in the level 2 trigger, which contained information about the number of hits on the track from each layer of muon PDT's, the track impact parameters, and the goodness of the track fit. If the track did not satisfy criteria on more than one of the above quantities, the muon candidate was rejected. Figures 11(a) and (b) show the impact parameters in the track bend view ( $r - z$  plane),  $b_{\text{bend}}$ , and in the track nonbend view ( $x - y$  plane),  $b_{\text{nonbend}}$ , for muons which satisfied all of the other selection criteria. The 3D impact parameter was sometimes used in lieu of the combination of the  $r - z$  and  $x - y$  selection criteria.

### 2. Fiducial Requirements

Muons which passed through the region between the CF and EF toroid magnets near  $|\eta| \approx 0.9$  may have traversed a smaller amount of magnetized iron and thus have a reduced momentum resolution. To reject these poorly measured muons, all of the muon identification definitions in this paper except “Loose II” required the minimum magnetic field integral along the muon track,  $\int Bdl$ , to be at least 2.0 Tesla-meters.

The “Tight II”, “Tight III”, and “Loose II” definitions required that the muon have hits in the A-layer, between the calorimeter and the toroid magnet. Making this requirement reduced the fake-muon background in the forward region but also reduced the acceptance by limiting the pseudorapidity coverage to approximately  $|\eta| < 1.7$ . A cut on  $|\eta| < 1.7$  was used to restrict the muon tracks to those totally contained within the WAMUS spectrometer.

### 3. Central Detector Track-Match

Muon candidates were required to have a confirming track in the CD within a range in both the polar and azimuthal angles. This reduced the backgrounds from cosmic ray muons and from combinations of random hits.

### 4. Calorimeter Confirmation

Muons deposited energy in the calorimeter as they passed through it. It was required that at least 1 GeV of energy was deposited in the tower which contained the projection of the muon track through the calorimeter and the nearest neighboring towers. Figure 11(c) shows the energy deposition in these towers around muons which passed the other selection requirements.

### 5. Cosmic Ray Identification

The muon track was refitted with the timing of the muon track with respect to the  $p\bar{p}$  interaction as a floating parameter,  $t_0$ . This allowed identification of cosmic ray muons. Figure 11(d) shows the value of  $t_0$  which resulted in the best track-fit for muons which passed all other selection requirements. The “Tight I” and “Tight II” definitions required  $t_0 < 100$  ns.



## 6. Muon Isolation

Muons from the decay of pions, kaons, and heavy quarks were reduced by requiring that the muon be isolated from other jet activity. This was done in three ways. One isolation variable (2NN) was defined by summing the energy deposited in the calorimeter cells hit by the muon and two nearest neighbors, subtracting the energy expected to have been deposited by the muon, and dividing the difference by the uncertainty. This was required to be less than five standard deviations. Another isolation variable (Halo) was defined as the difference between the energy deposited in a cone of size  $\Delta R = 0.6$  and the energy deposited in a cone of size  $\Delta R = 0.2$ , where  $\Delta R = \sqrt{\Delta\eta^2 + \Delta\phi^2}$ , around the muon in the calorimeter. This was required to be less than 8 GeV. The third isolation criterion ( $\Delta R_{\mu\text{-jet}}$ ) was that muons were spatially separated from the axis of any jet with  $E_T \geq 10$  GeV by at least  $\Delta R = 0.5$ .

Selection	Tight I	Tight II	Tight III	Loose I	Loose II
Analysis	$WW \rightarrow \mu\mu\nu\bar{\nu}$	$W\gamma \rightarrow \mu\nu\gamma$	$Z\gamma \rightarrow \mu\mu\gamma$	$WW \rightarrow e\mu\nu\bar{\nu}$	$Z\gamma \rightarrow \mu\mu\gamma$
Muon Quality	✓	✓	✓	✓	✓
Back-to-Back Muons Removed	✓	✓	✓	✓	✓
Minimum Field Integral (T-m)	2.0	2.0	1.9	2.0	-
3-Layers Required	-	-	✓	-	-
A-Layer Required	-	✓	✓	-	✓
Isolation Requirement	2NN Cut Halo Cut	$\Delta R_{\mu\text{-jet}} > 0.5$	$\Delta R_{\mu\text{-jet}} > 0.5$	$\Delta R_{\mu\text{-jet}} > 0.5$	$\Delta R_{\mu\text{-jet}} > 0.5$
Impact Parameter	$ 3D  \leq 22$ cm	$ RZ  \leq 22$ cm $ XY  \leq 15$ cm	$ RZ  \leq 22$ cm	$ 3D  \leq 22$ cm	$ RZ  \leq 22$ cm
$t_0$	$\leq 100$ ns	$\leq 100$ ns	-	-	-
CD Match	$\delta\phi \leq 0.45$ $\delta\theta \leq 0.45$	$\delta\phi \leq 0.25$ $\delta\theta \leq 0.30$	$\delta\phi \leq 0.25$ $\delta\theta \leq 0.30$	$\delta\phi \leq 0.45$ $\delta\theta \leq 0.45$	$\delta\phi \leq 0.25$ $\delta\theta \leq 0.30$
Cal Confirm	✓	✓	✓	✓	✓

TABLE II. Summary of the various muon identification definitions used in the analyses presented in this paper.

## C. Electron and Photon Identification

Electrons and photons were identified by the properties of the shower in the calorimeter and the presence, or lack thereof, of a matching track in the CD. Using a nearest-neighbor algorithm, clusters were formed from adjacent EM towers containing significant energy deposition. The clusters for which the energy in the EM and first FH section of the calorimeter divided by the sum of the energies in the EM and all hadronic sections (EMF) was greater than or equal to 0.9 were flagged as possible electrons or photons. Figure 12(a) shows the fraction of electrons from Z boson decays for which the EMF is above the value given on the abscissa. More detailed analysis of the calorimeter and tracking chamber information was then used to refine the sample as is described below. A summary of electron definitions is presented in Table III. The photon definitions are summarized in Table IV.

### 1. Fiducial Coverage of EM Calorimeter

All of the analyses presented in this paper made identical selection on the fiducial coverage of the EM calorimeter. It was required that the electron or photon have pseudorapidity within the range  $\pm 2.5$ . Furthermore, the EM calorimeter had a gap in the coverage at the transition between the CC and the EC. The four longitudinal layer coverage of the CC ended at pseudorapidity of 1.1 and the four longitudinal layer coverage of the EC returned at pseudorapidity of 1.5. Therefore, all analyses of photons and electrons in this paper made a fiducial selection which removed this transition region. The “Tight” photon identification criteria went one step further, requiring that photons in the CC have pseudorapidity within the range  $\pm 1.0$ . The samples used in the discussion of photon and electron identification presented below have these fiducial selections already applied.

## 2. Covariance Matrix $\chi^2$

The electron or photon shower shape was characterized by the fraction of the cluster energy deposited into each layer of the calorimeter. These fractions were correlated, depending on the depth of the start of the shower and on the energy of the incident particle. In order to reject background using the shower shape, including these correlations, a comparison was made between the candidate and a reference sample of Monte Carlo electrons with energies ranging from 10 to 150 GeV. This comparison (H-matrix  $\chi^2$ ) was carried out in 41 observables: the fractional energies in layers 1, 2, and 4 of the EM calorimeter; the fractional energy in each cell of a  $6 \times 6$  array of cells in layer 3 centered on the most energetic tower in the EM cluster; the logarithm of the total energy of the electron cluster, taking into account the depth dependence on the incident energy; and the position of the event vertex along the beam direction, taking into account the dependence of the shower shape on the incident angle. A separate reference shower shape was available as a function of  $\eta$ , assuming  $\phi$  symmetry. Figure 12(b) shows the fraction of electrons from Z boson decays for which the value of the H-matrix  $\chi^2$  is less than the value given on the abscissa. Requiring that the H-matrix  $\chi^2 < 100(200)$  in the CC (EC) gave an efficiency of  $94.9 \pm 0.8\%$  ( $100.0^{+0.0}_{-1.0}\%$ ) for electrons with  $E_T > 25$  GeV.

The efficiency for the H-matrix selection decreased if the  $E_T$  fell below 25 GeV. The efficiency as a function of photon  $E_T$  was measured in a test beam for both the CC and EC. This dependence was a dominant source of systematic uncertainty in the efficiency for low  $p_T$  photons. Figure 13 shows the efficiency versus  $p_T$  for the H-matrix selection criteria for low  $p_T$  “Loose” photons.

## 3. Cluster Isolation

The EM clusters were required to be isolated from other particles in the event in order to reduce the background from hadronic jets with high EM content. The isolation variable was

$$f_{\text{iso}} = \frac{E(0.4) - EM(0.2)}{EM(0.2)}, \quad (2.1)$$

where  $E(0.4)$  was the energy deposited in all the calorimeter cells in a cone of radius  $R = 0.4$  around the electron or photon and  $EM(0.2)$  was the energy deposited in the EM calorimeter in a cone of radius  $R = 0.2$ . For EM objects with  $E_T < 20$  GeV, there was deterioration of the efficiency of the  $f_{\text{iso}}$  selection criteria. This was modeled with a turn-on curve in a way similar to the H-matrix efficiency described above. Figure 12(c) shows the fraction of electrons from Z boson decays passing an  $f_{\text{iso}}$  selection criterion. Requiring  $f_{\text{iso}} < 0.10$  was  $97.6 \pm 0.6\%$  ( $98.5 \pm 1.4\%$ ) efficient for CC (EC) electron candidates.

## 4. Electromagnetic Fraction

The “Tight” photon identification criteria included the requirement that the energy deposited in the four EM layers be at least 96% of total energy in the calorimeter in a cone around the shower maximum. This was in addition to the EMF requirement discussed above.

## 5. Electron Track Match

Electrons and photons were distinguished from each other by the presence of a track consistent with the passage of a charged particle in the CD which pointed to the EM cluster in the calorimeter. An electron had such a track; a photon did not. The efficiency for track-finding was  $86.7 \pm 1.4\%$  in the CDC and  $86.1 \pm 1.8\%$  in the FDC’s. By demanding a good spatial match between the cluster and the track, backgrounds due to accidental overlaps of charged particles with photons in EM jets were reduced. In the calorimeter, the shower centroid,  $\vec{x}_c$ , was determined from the weighted mean of the coordinates  $\vec{x}_i$  of all cells containing the shower,  $\vec{x}_c = \sum_i w_i \vec{x}_i / \sum_i w_i$ . The weights were defined as  $w_i = \max(0, w_0 + \ln \frac{E_i}{E})$ , where  $E_i$  was the energy in the  $i$ th cell,  $E$  the energy of the cluster, and  $w_0$  a parameter chosen to optimize the position resolution. The logarithmic weighting was motivated by the exponential lateral profile of an electromagnetic shower. The azimuthal position matching resolution in the CC and EC was measured to be  $\approx 2.5$  mm. The CD track was extrapolated to the shower centroid and the significance of the track match,  $TMS$ , was formed between the position of the track and the centroid. For the CC this quantity was

$$TMS_{CC} = \sqrt{\left(\frac{\Delta\phi}{\delta_{\Delta\phi}}\right)^2 + \left(\frac{\Delta z}{\delta_{\Delta z}}\right)^2}, \quad (2.2)$$

where  $\Delta\phi$  was the azimuthal mismatch,  $\Delta z$  the mismatch along the beam direction, and  $\delta_x$  was the resolution for the observable  $x$ . For the EC,  $\Delta z$  was replaced by  $\Delta r$ , the mismatch transverse to the beam. Figure 12(d) shows the fraction of electrons from  $Z$  boson decays for which the track match significance variable is less than the criterion on the abscissa. Requiring  $TMS \leq 10$  was  $98.0 \pm 0.6\%$  ( $91.5 \pm 1.8\%$ ) efficient for CC (EC) electron candidates.

### 6. Electron Track Ionization

The tracks from  $e^+e^-$  pairs produced in photon conversions due to interactions with material in the tracking chambers were often reconstructed as a single track. For such pairs, the ionization in the tracking chambers was expected to be twice that of a single charged particle. The distribution of ionization per unit length ( $dE/dx$ ) for electrons from  $Z \rightarrow ee$  decays and from EM clusters in an inclusive jet sample are shown in Figs. 14(a) and 14(b). Most electrons had  $dE/dx \approx 1$ . The ionization in the inclusive jet sample shows a two-peaked structure. The lower peak, at  $dE/dx \approx 1$  was due to single charged particles. The higher peak came from unresolved  $e^+e^-$  pairs. This background was rejected by removing electron candidates with  $dE/dx \sim 2$ . The veto requirement for CC(EC) was  $1.6 \leq dE/dx \leq 3.0$  ( $1.6 \leq dE/dx \leq 2.6$ ) and was  $94.4 \pm 1.1$  ( $75.2 \pm 3.7$ )% efficient for electrons from  $Z$  bosons.

### 7. Loss of Photons due to Track Overlaps

Some photons were mislabeled as electrons because of spatial overlap of the photon with a random track. The inefficiency introduced was estimated by looking for a track or tracks in a cone randomly oriented in  $\phi$  but at the same  $\eta$  location as the electrons in  $Z$  boson decays to  $ee$ . The assumption is that the probability of finding such a track or tracks at a given  $\eta$  is the same in  $Z$  boson production and double vector boson production. The probability for a random track overlap was found to be  $6 \pm 1\%$  and  $15 \pm 1\%$  for the CC and EC, respectively, the latter being higher due to the higher density of tracks in the forward direction.

### 8. Photon Conversions

Some photons were lost when they converted to  $e^+e^-$  pairs in material in front of the CDC or FDC. The conversion probability was calculated using the GEANT simulation of the DØ detector. This probability depended on the pseudorapidity of the photon and is shown in Fig. 15. Averaged over the CC (EC) it amounted to a 10% (26%) loss of photons. There is a systematic uncertainty of 5%.

### 9. Photon-Vertex Projection

An algorithm, EMVTX, was developed to reduce the background from cosmic ray or beam-related muon bremsstrahlung which produced photons inconsistent with having originated at the event vertex. The energy-weighted centers of the cluster in each of the four layers of the EM calorimeter plus the vertex position, and their uncertainties, were used to compute two dimensional fits. The resulting  $\chi^2$  was then converted into a probability for the photon to have originated at the vertex. It was required that the probability of the  $RZ$  and  $XY$  projections,  $P_{RZ}$  and  $P_{XY}$ , each exceed 1%. Comparison of the  $P_{RZ}$  and  $P_{XY}$  distributions for electrons from  $Z$  bosons and from photons resulting from cosmic ray bremsstrahlung are shown in Fig. 16. In case there were multiple vertices in the event, the one with the highest  $P_{RZ}$  was selected as the vertex for the interaction. This vertex was then used in computing the missing transverse energy and  $E_T^\gamma$ . The vertex resolution provided by this algorithm was approximately 17 (11) cm in the  $RZ$  ( $XY$ ) planes.

The backgrounds to photons from electrons and high-EM content jets with unreconstructed tracks were reduced by looking for hits in narrow roads between the vertex and the EM cluster in the calorimeter. In particular, a background to  $Z\gamma \rightarrow \nu\nu\gamma$  was  $W \rightarrow e\nu$  events where the electron was misidentified as a photon. The tracking algorithm could have been confused by extra hits or have missed the track because the wrong vertex was selected (in the case of multiple vertices) or because the vertex was reconstructed poorly and the track pointed in a different direction. An algorithm was developed, called HITSINFO, to identify this background. Roads were defined between the cluster and each reconstructed vertex as well as the vertex position obtained by the EMVTX algorithm. The road size depended on the tracking chamber. The following road sizes were used:

$$\begin{aligned}\Delta\theta_{VTX} &= 0.005, \Delta\phi_{VTX} = 0.012; \\ \Delta\theta_{CDC} &= 0.050, \Delta\phi_{CDC} = 0.0075; \\ \Delta\theta_{FDC} &= 0.005, \Delta\phi_{FDC} = 0.015;\end{aligned}$$

where the angles,  $\Delta\theta$  and  $\Delta\phi$ , were the half-opening angles of the roads in the  $RZ$  and  $XY$  planes.

The roads were examined for tracks and hits. The photon candidate was required to have no tracks from any vertex. Further requirements were made on the fraction of available wires hit, the number of reconstructed track segments, and on the number of hits, depending on the tracking sub-detector. The selection criteria were optimized using the  $Z \rightarrow ee$  sample with one of the electrons being misidentified as a photon due to tracking chamber inefficiency. The efficiency was calculated using a sample of “emulated” photons obtained by rotation of the positions of the electron energy clusters by 90 degrees in  $\phi$  and then applying the selection criteria.

Selection	Tight I	Tight II	Tight III	Tight IV	Loose I
Analysis	$WW \rightarrow ee$ and $e\mu$	$Z\gamma \rightarrow ee\gamma$	$W\gamma \rightarrow e\nu\gamma$	$WW/WZ \rightarrow e\nu$ jet jet	$Z\gamma \rightarrow ee\gamma$
EM Fraction	$> 0.90$	$> 0.90$	$> 0.90$	$> 0.90$	$> 0.90$
Track Match	$\checkmark$	$\checkmark$	$\checkmark$	$\checkmark$	-
CC (EC) $\chi^2$	$< 100(100)$	$< 100(200)$	$< 100(200)$	$< 100(100)$	$< 100(200)$
Isolation	$< 0.1$	$< 0.1$	$< 0.15$	$< 0.1$	$< 0.1$
$TMS$	$< 10\sigma$	$< 10\sigma$	$< 10\sigma$	$< 5\sigma$	-
$dE/dx$	$\checkmark$	-	-	-	-
CC Efficiency	$72.9 \pm 2.3\%$	$78.1 \pm 2.3\%$	$79 \pm 2\%$	$76.7 \pm 1.6\%$	$90.2 \pm 1.3\%$
EC Efficiency	$51.0 \pm 3.6\%$	$70.8 \pm 3.4\%$	$78 \pm 3\%$	$62.0 \pm 3.1\%$	$97.1 \pm 2.9\%$

TABLE III. Summary of the various electron identification definitions used in the analyses presented in this paper.

Selection	Tight	Loose
Analysis	$Z\gamma \rightarrow \nu\nu\gamma$	$W\gamma$ $Z\gamma \rightarrow ee\gamma$ and $\mu\mu\gamma$
EM Fraction	$> 0.96$	$> 0.90$
CC (EC) $\chi^2$	$< 100(100)$	$< 100(200)$
Isolation	$< 0.1$	$< 0.1$
Matching Track	Veto	Veto
EMVTX	$\checkmark$	-
HITSINFO	$\checkmark$	-
CC Efficiency	$57 \pm 2\%$	$74 \pm 7\%$
EC Efficiency	$56 \pm 4\%$	$58 \pm 5\%$

TABLE IV. Summary of the various photon identification definitions used in the analyses presented in this paper. The “Loose” efficiencies do not include the  $p_T$  dependent effects important at low  $p_T$ . Similarly, the “Tight” efficiency applies to only the high  $p_T$  photons within the fiducial region.

## D. Jet Reconstruction

Jets were reconstructed using cone algorithms with cone sizes,  $\Delta\mathcal{R}$ , of 0.3, 0.5, and 0.7 for the analyses presented in this paper. The algorithm was as follows. First, a jet candidate was identified by forming preclusters of size  $\Delta\eta \times \Delta\phi = 0.3 \times 0.3$ , centered on the highest  $E_T$  tower in the cluster, from a list of jet towers with  $E_T \geq 1.0$  GeV ordered by  $E_T$ . Next, the jet direction was determined by an iterative process. A cone of size  $\Delta\mathcal{R}$  was placed around a new  $E_T$  weighted jet center of towers and the process was repeated until the jet direction became stable. If two jets shared energy, they were combined or split, based on the fraction of energy shared relative to the  $E_T$  of lower  $E_T$  jet. If the shared energy was greater than 50% of the lower  $E_T$  jet, the jets were merged.

The jet energy was corrected for a number of effects. These included energy contributed to the jet from the underlying event, energy from the jet which escaped the jet cone, energy lost due to the zero-suppression, as well as the overall jet energy scale. A cone of radius  $\Delta\mathcal{R} = 0.7$  was selected by all analyses presented here, except for the  $WW/WZ \rightarrow e\nu$  jet jet analysis, where a cone of radius  $\Delta\mathcal{R} = 0.3$  was used, and the  $Z\gamma \rightarrow \nu\bar{\nu}\gamma$  analysis, where a cone of radius  $\Delta\mathcal{R} = 0.5$  was used. The small cone size was advantageous for detecting two closely-spaced jets expected from high- $p_T$   $W$  boson decays. The larger cone size had smaller  $E_T$  corrections.

## E. Missing Transverse Energy

The missing transverse energy in the calorimeter  $\cancel{E}_T^{\text{cal}}$  was defined as

$$\cancel{E}_T^{\text{cal}} = \sqrt{\cancel{E}_{Tx}^{\text{cal}2} + \cancel{E}_{Ty}^{\text{cal}2}}, \quad (2.3)$$

where

$$\cancel{E}_{Tx}^{\text{cal}} = - \sum_i E_i \sin \theta_i \cos \phi_i - \sum_j \Delta E_x^i, \quad (2.4)$$

$$\cancel{E}_{Ty}^{\text{cal}} = - \sum_i E_i \sin \theta_i \sin \phi_i - \sum_j \Delta E_y^i, \quad (2.5)$$

The first sum is over all the cells in the calorimeter and ICD. The second sum is over all the corrections in  $E_T$  applied to all the electrons and jets in the event. In order to obtain the best resolution, the corrections  $\Delta E_T^i$  were those from reconstructing the event with a jet of cone size  $\Delta\mathcal{R} = 0.7$ .

The sources of  $\cancel{E}_T$  included neutrinos, which escaped undetected, and the energy imbalance due to the resolution of the calorimeter and muon system. The missing transverse energy was corrected if there were muons in the event. The transverse momenta of the muons were removed from the  $\cancel{E}_T^{\text{cal}}$  to form the total missing  $E_T$ , whose components were:

$$\cancel{E}_{Tx} = \cancel{E}_{Tx}^{\text{cal}} - \sum_i p_x^{\mu_i}, \quad (2.6)$$

$$\cancel{E}_{Ty} = \cancel{E}_{Ty}^{\text{cal}} - \sum_i p_y^{\mu_i}. \quad (2.7)$$

In that which follows in this paper, analyses not involving muons did not distinguish between  $\cancel{E}_T^{\text{cal}}$  and  $\cancel{E}_T$ ; the “cal” superscript is then ignored.

## III. MONTE CARLO SIMULATION

In order to determine effects due to experimental limitations such as detector acceptances, resolutions, and efficiencies on the expected signal and background, and to provide a cross-check for many of the quantities measured with the data, simulations of the detector and trigger were developed. Various levels of sophistication were used, depending on the detail required.

## A. Detector simulation programs

The most detailed model of the detector was the GEANT [22] simulation. The DØ implementation of GEANT, DØGEANT, included details of the geometry of individual detectors, instrumental efficiencies and resolutions, and particle responses. The performance of the DØGEANT program was confirmed by comparing the simulation results with the data taken from test beams [21], cosmic ray muons and  $\bar{p}p$  collisions. It was typically used to predict and cross-check the effect of variations in the particle identification requirements on the efficiency for leptons and jets. It was also used to predict and cross-check the effect of changing the kinematic requirements on the number and characteristics of some of the signals and backgrounds.

In a typical application, an event generator such as PYTHIA [23] or ISAJET [24] was used to create a list of particles produced in the collision. The simulation converted this into a Monte Carlo event with the same format as the digitized information from the real collision. This Monte Carlo event was then reconstructed in the same way as the data. As it was a very detailed detector simulation, it consumed relatively large quantities of computer resources. This limited its application to problems of manageable scale.

In order to speed-up the GEANT simulation, the calorimeter response for electrons, photons, and hadrons could be modeled using a database of particle showers called the Shower Library. The Shower Library [25] was created by storing the energy deposition in each calorimeter cell for each shower that was generated using GEANT in the full shower mode. Each shower was stored in a list together with its particle identity, momentum, pseudorapidity, azimuth, and collision vertex origin. When using the Shower Library to simulate the response of a particle in a Monte Carlo event, a shower of the appropriate type was selected randomly from the library and added to the event. This method was useful, for example, in determining the efficiency for dijets in the  $WW/WZ \rightarrow e\nu$  jet jet analysis presented in Section VII, where the advantage of speed made it possible to create a parameterization of the efficiency.

An even faster simulation, DØFAST, with correspondingly less detail, used simplified geometrical structures of the DØ detector and parameterizations of the detector response including energy (momentum) resolutions, particle identification efficiencies, and trigger turn-on curves obtained from the data and described in the previous section. Careful comparisons were performed between DØFAST and DØGEANT for the processes with Standard Model couplings to ensure that nothing important was lost in using the former. This simulation was used, for example, to model the acceptance for the grid points in the anomalous coupling parameter space, where dozens of grid points were used, each with 10,000 to 100,000 MC events. A similar fast Monte Carlo was used to estimate the background from  $Z$  boson decays for the  $WW \rightarrow$  dileptons analyses.

## B. Trigger Simulation

In order to optimize and cross-check the efficiency of the triggers described in Table I, and to provide a method for finding the efficiency of combinations of separate triggers, a detailed simulation of the trigger algorithm was made. The list of available triggers, particularly those used for monitoring the higher- $p_T$  triggers, changed from time-to-time over the course of the run as the luminosity increased. Occasionally the algorithms were improved as our understanding of the detector improved. The trigger simulation, TRIGSIM, was used to pre-test the changes in the trigger. The output from the GEANT simulation was processed by the simulator using level 1 (L1.0) and level 1.5 (L1.5) hardware and level 2 (L2.0) software simulations. The L2.0 simulation used software identical to that used in the L2 computers. The results were then compared to the arrays of available triggers and the events were marked as passed or failed. The simulator was cross-checked against the actual trigger using real data as input events.

## IV. DATA SAMPLES

During the 1992–1993  $p\bar{p}$  collider run, the Fermilab Tevatron, operating at a center of mass energy of  $\sqrt{s} = 1.8$  TeV, delivered a total integrated luminosity of  $\int L dt = 21.8 \text{ pb}^{-1}$ . Typical instantaneous luminosities of  $4 \times 10^{30} \text{ cm}^{-2}\text{sec}^{-1}$  were attained. DØ collected  $14.4 \text{ pb}^{-1}$  to tape. The difference between delivered and collected luminosity was dominated by the dead time incurred due to operation of the Main Ring accelerator. A small part of the data was lost due to operational difficulties and hardware problems (bad runs) at the time of data collection.

The luminosity was calculated by measuring the rate for  $p\bar{p}$  nondiffractive inelastic collisions using the level 0 scintillation counter hodoscopes. The normalization for the luminosity measurement and the 5.4% systematic uncertainty came from the  $p\bar{p}$  inelastic cross section and the uncertainty in the acceptance of the counters [26]. The

final integrated luminosity varied from trigger to trigger for a number of reasons. The muon L1.5 triggers started operating approximately six weeks after the muon L1.0 and calorimeter triggers. The muon triggers tended to be prescaled at high luminosities because they had higher L1.0 and L1.5 trigger rates than the calorimeter triggers. Finally the analyses which used only EM objects could use luminosity collected while the muon system had hardware problems whereas the muon system, which relied on the calorimeter as part of muon identification, could not use luminosity collected when the calorimeter had a problem. The luminosity for a given trigger may have varied slightly from analysis to analysis depending on the bad run list used. Table V shows the total integrated luminosity, after bad run removal, for each trigger used in the analyses presented in this paper.

Trigger	$\int L dt$ (pb $^{-1}$ )
MU-MAX	$12.2 \pm 0.7$
MU-ELE	$13.8 \pm 0.7$
ELE-HIGH	$13.7 \pm 0.7$ ( $13.1 \pm 0.7$ )
ELE-MAX	$13.8 \pm 0.7$
ELE-2-HIGH	$14.3 \pm 0.8$
ELE-2-MAX	$14.3 \pm 0.8$

TABLE V. Integrated luminosity for each trigger after accounting for the effects of the Main Ring and for bad runs due to hardware problems. The ELE-HIGH trigger has separate luminosities depending on whether the calorimeter or calorimeter plus muon system were checked.

## V. $W\gamma$ ANALYSIS

A measurement of the  $WW\gamma$  couplings using  $p\bar{p} \rightarrow \ell\nu\gamma + X$  ( $\ell = e, \mu$ ) events is presented in this section. These events contained the  $W\gamma$  production processes,  $p\bar{p} \rightarrow W\gamma$ , followed by  $W \rightarrow \ell\nu$  or the final state radiation process  $W \rightarrow \ell\nu \rightarrow \ell\nu\gamma$ , as shown in Figs. 1 and 2. Anomalous coupling parameters would enhance the  $W\gamma$  production cross section, leading to an excess of events with high transverse energy photons, well separated from the charged lepton. Figure 3 shows the photon spectrum from SM and anomalous couplings predicted by theory [10]. The procedure of the analysis was to obtain a candidate sample, estimate the background contribution as a function of photon  $E_T$ , and compare the background-subtracted candidate photon spectrum with that expected from various anomalous  $WW\gamma$  couplings. In the following, the electron and muon channels are referred to as  $W(e\nu)\gamma$  and  $W(\mu\nu)\gamma$ , respectively.

### A. Event selection

The  $W(e\nu)\gamma$  candidates were obtained by searching for events with an isolated high  $E_T$  electron, large missing transverse energy, and an isolated photon. The data sample was taken with a L1.0 trigger that required at least one EM tower with  $E_T > 10$  GeV and the ELE-MAX trigger at level 2, that required an isolated EM cluster with  $E_T \geq 20$  GeV and  $\cancel{E}_T \geq 20$  GeV, as described in Table I. The data sample corresponded to an integrated luminosity of  $13.8 \pm 0.7$  pb $^{-1}$ . The electron was required to pass the “Tight III” requirements of Table III and the photon to pass the “Loose” requirements as described in Table IV. The electron and photon were required to be within the fiducial region of the calorimeter, as discussed in Section II C 1, and at least 0.01 radians away from the azimuthal boundaries of the 32 EM modules in the CC. Kinematic selection was made requiring  $E_T^e > 25$  GeV,  $\cancel{E}_T > 25$  GeV, and  $M_T > 40$  GeV/c $^2$ , where  $M_T$  is the transverse mass of the electron and  $\cancel{E}_T$  vector defined as

$$M_T = [2E_T^e \cancel{E}_T (1 - \cos \phi^{e\nu})]^{1/2}, \quad (5.1)$$

and  $\phi^{e\nu}$  is the angle between the electron  $E_T$  and the  $\cancel{E}_T$ .

The  $W(\mu\nu)\gamma$  candidates were obtained by searching for events with an isolated high  $p_T$  muon and an isolated photon in the data sample taken with the MU-ELE trigger described in Table I. The sample corresponded to an integrated luminosity of  $13.8 \pm 0.7$  pb $^{-1}$ . A muon track satisfying the “Tight II” definition of Table II was required. Kinematic selection was made requiring  $p_T^\mu > 15$  GeV/c and  $\cancel{E}_T > 15$  GeV. To reduce background from  $Z\gamma$  events, where the  $\cancel{E}_T$  resulted from muon  $p_T$  mismeasurement, events were rejected if they contained an additional muon track with  $p_T^\mu > 8$  GeV/c.

The requirements on photons were the same for both the electron and muon samples. The photon was required to have  $E_T^\gamma \geq 10$  GeV. The separation between the photon and charged lepton,  $\Delta\mathcal{R}_{\ell\gamma}$ , was required to be  $\geq 0.7$ . This requirement suppressed the contribution of the final state radiation process, and minimized the probability for a photon cluster to merge with a nearby calorimeter cluster associated with an electron or a muon. The above selection criteria yielded 11  $W(e\nu)\gamma$  candidates and 12  $W(\mu\nu)\gamma$  candidates.

## B. Efficiencies

The trigger and offline lepton selection efficiencies, shown in Table VI, were primarily determined using  $Z \rightarrow \ell\ell$  events, requiring only one of the leptons to pass the trigger and selection criteria. Thus the second lepton provided an unbiased sample to measure efficiencies. The efficiency for the  $\cancel{E}_T$  requirement of the ELE-MAX trigger was calculated using the events which passed the ELE-HIGH trigger, which had no  $\cancel{E}_T$  requirement. The detection efficiency of the photons with  $E_T > 25$  GeV was determined using electrons from  $Z$  decays. For photons with lower  $E_T$  there was a decrease in detection efficiency due to the cluster shape requirement, determined using test beam electrons, and the isolation requirement, which was determined by measuring the energy in a cone of radius  $\mathcal{R} = 0.4$  rotated randomly in azimuth in the inclusive  $W(e\nu)$  sample. Combining this  $E_T$ -dependent efficiency with the probability of losing a photon due to  $e^+e^-$  pair conversion, 0.10 (0.26) in the CC (EC), and due to an overlap with a random track in the event, with probability 0.065 (0.155), the overall photon selection efficiency was estimated to be  $0.43 \pm 0.04$  ( $0.38 \pm 0.03$ ) at  $E_T^\gamma = 10$  GeV which increased to  $0.74 \pm 0.07$  ( $0.58 \pm 0.05$ ) for  $E_T^\gamma > 25$  GeV.

The kinematic and geometrical acceptance was calculated as a function of coupling parameters using the Monte Carlo program of Baur and Zeppenfeld [10], in which the  $W\gamma$  production and radiative decay processes were generated to leading order, and higher order QCD effects were approximated by a K-factor of 1.34. The MRSD-’ structure functions [27] were used and the  $p_T$  distribution of the  $W\gamma$  system was simulated using the observed  $p_T$  spectrum of the  $W$  in the inclusive  $W(e\nu)$  sample. Table VI lists the acceptances for the SM production of  $W(\ell\nu)\gamma$ .

	$W(e\nu)\gamma$ $E_T(e) > 25$ GeV		$W(\mu\nu)\gamma$ $p_T(\mu) > 15$ GeV/c	
	$ \eta  < 1.1$	$1.5 <  \eta  < 2.5$	$ \eta  < 1.0$	$1.0 <  \eta  < 1.7$
$\epsilon_{trig}$	$0.98 \pm 0.02$	$0.98 \pm 0.02$	$0.74 \pm 0.06$	$0.35 \pm 0.14$
$\epsilon_\ell$	$0.79 \pm 0.02$	$0.78 \pm 0.03$	$0.54 \pm 0.04$	$0.22 \pm 0.07$
$\epsilon_{Acc}^{SM}$	$0.11 \pm 0.01$		$0.29 \pm 0.02$	

TABLE VI. Summary of trigger ( $\epsilon_{trig}$ ) and lepton selection ( $\epsilon_\ell$ ) efficiencies and geometrical acceptances ( $\epsilon_{Acc}^{SM}$ ) for the SM  $W\gamma$  production events.

## C. Backgrounds

The background estimate, summarized in Table VII, included contributions from:  $Z\gamma$ , where the  $Z$  decays to  $\ell\ell$ , and one of the leptons was undetected or was mismeasured by the detector and contributed to  $\cancel{E}_T$ ;  $W\gamma$  with  $W \rightarrow \tau\nu$  followed by  $\tau \rightarrow \ell\nu\bar{\nu}$ ; and  $W + \text{jet(s)}$ , where a jet was misidentified as a photon. The backgrounds due to  $Z\gamma$  were estimated using the  $Z\gamma$  event generator of Baur and Berger [18] followed by a full detector simulation using the GEANT program [22]. It should be noted that  $\sigma(Z(\ell\ell)\gamma)/\sigma(W(\ell\nu)\gamma)$  is about 0.5 (rather than 0.1 which is the ratio of cross sections of  $Z \rightarrow \ell\ell$  and  $W \rightarrow \ell\nu$ ), since the  $W(\ell\nu)\gamma$  process is suppressed by interference between the production diagrams and since the  $Z$  boson has twice as many leptons from which a photon can be radiated. The background due to  $W\gamma \rightarrow (\tau\nu)\gamma$  was estimated from the ratio of the detection efficiencies of  $W \rightarrow \tau\nu \rightarrow e\nu\bar{\nu}$  and  $W \rightarrow e\nu$  processes. The ratio was found to be  $0.019 \pm 0.002$ , using the ISAJET [24] event generator followed by the GEANT detector simulation.

The  $W + \text{jets}$  background was estimated using the probability,  $\mathcal{P}(j \rightarrow \gamma)$ , for a jet to be misidentified as a photon. The probability was determined as a function of  $E_T$  of the jet by measuring the fraction of jets in a sample of multi-jet events that passed the photon identification requirements. Of course, some of the “fake rate” was due to real photons in the jet sample. The fraction of direct photon events in the multi-jet sample was estimated using the differences in the transverse and longitudinal shower shapes of multiple photons from meson decays and single photons [28]. In the  $E_T$  range 10 to 50 GeV,  $25\% \pm 25\%$  of the “fake” photons in the background sample were attributed



to direct photons. This fraction was subtracted from  $\mathcal{P}(j \rightarrow \gamma)$ . The misidentification probability was found to be  $\mathcal{P}(j \rightarrow \gamma) \sim 4 \times 10^{-4}$  ( $\sim 6 \times 10^{-4}$ ) in the CC (EC) in the  $E_T$  region between 10 and 40 GeV. The measured probability, before direct photon subtraction, for a jet to mimic a photon is shown in Fig. 17.

The total numbers of  $W$  + jets background events were estimated to be  $1.7 \pm 0.9$  and  $1.3 \pm 0.7$  for  $W(e\nu)\gamma$  and  $W(\mu\nu)\gamma$ , respectively, by applying  $\mathcal{P}(j \rightarrow \gamma)$  to the observed  $E_T$  spectrum of jets in the inclusive  $W(\ell\nu)$  sample. The uncertainty on the background estimates was dominated by the uncertainty on  $\mathcal{P}(j \rightarrow \gamma)$  due to the direct photon subtraction. Bias in the  $W$  + jets background estimate due to a possible difference in jet fragmentation (e.g. the number of  $\pi^0$ 's in a jet) between jets in the  $W$  sample and those in the multi-jet sample was investigated by parameterizing  $\mathcal{P}(j \rightarrow \gamma)$  as a function of the EM energy fraction of the jet. No statistically significant difference was found between the background estimates with and without the parametrization. The estimated  $W$  + jets background also included the background from  $\ell$ +jets, where  $\ell$  was a jet misidentified as an electron, a cosmic ray muon or a fake muon track, since it was derived from the observed inclusive  $W \rightarrow \ell\nu$  event sample.

Other backgrounds considered and found to be negligible included those from single photon events where a jet was misidentified as an electron, and  $ee + X$  events where an electron was misidentified as a photon due to tracking inefficiency.

	$W(e\nu)\gamma$	$W(\mu\nu)\gamma$
Source:		
$W$ + jets	$1.7 \pm 0.9$	$1.3 \pm 0.7$
$Z\gamma$	$0.11 \pm 0.02$	$2.7 \pm 0.8$
$W(\tau\nu)\gamma$	$0.17 \pm 0.02$	$0.4 \pm 0.1$
Total Background	$2.0 \pm 0.9$	$4.4 \pm 1.1$
Data	11	12

TABLE VII. Summary of  $W(e\nu)\gamma$  and  $W(\mu\nu)\gamma$  data and backgrounds.

#### D. Cross section and limits on the coupling parameters

After subtraction of the estimated backgrounds from the observed number of events, the number of signal events was found to be

$$N^{W(e\nu)\gamma} = 9.0^{+4.2}_{-3.1} \pm 0.9, \quad N^{W(\mu\nu)\gamma} = 7.6^{+4.4}_{-3.2} \pm 1.1,$$

where the first uncertainty is statistical, calculated following the prescription for Poisson processes with background given in Ref. [29], and the second is systematic.

Using the acceptance for SM couplings of  $0.11 \pm 0.01$  for  $W(e\nu)\gamma$  and  $0.29 \pm 0.02$  for  $W(\mu\nu)\gamma$  and the efficiencies quoted above, the  $W\gamma$  cross section (for photons with  $E_T^\gamma > 10$  GeV and  $\Delta\mathcal{R}_{\ell\gamma} > 0.7$ ) was calculated from a combined  $e + \mu$  sample:

$$\sigma(W\gamma) = 138^{+51}_{-38}(\text{stat}) \pm 21(\text{syst}) \text{ pb},$$

where the systematic uncertainty includes the uncertainties in the  $e/\mu/\gamma$  efficiencies, the choice of the structure functions and the  $Q^2$  scale at which the structure functions are evaluated, the  $p_T$  distribution of the  $W\gamma$  system, and the integrated luminosity calculation. The systematic uncertainties from the sources other than trigger and lepton selection efficiencies and geometrical acceptances are listed in Table VIII. The measured cross section agrees with the SM prediction of  $\sigma_{W\gamma}^{SM} = 112 \pm 10$  pb within the uncertainty. Figure 18 shows the data and the SM prediction plus the background in the distributions of  $E_T^\gamma$ ,  $\Delta\mathcal{R}_{\ell\gamma}$ , and the three-body “cluster” transverse mass defined by  $M_T(\gamma\ell; \nu) = [((m_{\gamma\ell}^2 + |\mathbf{E}_T^\gamma + \mathbf{E}_T^\ell|^2)^{\frac{1}{2}} + \cancel{E}_T)^2 - |\mathbf{E}_T^\gamma + \mathbf{E}_T^\ell + \mathbf{E}_T|]^{\frac{1}{2}}$ . Final state radiation events and background events composed most of the expected signal with  $M_T(\gamma\ell; \nu) \leq M_W$ . Of the 23 observed events, 11 events had  $M_T(\gamma\ell; \nu) \leq M_W$ .

	Uncertainty
Luminosity	5.4%
Structure Function choice	6.0%
$P_T^{W\gamma}$	3.9%
Conversion Probability	5.0%
Random track overlap	1.0%
Photon selection efficiency	7.0%
Total	12.5%

TABLE VIII. The values of systematic uncertainties in the  $W\gamma$  cross section and coupling limit measurements, other than those of trigger, lepton selection and acceptance.

To set limits on the anomalous coupling parameters, a binned maximum likelihood fit was performed on the  $E_T^\gamma$  spectrum for each of the  $W(e\nu)\gamma$  and  $W(\mu\nu)\gamma$  samples, by calculating the probability for the sum of the Monte Carlo prediction and the background to fluctuate to the observed number of events (see Appendix 2 for more detail). The uncertainties in background estimate, efficiencies, acceptance and integrated luminosity were convoluted in the likelihood function as Gaussian distributions. A dipole form factor with a scale  $\Lambda = 1.5$  TeV was assumed for the anomalous couplings in the Monte Carlo event generation. The Monte Carlo events were generated at  $11 \times 11$  grid points of the CP-conserving anomalous coupling parameters,  $\Delta\kappa_\gamma$  and  $\lambda_\gamma$ , assuming that the CP-violating anomalous coupling parameters  $\tilde{\kappa}_\gamma$  and  $\tilde{\lambda}_\gamma$  are zero. The limit contours for  $\Delta\kappa_\gamma$  and  $\lambda_\gamma$  are shown in Fig. 19. The numerical values of the limits at the 95% confidence level (CL) were

$$-1.6 < \Delta\kappa_\gamma < 1.8 \ (\lambda_\gamma = 0), \quad -0.6 < \lambda_\gamma < 0.6 \ (\Delta\kappa_\gamma = 0)$$

for  $\hat{s} = 0$  (i.e. the static limit). The  $U(1)_{EM}$ -only coupling of the  $W$  boson to a photon, which leads to  $\kappa_\gamma = 0$  ( $\Delta\kappa_\gamma = -1$ ) and  $\lambda_\gamma = 0$ , and thereby,  $\mu_W = e/2m_W$  and  $Q_W^e = 0$  [30], was excluded at the 80% CL, while the zero magnetic moment ( $\mu_W = 0$ ) was excluded at more than the 95% CL. Similarly, limits on CP-violating coupling parameters were obtained as  $-1.7 < \tilde{\kappa}_\gamma < 1.7$  ( $\tilde{\lambda}_\gamma = 0$ ) and  $-0.6 < \tilde{\lambda}_\gamma < 0.6$  ( $\tilde{\kappa}_\gamma = 0$ ) at the 95% CL. The form factor scale dependence of the results was studied. It was found that the limits were insensitive to the values of the form factor scale for  $\Lambda > 200$  GeV and were well within the constraints imposed by S-matrix unitarity [31] for  $\Lambda = 1.5$  TeV. A simultaneous fit to  $E_T^\gamma$  and the  $\Delta\mathcal{R}_{\ell\gamma}$  spectra was performed. It was found that the results were within 3% of those obtained from a fit to the  $E_T^\gamma$  spectrum only.

## VI. $WW \rightarrow$ DILEPTONS

In this section the results of a search for  $p\bar{p} \rightarrow WW + X \rightarrow \ell\bar{\ell}'\nu\nu' + X$ , where the leptons included muons and electrons, are presented. The signal and background were estimated and an upper limit was set for the cross section of the SM process. Anomalous  $WWZ$  and  $WW\gamma$  couplings would have enhanced the expected  $WW$  cross section by upsetting the cancellation [14] between the production diagrams and the trilinear diagram as seen in Fig. 4, which shows the cross section *vs* anomalous couplings for  $\Lambda = 1000$  GeV. The detection efficiency also increases with anomalous couplings because of the higher average  $E_T$  of the  $W$  bosons (see Fig. 5), resulting in a higher average  $E_T$  for leptons and in more central events. This expected increase in the cross section and efficiency was exploited to set limits on the anomalous coupling parameters,  $\lambda$  and  $\Delta\kappa$ .

The expected signature for  $W$  boson pair production with subsequent decay to dileptons was two high- $p_T$  isolated leptons in association with large  $\cancel{E}_T$ . The major sources of background were the following: events with a  $W + \text{jet(s)}$  where a jet was misidentified as a lepton;  $W + \gamma$  events where a photon was misidentified as an electron; QCD multi-jet events where two jets were misidentified as leptons;  $Z \rightarrow \ell\ell$ ,  $Z \rightarrow \tau\tau \rightarrow \ell\ell'\nu\nu\bar{\nu}\bar{\nu}$  events; and  $t\bar{t} \rightarrow \ell\ell' + X$  events. The event selection requirements were designed to reduce these backgrounds while retaining high detection efficiency for signal events. The selection requirements were slightly different for the  $ee$ ,  $e\mu$ , and  $\mu\mu$  channels because the electrons had a better  $p_T$  resolution but a larger background contamination than muons. In what follows, the analyses of individual channels and our limits on the cross section for  $W$  boson pair production as well as on the anomalous gauge boson trilinear couplings are presented.

## A. The $ee$ channel

The  $WW \rightarrow ee\nu\bar{\nu}$  candidate events were selected from the data sample recorded using the ELE-2-HIGH trigger which required two EM clusters with  $E_T > 7$  GeV at level 1 and two isolated EM clusters with  $E_T > 10$  GeV at level 2 (see Table I). Candidate events containing two electrons that passed the “Tight I” requirements were selected. The “Tight I” requirements discussed in Section II, and detailed in Table III, provided the largest rejection of fake electrons. The following event selection requirements were then imposed. Both electrons were required to have a large transverse energy ( $E_T \geq 20$  GeV); at this stage the remaining sample of 605 events was comprised primarily of  $Z$  bosons. The  $\cancel{E}_T$  of the event was then required to be  $\geq 20$  GeV. These first two selection criteria strongly reduced the background due to QCD fakes. The dielectron invariant mass was required to be outside of the  $Z$  boson mass window (between 77 and 105 GeV/ $c^2$ ). The  $\cancel{E}_T$  and dielectron invariant mass selections had very strong rejection ( $> 100$ ) of  $Z \rightarrow ee$  decays. The background from  $Z \rightarrow \tau\tau \rightarrow ee\nu\bar{\nu}$  which was not eliminated by the electron  $p_T$  thresholds was further reduced by requiring that the  $\cancel{E}_T$  not be collinear with the direction of the lower energy electron; it was required that  $20^\circ \leq \Delta\phi(p_T^e, \cancel{E}_T) \leq 160^\circ$  for the lower energy electron if  $\cancel{E}_T \leq 50$  GeV. Releasing this requirement for events with large  $\cancel{E}_T$  increased the acceptance for  $W$  boson pairs in a region where the  $Z$  boson background was very small. This can be seen in Fig. 20 which shows  $\Delta\phi(p_T^e, \cancel{E}_T)$  vs  $\cancel{E}_T$  distributions for  $W$  boson pairs,  $Z \rightarrow ee$  and  $Z \rightarrow \tau\tau \rightarrow ee\nu\bar{\nu}$ . Finally, the sum of the  $E_T$  of the recoiling hadrons ( $\vec{E}_T^{\text{had}}$ ), defined as  $-(\vec{E}_T^{l1} + \vec{E}_T^{l2} + \vec{\cancel{E}}_T)$  was required to be less than 40 GeV in magnitude. The background from  $t\bar{t}$  production was effectively eliminated by this requirement. Figure 21 shows a Monte Carlo (PYTHIA plus DØGEANT) simulation of  $\vec{E}_T^{\text{had}}$  for  $\sim 20$  fb $^{-1}$  of SM  $WW$  and  $t\bar{t}$  events. For  $WW$  events, non-zero values of  $\vec{E}_T^{\text{had}}$  were due to gluon radiation and detector resolution. For  $t\bar{t}$  events, the most significant contribution was from  $b$  quark jets from  $t$  quark decays. This selection reduced the background from  $t\bar{t}$  production by a factor of more than four for a  $t$  quark mass of 170 GeV/ $c^2$ . The efficiency of this selection criterion for SM  $W$  boson pair production events was  $0.95^{+0.01}_{-0.04}$  and decreased slightly with increasing  $W$  boson pair invariant mass. The systematic uncertainty in the efficiency of this last selection criteria, included in the uncertainties presented, was estimated from the difference between  $\vec{E}_T^{\text{had}}$  for  $Z$  boson data and Monte Carlo (PYTHIA plus DØGEANT) distributions.

Table IX shows the numbers of events remaining after each selection cut. One event survived all the selection criteria.

Event selection criteria	Number of events surviving
$E_T \geq 20$ GeV	605
$\cancel{E}_T > 20$ GeV	5
$M_{ee} < 77$ GeV/ $c^2$ or $M_{ee} \geq 105$ GeV/ $c^2$	3
$\Delta\phi(p_T^e, \cancel{E}_T)$ cut	1
$ \vec{E}_T^{\text{had}}  \leq 40$ GeV	1

TABLE IX. The numbers of events after each selection cut for the  $WW \rightarrow ee$  analysis.

Fiducial Region	Efficiency
CC – CC	$0.526 \pm 0.041$
CC – EC	$0.368 \pm 0.044$
EC – EC	$0.257 \pm 0.058$

TABLE X. The combined trigger and electron selection efficiency for individual fiducial regions in the  $WW \rightarrow ee$  analysis for SM  $W$  pair production.

The integrated luminosity of the data sample was  $14.3 \pm 0.8$  pb $^{-1}$ . The trigger efficiency was calculated with the TRIGSIM simulation package to be  $\epsilon_{\text{trig}} = 0.989 \pm 0.002$ . The measured electron selection efficiency was used to estimate the detection efficiency for SM  $WW \rightarrow ee\nu\bar{\nu}$  events. The geometrical acceptance was obtained from a PYTHIA and DØGEANT Monte Carlo simulation. These efficiencies for individual fiducial regions are listed in Table X. The overall detection efficiency for SM  $W$  pair events was estimated to be  $\epsilon_{ee} = 0.094 \pm 0.008$ . The expected number of events  $N_{ee}^{SM}$  was  $N_{ee}^{SM} = 0.149 \pm 0.013(\text{stat}) \pm 0.019(\text{sys})$ , using the next-to-leading order cross section [13], and branching fraction  $\text{Br}(W \rightarrow e\nu) = 0.108 \pm 0.004$  [32].

The backgrounds from  $W\gamma$ , Drell-Yan dilepton,  $Z \rightarrow \tau\tau \rightarrow ee\nu\bar{\nu}\nu\bar{\nu}$  and  $t\bar{t}$  processes were estimated using the PYTHIA and ISAJET Monte Carlo event generators followed by the DØGEANT detector simulation. The  $t\bar{t}$  cross

section estimates were from the calculations of Laenen *et al.* [33]. The  $t\bar{t}$  background was averaged for  $M_{\text{top}} = 160, 170, \text{ and } 180 \text{ GeV}/c^2$ . The production and decay of  $Z$  bosons was modeled using the double differential (in rapidity and  $p_T$ ) cross section calculated at next-to-leading order [34], and a fast detector simulation of the type discussed in Section III A. The line shape of the  $Z$  boson was taken to be a relativistic Breit-Wigner function. The kinematic distributions were compared with the  $Z$  boson data sample and found to be consistent.

The backgrounds from  $W + \text{jet(s)}$  with a jet misidentified as an electron and multijet events with two jets misidentified as electrons were called “fake” background. The size of this background was estimated with the following method. Two sub-samples of data were derived from the full data set. One was similar to the signal sample and contained two “Tight I” electrons each with  $E_T \geq 20 \text{ GeV}$ . The other was a sample of events with at least one *bad* electron which had an H-matrix  $\chi^2 \geq 200$  and Isolation  $f_{iso} > 0.15$  (the fake sample). A normalization factor ( $F_{fake}$ ) of this fake sample relative to the signal sample was calculated using the number of events with  $\cancel{E}_T < 15 \text{ GeV}$ , which contained solely fake electrons, in both the samples. All the event selection cuts were applied to the fake sample and the number of remaining events ( $N_{fake}$ ) was counted. The fake background ( $N_{fake}^{BG}$ ) was then computed from the products of  $F_{fake}$  and  $N_{fake}$ . The result was  $N_{fake}^{BG} = 0.152 \pm 0.012(\text{stat}) \pm 0.076(\text{sys})$ . The total number of background events was estimated to be  $N_{ee}^{BG} = 0.222 \pm 0.020(\text{stat}) \pm 0.080(\text{sys})$ . Table XI contains a summary of the expected background in the  $ee$  channel.

Background	$ee$	$e\mu$	$\mu\mu$
$Z \rightarrow ee \text{ or } \mu\mu$	$0.02 \pm 0.01$	—	$0.068 \pm 0.026$
$Z \rightarrow \tau\tau$	$< 10^{-3}$	$0.11 \pm 0.05$	$< 10^{-3}$
Drell-Yan dileptons	$< 10^{-3}$	—	$< 10^{-3}$
$W\gamma$	$0.02 \pm 0.01$	$0.04 \pm 0.03$	—
QCD ( $N_{fake}^{BG}$ )	$0.15 \pm 0.08$	$0.07 \pm 0.07$	$< 10^{-3}$
$t\bar{t}$	$0.03 \pm 0.01$	$0.04 \pm 0.02$	$0.009 \pm 0.003$
Total	$0.22 \pm 0.08$	$0.26 \pm 0.10$	$0.077 \pm 0.026$

TABLE XI. Summary of the expected number of background events to  $WW \rightarrow ee\nu\bar{\nu}$ ,  $WW \rightarrow e\mu\nu\bar{\nu}$  and  $WW \rightarrow \mu\mu\nu\bar{\nu}$ . The uncertainties include both statistical and systematic contributions.

## B. The $e\mu$ channel

The  $WW \rightarrow e\mu\nu\bar{\nu}$  candidate events were selected from the data sample acquired with the MU-ELE trigger which required at least one EM tower with  $E_T > 7 \text{ GeV}$  and one muon with  $|\eta| < 1.7$  at level 1 and one EM cluster with  $E_T > 7 \text{ GeV}$  and one muon with  $p_T > 5 \text{ GeV}/c$  at level 2 (see Table I). The electron in a candidate event was required to pass “Tight I” criteria, providing the strictest rejection against fake electrons, and the muon to pass the “Loose I” criteria of Table II. The following event selection requirements were imposed. Both the electron and the muon were required to have a large transverse energy (momentum)  $E_T^e \geq 20 \text{ GeV}$  and  $p_T^\mu \geq 15 \text{ GeV}/c$ . Both  $\cancel{E}_T$  and  $\cancel{E}_T^{cal}$  of the event were required to be  $\geq 20 \text{ GeV}$ . These first two requirements provided large rejection of the background from multijet events. In order to reduce the backgrounds from  $Z \rightarrow \tau\tau \rightarrow e\mu\nu\nu\bar{\nu}$ , the  $\cancel{E}_T$  was required not to be collinear to the muon:  $20^\circ \leq \Delta\phi(p_T^\mu, \cancel{E}_T) \leq 160^\circ$  if  $\cancel{E}_T \leq 50 \text{ GeV}$ . Figure 22 shows the  $\Delta\phi(p_T^\mu, \cancel{E}_T)$  vs  $\cancel{E}_T$  distributions. Finally, the recoil hadronic  $E_T$  ( $\vec{E}_T^{\text{had}}$ ), defined as  $-(\vec{E}_T^e + \vec{E}_T^\mu + \vec{\cancel{E}}_T)$  was required to be less than  $40 \text{ GeV}$  in magnitude to reduce the background from  $t\bar{t}$  production. Table XII shows the number of events remaining after each selection cut. One event survived all the requirements but the last; this event is a candidate for  $t\bar{t}$  production and has been discussed extensively elsewhere [35].

Event selection cut	Number of events
$E_T^e \geq 20 \text{ GeV}$	9
$p_T^\mu \geq 15 \text{ GeV}$	6
$\cancel{E}_T \geq 20 \text{ GeV}$	1
$\Delta\phi(p_T^\mu, \cancel{E}_T) \text{ cut}$	1
$ \vec{E}_T^{\text{had}}  \leq 40 \text{ GeV}$	0

TABLE XII. The numbers of events remaining after each selection criteria for the  $WW \rightarrow e\nu\mu\nu$  analysis.

The integrated luminosity of the data sample was  $13.9 \pm 0.8 \text{ pb}^{-1}$ . The trigger efficiency was largely determined by the trigger efficiency for the muons and was estimated using data as was discussed in Section II. The detection efficiency for the SM  $WW \rightarrow e\mu\nu\bar{\nu}$  events, including the muon selection efficiency, the geometrical acceptance, and the event selection efficiency, was estimated using the PYTHIA and DØGEANT Monte Carlo simulation. The muon selection efficiency was implemented in the DØGEANT Monte Carlo program by introducing the measured hit efficiencies and resolutions of the muon chamber modules. The measured electron selection efficiency was implemented as a multiplicative factor after the detector simulation. The detection efficiencies, including lepton identification efficiencies, of individual fiducial regions are listed in Table XIII. The uncertainty on the efficiency for the regions involving EF muons was dominated by the statistics of the GEANT Monte Carlo simulation. The overall detection efficiency of the SM  $W$  pair events was estimated to be  $\epsilon_{e\mu} = 0.092 \pm 0.010$ . The expected number of events was estimated to be  $N_{e\mu}^{SM} = 0.283 \pm 0.031(\text{stat}) \pm 0.037(\text{sys})$ .

Fiducial Region	Efficiency
CC – CF	$0.43 \pm 0.08$
CC – EF	$0.21 \pm 0.14$
EC – CF	$0.30 \pm 0.09$
EC – EF	$0.15 \pm 0.15$

TABLE XIII. The combined efficiencies of trigger, electron and muon selection, and kinematic event selection for individual fiducial regions in the  $WW \rightarrow e\mu\nu\bar{\nu}$  analysis. The fiducial regions are those of the charged leptons.

The backgrounds from  $W\gamma$ ,  $Z \rightarrow \tau\tau \rightarrow e\mu\nu\nu\bar{\nu}$  and  $t\bar{t}$  were estimated using the PYTHIA and ISAJET Monte Carlo event generators followed by the DØGEANT detector simulation. The background due to a jet misidentified as an electron was estimated by a different method from the  $ee$  channel, since the accuracy of the estimate was limited by statistics when that method was applied to the  $e\mu$  channel. Instead, the inclusive  $W \rightarrow \mu\nu$  data were used to estimate this background. Each jet in an event was treated as an electron and the event selection requirements were applied. The events that survived the criteria were weighted by the probability of a jet being misidentified as an electron. The misidentification probabilities were measured from data to be  $P^{CC}(\text{jet} \rightarrow e) = (0.9 \pm 0.4) \times 10^{-4}$  for CC and  $P^{EC}(\text{jet} \rightarrow e) = (4.0 \pm 1.0) \times 10^{-4}$  for EC. The total “fake” background from this source was calculated to be  $N_{\text{fake}}^{BG} = 0.074 \pm 0.016(\text{stat}) \pm 0.074(\text{sys})$ . The background due to a jet faking a muon was estimated to be negligibly small. The total number of background events was estimated to be  $N_{e\mu}^{BG} = 0.264 \pm 0.052(\text{stat}) \pm 0.084(\text{sys})$ . The backgrounds to  $WW \rightarrow e\mu\nu\bar{\nu}$  are summarized in Table XI.

### C. The $\mu\mu$ channel

The  $WW \rightarrow \mu\mu\nu\bar{\nu}$  candidate events were selected from the data sample recorded with the MU-MAX trigger of Table I. This trigger required at least one muon in  $|\eta| < 1.7$  at levels 1 and 1.5 with  $p_T > 7 \text{ GeV}/c$  (threshold determined by the hardware) and one muon with  $p_T \geq 15 \text{ GeV}/c$  at level 2. Candidate events with two muons that passed “Tight I” requirements were selected. The following event selection requirements were imposed. Both muons were required to have large transverse momentum:  $p_T^{\mu 1} \geq 20 \text{ GeV}/c$  and  $p_T^{\mu 2} \geq 15 \text{ GeV}/c$ . To reduce the background from  $Z \rightarrow \mu\mu$  decays, the  $\cancel{E}_T^\eta$  was required to be  $\geq 30 \text{ GeV}$ , where  $\cancel{E}_T^\eta$  was defined as the projection of the  $\cancel{E}_T$  vector onto the bisector of the opening angle of the two muons in the transverse plane. By selecting this component of the  $\cancel{E}_T$ , it was ensured that the  $\cancel{E}_T$  was least sensitive to mismeasurements of the muon momentum. This selection requirement was also less sensitive to the momentum resolution of the muons than was a dimuon invariant mass cut. The  $\cancel{E}_T$  was required not to be collinear to the higher momentum muon:  $\Delta\phi(p_T^{\mu 1}, \cancel{E}_T) \leq 170^\circ$ . This reduced the background from  $Z \rightarrow \tau\tau \rightarrow \mu\mu\nu\nu\bar{\nu}$ . Figure 23 shows  $\Delta\phi(p_T^\mu, \cancel{E}_T)$  vs  $\cancel{E}_T$  distributions. The recoil hadronic  $E_T$  ( $\vec{E}_T^{\text{had}}$ ), defined as  $-(\vec{E}_T^{\mu 1} + \vec{E}_T^{\mu 2} + \vec{\cancel{E}}_T)$  was required to be less than 40 GeV in magnitude, rejecting  $t\bar{t}$  as in the other two channels. Even though the  $p_T$  resolution of the muons was worse than that of the electrons, the resolution of this variable was the same in all three channels since the mismeasurement of the leptons cancels when taken in a vector sum with the  $\cancel{E}_T$ . Table XIV shows the numbers of events after each selection cut. No event survived all the selection cuts.

Event selection cut	Number of events
$p_T^{\mu 1} \geq 20$ GeV/c	102
$p_T^{\mu 2} \geq 15$ GeV	88
$E_T^\eta \geq 30$ GeV	0
$\Delta\phi(p_T^{\mu 1}, E_T) \leq 170^\circ$	0
$ \vec{E}_T^{had}  \leq 40$ GeV	0

TABLE XIV. The number of events remaining after each selection criteria for the  $WW \rightarrow \mu\mu\nu\bar{\nu}$  analysis.

Fiducial Region	Efficiency
CF – CF	$0.023 \pm 0.006$
CF – EF	$0.009 \pm 0.002$
EF – EF	$0.0010 \pm 0.0006$

TABLE XV. The combined efficiencies of trigger and muon selection for individual fiducial regions in the  $WW \rightarrow \mu\mu\nu\bar{\nu}$  analysis. CF–CF is, for instance, the case that both muons were in the central region.

The integrated luminosity of the data sample was  $12.2 \pm 0.7$  pb $^{-1}$ . The trigger efficiency was measured using data. The detection efficiency for the SM  $WW \rightarrow \mu\mu\nu\bar{\nu}$  events that included the muon selection efficiency, the geometrical acceptance and the event selection efficiency was estimated using the PYTHIA and DØGEANT Monte Carlo simulation. The muon selection efficiency was implemented in the DØGEANT Monte Carlo program by introducing the measured hit efficiencies and resolutions of the muon chamber modules as in the  $e\mu$  channel. The efficiencies of individual fiducial regions are listed in Table XV. The overall detection efficiency for the SM  $W$  pair events was estimated to be  $\epsilon_{\mu\mu} = 0.033 \pm 0.006$ . The expected number of events was estimated to be  $N_{\mu\mu}^{SM} = 0.045 \pm 0.004(\text{stat}) \pm 0.006(\text{sys})$ .

The backgrounds from Drell-Yan dilepton,  $Z \rightarrow \tau\tau \rightarrow \mu\mu\nu\bar{\nu}\bar{\nu}$  and  $t\bar{t}$  processes were estimated using the PYTHIA and ISAJET Monte Carlo event generators followed by the DØGEANT detector simulation. The background from  $Z \rightarrow \mu\mu$  was estimated using the same fast simulation program as in the  $ee$  channel. The fake background due to a jet faking a muon was negligibly small. The total number of background events was estimated to be  $N_{\mu\mu}^{BG} = 0.077 \pm 0.023(\text{stat}) \pm 0.012(\text{sys})$ .

#### D. Limit on the cross section for $W$ boson pair production

The results from the analyses of the  $ee$ ,  $e\mu$  and  $\mu\mu$  channels are summarized in Table XVI. For the three channels combined, the expected number of events for SM  $W$  boson pair production, based on a cross section of  $9.5 \pm 1.0$  pb [13], was  $0.47 \pm 0.07$ . In approximately 14 pb $^{-1}$  of data, one event was found with an expected background of  $0.56 \pm 0.13$  events.

Channel	$ee$	$e\mu$	$\mu\mu$	Total
Efficiency	$0.094 \pm 0.008$	$0.092 \pm 0.010$	$0.033 \pm 0.006$	
$N^{SM}$	$0.15 \pm 0.01 \pm 0.02$	$0.28 \pm 0.03 \pm 0.04$	$0.045 \pm 0.004 \pm 0.006$	$0.47 \pm 0.03 \pm 0.06$
$N^{BG}$	$0.22 \pm 0.02 \pm 0.06$	$0.26 \pm 0.05 \pm 0.08$	$0.077 \pm 0.023 \pm 0.012$	$0.56 \pm 0.06 \pm 0.10$
$N^{observed}$	1	0	0	1

TABLE XVI. The summary of  $WW \rightarrow$  dileptons analyses including the efficiency, number of SM events expected, expected backgrounds, and number of candidates observed.

The 95% confidence level upper limit on the  $W$  boson pair production cross section was estimated based on one observed event, taking into account the expected background of  $0.56 \pm 0.13$  events. Poisson-distributed numbers of events were convoluted with Gaussian uncertainties on the detection efficiencies, background and luminosity. For SM  $W$  boson pair production, the upper limit for the cross section was 87 pb at the 95% confidence level.

## E. Limits on the trilinear gauge boson couplings

The limit on the  $W$  boson pair production cross section can be translated into limits on the anomalous gauge boson couplings. The Monte Carlo program of Ref. [15] followed by a fast detector simulation was used to estimate [36] the detection efficiency for  $W$  boson pair production as a function of the coupling parameters  $\lambda$  and  $\Delta\kappa$ . It was assumed that the  $W$  boson couplings to the photon and to the  $Z$  boson were equal:  $\lambda \equiv \lambda_\gamma = \lambda_Z$  and  $\Delta\kappa \equiv \Delta\kappa_\gamma = \Delta\kappa_Z$ . The form factor scale  $\Lambda = 900$  GeV was chosen. This was the highest value of  $\Lambda$  that produced anomalous coupling limits within the corresponding unitarity bound in this analysis. For smaller values of  $\Lambda$ , the anomalous coupling limits are looser (see Appendix 1). The MRSD-’ parton distribution functions were used in the event generation.

The number of  $W$  boson pair events expected at each point in a grid of  $\lambda$  and  $\kappa$ , including SM production, was fitted to the following equation which reflected the general Lagrangian form of gauge boson self-interactions:

$$N(\Delta\kappa, \lambda) = a_1 + a_2\Delta\kappa + a_3(\Delta\kappa)^2 + a_4\lambda + a_5(\lambda)^2 + a_6\lambda\Delta\kappa,$$

where the  $a_i$  were parameters determined from the fit. A 95% CL limit contour on the coupling parameters  $\Delta\kappa$  and  $\lambda$  was formed by intersecting the parabolic surface of expected number of events with the plane of the 95% CL upper limit on the observed number of events (with the background subtracted), fluctuated by Gaussian uncertainties on the detection efficiencies, backgrounds, and luminosity and by the Poisson uncertainty on the statistics of the observation. The 95% CL upper limits on the coupling parameters are shown in Fig. 24 (solid line). Also shown in Fig. 24 (dotted line) is the contour of the unitarity constraint on the coupling limits for the form factor scale  $\Lambda = 900$  GeV. This value of  $\Lambda$  was chosen so that the observed coupling limits lie within this ellipse. The limits on the CP-conserving anomalous coupling parameters were  $-2.6 < \Delta\kappa < 2.8$  ( $\lambda = 0$ ) and  $-2.1 < \lambda < 2.1$  ( $\Delta\kappa = 0$ ). The limits for the CP-violating parameters,  $\tilde{\kappa}$  and  $\tilde{\lambda}$ , were similar. The limits on  $\lambda$  and  $\Delta\kappa$  exhibited almost no correlation, in contrast to limits from the  $W\gamma$  analyses presented in Section V and in Refs. [11,12].

## VII. SEARCH FOR ANOMALOUS $WW$ AND $WZ$ PRODUCTION IN THE $e\nu$ JET JET CHANNEL

In this section, a search for anomalous  $WW$  and  $WZ$  production is presented. The method was to identify  $WW$  and  $WZ$  candidates where one  $W$  boson decayed to an electron and a neutrino and the  $Z$  boson or other  $W$  boson decayed to two jets. The expected cross section times branching fraction for the SM  $WW$  and  $WZ$  processes ( $\sim 1.6$  pb) was much smaller than that expected from the  $W$  boson plus dijet background ( $\sim 76$  pb) [37], which had similar characteristics. Rather than isolating the SM signal, limits were set on the anomalous couplings by comparing the characteristics of the events with those expected from non-SM couplings. Figure 5 shows the  $p_T$  of the  $W$  bosons for SM  $WW$  production and for  $WW$  production with anomalous trilinear couplings. Anomalous couplings lead to a dramatic increase in the cross section at high  $p_T(W)$ . To exploit this, the  $p_T$  of  $W$  bosons in the candidate events was measured, the contribution of the backgrounds to that spectrum was estimated, and the data were compared with the sum of the background plus the expectations for the signal for various anomalous couplings.

### A. Event Selection and Efficiency

The  $WW(WZ) \rightarrow e\nu jj$  candidates were selected by searching the data which passed the ELE-HIGH trigger (see Table I) for events with a high  $E_T$  electron accompanied by significant  $\cancel{E}_T$  and at least two jets consistent with  $W \rightarrow jj$  or  $Z \rightarrow jj$ . Events with electrons which satisfied the “Tight IV” criteria within  $|\eta| < 2.5$  and with  $E_T > 25$  GeV were chosen. The  $\cancel{E}_T$  was required to be greater than 25 GeV, and at least two jets were demanded, each with  $E_T > 20$  GeV and  $|\eta| < 2.5$ . A small jet cone size,  $\mathcal{R} < 0.3$ , was used to ensure that the two jets from the  $W$  or  $Z$  decay, close together for high- $p_T$   $W$  or  $Z$  bosons, were resolved into distinct jets. After the jets were identified, a cleanup algorithm was applied to remove events with “fake” jets due to noisy cells or badly mismeasured jets, which occurred primarily in the intercryostat region. Figure 25 shows the transverse mass of the electron and  $\cancel{E}_T$ ,  $M_T^{e\nu}$ , for the candidates which survived the preceding selection criteria.  $M_T^{e\nu}$  was required to be greater than 40 GeV/c<sup>2</sup>. The dijet invariant mass distribution of these events is shown in Fig. 26. In case there were more than two jets with  $E_T > 20$  GeV in the fiducial region, the combination yielding the largest invariant mass was taken to be the dijet mass of the candidate  $W$  or  $Z$  boson. Requiring the dijet invariant mass to be  $50 < m_{jj} < 110$  GeV/c<sup>2</sup> yielded 84 candidate events.

The efficiency for identifying two separated jets depended on the  $p_T$  of the  $W$  boson. For  $p_T(W) < 125$  GeV/c, the efficiency was dominated by the jet  $E_T$  threshold. For  $p_T(W) > 350$  GeV, the efficiency was dominated by the probability for the two jets to merge into one in the reconstruction process (hence the use of the small cone size). Using the ISAJET and PYTHIA event generators, followed by the detailed detector simulation, DØGEANT, and the Shower Library described in Section III A, the efficiency for reconstructing  $W \rightarrow jj$  was estimated as a function of  $p_T(W)$ , including the jet-finding efficiency and the efficiency for the dijet mass requirement. The  $Z \rightarrow jj$  reconstruction efficiency was obtained in a similar manner. From the Monte Carlo it was determined that the use of the two highest  $E_T$  jets to form the dijet mass was the correct assignment 90% of the time. Figure 27 shows the efficiency for the dijet reconstruction of  $W \rightarrow jj$  as a function of  $p_T(W)$  for events generated with ISAJET and PYTHIA. For the efficiency, the results from the ISAJET simulation were used because they were smaller than the efficiencies determined from PYTHIA; the difference (9%) was included in the systematic uncertainty for the efficiency.

The overall efficiency was calculated for SM and anomalous couplings using the fast detector simulation described in Section III along with the  $WW$  ( $WZ$ ) generator [15]. The reconstruction efficiencies for  $W$  and  $Z$  boson decays to dijets were incorporated as look-up tables. The  $p_T$  distribution of the  $WW$  and  $WZ$  systems was included in the simulation by using the observed  $p_T(Z)$  spectrum from the inclusive  $Z \rightarrow ee$  sample. The uncertainty in the absolute jet energy scale and in the jet corrections, 10%, was included in the systematic uncertainty by recalculating the results shifting the jet energies within their uncertainty. Other sources of uncertainty included: 6% for the uncertainty in the resolution of the  $\cancel{E}_T$  and 4% for the uncertainty in the electron identification efficiency. All of the uncertainties in the efficiency are listed in Table XVII.

Source	Uncertainty (%)
Statistical	1
Electron Efficiency	4
$\cancel{E}_T$ Smearing	6
Jet Energy Scale	6
Jet Reconstruction Efficiency	9
Total	13

TABLE XVII. Summary of systematic uncertainties for the  $WW/WZ \rightarrow e\nu jj$  analysis.

The total efficiency for the detection of SM  $WW$  and  $WZ$  events was estimated to be  $0.15 \pm 0.02$  and  $0.16 \pm 0.02$ , respectively. Therefore the total number of expected (SM) signal was  $3.2 \pm 0.6$  events where  $2.8 \pm 0.64$  events were  $WW$  and  $0.4 \pm 0.1$  events were  $WZ$ , including the uncertainties in the efficiency and luminosity.

## B. Background Estimate

The background included contributions from the following:  $W+ \geq 2$  jets;  $t\bar{t}$  production with subsequent decay to  $W^+W^-b\bar{b}$ , where the top mass was assumed to be 180 GeV/c<sup>2</sup>;  $WW(WZ)$  production with  $W \rightarrow \tau\nu$  followed by  $\tau \rightarrow e\nu\bar{\nu}$ ;  $ZX \rightarrow eeX$ , where one electron was mismeasured or not identified; and multijet events, where one or more jets was misidentified as an electron and there was significant  $\cancel{E}_T$  due to mismeasurement or the presence of neutrinos.

The multijet background was estimated following the same procedure used in the  $WW \rightarrow ee\nu\bar{\nu}$  channel. The background sample was comprised of events which contained a jet with an EM fraction greater than 0.9 within the electron fiducial region and a matching track. However, these electron candidates satisfied at least one of the following three electron “anti-identification” criteria:  $f_{\text{iso}} > 0.15$ , H-matrix  $\chi^2 > 250$ , or track match significance,  $TMS > 10$ . The number of events in the region  $0 < \cancel{E}_T < 15$  GeV/c was used to normalize the fake sample to the signal sample. This was done after all selections except for the dijet mass cut. Then the dijet mass selection criterion was applied to the fake sample to determine the number of background events. The possible signal contamination of the fake sample was included as a 7% systematic uncertainty in the normalization of the fake background. A systematic uncertainty of 3.4% comes from the variation in the fake event normalization when the upper end of the normalization region was varied in the range 12 to 18 GeV. An uncertainty of 4% arose from variation of the  $\cancel{E}_T$  threshold of the signal over the range 22 to 28 GeV. Figure 28 shows the  $\cancel{E}_T$  for the QCD background and for the signal candidates before the dijet mass selection.

The backgrounds from  $t\bar{t}$ ,  $WW, WZ \rightarrow \tau\nu jj$  and  $ZX \rightarrow eeX$  were estimated from DØGEANT simulation of PYTHIA and ISAJET events. The background from  $W+ \geq 2$  jets came from VECBOS [38] generated events carried through a hybrid detector simulation which combined the DØGEANT detector simulation with the parton-



based jet Shower Library. The normalization of the  $W + \geq 2$  jets background, made before the dijet mass selection, was determined from the comparison of the number of candidate events outside the dijet mass window with that expected from the VECBOS Monte Carlo, after subtracting the multijet backgrounds and expected SM signal. The systematic uncertainty in the  $W + \geq 2$  jets background included contributions from uncertainty in the fake normalization amounting to 7%; variation when the dijet mass window was increased in width to  $40 < m_{jj} < 120$  GeV/c<sup>2</sup>, amounting to 10%; and variation in the background when the Monte Carlo jet energy scale was increased by 10%, amounting to 11%. The cross section for the resulting  $W + \geq 2$  jets background agreed within 1.5% of the VECBOS expectation. The background estimate is summarized in Table XVIII.

Background Source	Number of Expected Events	
	Before Dijet Mass Cut	After Dijet Mass Cut
$W + \geq 2$ jets	$125.4 \pm 25.9$	$62.2 \pm 13.0$
$t\bar{t}$	$3.42 \pm 0.47$	$0.87 \pm 0.12$
$WW, WZ \rightarrow \tau\nu jj$	$0.24 \pm 0.02$	$0.22 \pm 0.02$
$ZX \rightarrow eeX$	$0.00^{+0.34}_{-0.00}$	-
multijets	$30.0 \pm 4.5$	$12.2 \pm 2.6$
Total Background	$159 \pm 26$	$75.8 \pm 13.3$
SM $WW + WZ$ Prediction	$3.4 \pm 0.6$	$3.2 \pm 0.6$
Data	166	84

TABLE XVIII. Summary of  $WW(WZ) \rightarrow e\nu jj$  backgrounds and data.

The distributions in  $p_T(e\nu)$  of the final event sample, and for the  $W + \geq 2$  jets background, the total background, the SM  $WW$  and  $WZ$  Monte Carlo, and the  $WW$  and  $WZ$  Monte Carlo for a non-SM value of the couplings ( $\Delta\kappa_Z = \Delta\kappa_\gamma = 2$ ,  $\lambda_Z = \lambda_\gamma = 1.5$ ) are shown in Fig. 29. The  $p_T$  spectrum was consistent with that expected from the background. The highest  $p_T$  event, important in setting anomalous coupling limits, had  $p_T(e\nu) = 186 \pm 20$  GeV/c. There were no other candidates with  $p_T(e\nu) \geq 100$  GeV/c.

Using the detection efficiencies for SM  $WW$  and  $WZ$  production and the background-subtracted signal, and assuming the SM ratio of cross sections for  $WW$  and  $WZ$  production, an upper limit at the 95% confidence level (CL) on the cross section  $\sigma(p\bar{p} \rightarrow W^+W^-X)$  of 183 pb was determined.

### C. Determination of Limits on Anomalous Couplings

The absence of an excess of events with high  $p_T(W)$  excluded large deviations of the trilinear couplings from the SM values. The  $p_T$  spectrum expected at each element in a 225 point grid in  $\lambda$  and  $\Delta\kappa$  space, centered around and including the SM values, was obtained using Monte Carlo simulation. The assumptions on the  $\Lambda$  scale and on the relation between the  $WW\gamma$  and  $WWZ$  couplings affected the  $p_T$  spectra. Unequal width bins were used in order to evenly distribute the events, particularly at the ends of the spectrum. An analytic form of the prediction of the number of events in each  $p_T$  bin was obtained with a quadratic function of the coupling parameters, similar to that used in the dilepton analysis, fit to the number of events for each pair of anomalous couplings. The difference between the estimated number of events and the fit was calculated for each pair of anomalous couplings for a particular  $p_T$  bin and found to be less than 10%. This value was included as a systematic uncertainty in the fitting procedure. To set limits on the anomalous couplings, a binned likelihood fit was performed on the  $p_T(W)$  spectrum of the expected signal plus background for  $p_T(W) > 25$  GeV/c. In each  $p_T$  bin, the probability was calculated for the predicted number of events to fluctuate to the observed number of events. The uncertainties in the efficiency, background estimates, and total luminosity were convoluted in the likelihood function using Gaussian distributions. This likelihood fit procedure is described in detail in Appendix 2.

Limits were obtained on the coupling parameters under four sets of assumptions on the relations among the coupling parameters. For all four assumptions, the most likely point in the  $\lambda - \Delta\kappa$  grid was the SM point. For the assumption  $\Delta\kappa \equiv \Delta\kappa_\gamma = \Delta\kappa_Z$ , and  $\lambda \equiv \lambda_\gamma = \lambda_Z$  with  $\Lambda = 1500$  GeV, the contours for the 95% CL limit on  $\lambda$  and  $\Delta\kappa$ , with  $\Lambda = 1500$  GeV, are shown in Fig. 30(a). The 95% CL limits were  $-0.9 \leq \Delta\kappa \leq 1.1$  ( $\lambda = 0$ ) and  $-0.6 \leq \lambda \leq 0.7$  ( $\Delta\kappa = 0$ ). As in the  $WW \rightarrow$  dileptons analysis, the limits on  $\lambda$  and  $\Delta\kappa$  exhibited almost no correlation. Under the HISZ relations [39], which parameterize the  $WWZ$  couplings in terms of the  $WW\gamma$  couplings:  $\Delta\kappa_Z = 0.5 \Delta\kappa_\gamma (1 - \tan^2 \theta_w)$ ,  $\Delta g_Z = 0.5 \Delta\kappa_\gamma / \cos^2 \theta_w$ ,  $\lambda_Z = \lambda_\gamma$ , the 95% CL coupling limit contours with

$\Lambda = 1500$  GeV are shown in Fig. 30(b). The limits were  $-1.0 \leq \Delta\kappa_\gamma \leq 1.3$  ( $\lambda_\gamma = 0$ ) and  $-0.6 \leq \lambda_\gamma \leq 0.7$  ( $\Delta\kappa_\gamma = 0$ ). Under the assumption that the  $WW\gamma$  couplings have the SM value, the 95% CL upper limit contour, in  $\lambda_Z$  and  $\Delta\kappa_Z$ , is shown in Fig. 30(c). The 95% CL limits were  $-1.1 \leq \Delta\kappa_Z \leq 1.3$  ( $\lambda_Z = 0$ ) and  $-0.7 \leq \lambda_Z \leq 0.7$  ( $\Delta\kappa_Z = 0$ ). Under the assumption that the  $WWZ$  couplings have the SM value, the 95% CL upper limit contour, in  $\lambda_\gamma$  and  $\Delta\kappa_\gamma$ , is shown in Fig. 30(d). Here the  $\Lambda$  scale was 1000 GeV. The 95% CL limits were  $-2.8 \leq \Delta\kappa_\gamma \leq 3.3$  ( $\lambda_\gamma = 0$ ) and  $-2.5 \leq \lambda_\gamma \leq 2.6$  ( $\Delta\kappa_\gamma = 0$ ). The limits from  $S$ -matrix unitarity are also shown in Fig. 30(a)–(d) for each assumption. The unitarity limits were ellipses for (a) and (b) due to the form of Equation 11.1, shown in Appendix 1. However, for (c) and (d), the intersections of the  $W\gamma$  and  $WW/WZ$  unitarity contours are shown in the Figure.

Because this analysis accounted for the background in fitting the spectrum for  $p_T(W) > 25$  GeV/c, it was sensitive to anomalous couplings at both large and small  $\hat{s}$ . All of the results of the fits were insensitive to the  $p_T(W)$  threshold when varied between 25 and 130 GeV/c. In contrast, the analysis in Ref. [17], which required  $p_T(W) > 130$  GeV/c, loses sensitivity at small  $\hat{s}$ ; deviations from the SM restricted to  $\hat{s} < 500$  GeV could have been missed [40].

## VIII. COMBINED $W\gamma$ AND $WW/WZ$ ANOMALOUS COUPLING RESULTS

The  $WW \rightarrow$  dileptons counting experiment and  $WW/WZ$   $p_T$  spectrum analysis are sensitive to the same  $WW\gamma$  couplings as the  $W\gamma$  photon spectrum analysis. The three analyses can be combined to form tighter limits on anomalous couplings. In this section, the procedure and results of the combined fit are discussed.

The likelihood method used in the  $WW/WZ$   $p_T$  analysis and  $W\gamma$  photon spectrum analysis was used in the combined analysis. The joint log-likelihood was the sum of the log of the probabilities, as discussed in Appendix 2. The likelihood was formed from the Monte Carlo  $WW/WZ$   $p_T$  spectrum and Monte Carlo  $W\gamma$  photon spectrum, expected background, and observed number of events in each channel with identical binning as was used in the separate analyses. The expected number of  $WW \rightarrow$  dilepton events was recalculated for  $\Lambda = 1500$  GeV (equivalent to use of a single bin for all  $p_T(W)$ ); while the  $\lambda$  and  $\Delta\kappa$  limits would have violated unitarity for this value of  $\Lambda$ , the combined limit does not. Common systematic uncertainties, including lepton identification efficiency (4% for all channels with an electron in the final state and 12% for all channels with a muon in the final state), integrated luminosity (5.4%), and choice of parton distribution function (9.1%), were treated as discussed in Appendix 2. The limits are insensitive to a change in the size of the common systematic uncertainty by as much as a factor of two. The statistical uncertainties of the data dominate the uncertainty in the analysis.

The following results were obtained. For the assumption that the  $WW\gamma$  couplings are equal to the  $WWZ$  couplings and with  $\Lambda = 1500$  GeV, the 95% CL limits were  $-0.71 \leq \Delta\kappa \leq 0.89$  ( $\lambda = 0$ ) and  $-0.44 \leq \lambda \leq 0.44$  ( $\Delta\kappa = 0$ ). Figure 31 shows the 95% CL limit contour for  $\lambda$  and  $\Delta\kappa$  along with the unitarity contour.

## IX. $Z\gamma$ PRODUCTION

A measurement of the  $ZZ\gamma$  and  $Z\gamma\gamma$  couplings using  $p\bar{p} \rightarrow \ell\ell\gamma + X$  ( $\ell = e, \mu, \nu$ ) events is discussed in this section.

The signature for  $Z\gamma$  events was two high- $p_T$  leptons ( $e^+e^-$ ,  $\mu^+\mu^-$  or  $\nu\bar{\nu}$ ), and a photon. The leptons would not necessarily have combined to give the  $Z$  boson mass. In initial state radiation and anomalous coupling events, of the type shown in Figs. 1(a)–(c), the dilepton invariant mass for the electron and muon decay channels would be at the  $Z$  boson mass. However, for events with bremsstrahlung radiation from a charged lepton, as shown in Fig. 6, the two leptons would have a pair mass below that of the  $Z$  boson. Furthermore, photons radiated from the leptons would have tended to be close to the leptons. The neutrino decay channels had several important differences. Besides having a higher branching fraction than the electron and muon decay channels (20.0% for three generations of neutrinos vs. 3.37% for  $ee$  or  $\mu\mu$ ), the  $Z \rightarrow \nu\nu$  decays are inferred with high efficiency in the detector through the  $E_T$  measurement. The radiative diagrams do not contribute to the neutrino decay channel. Thus, the cross-section changes more quickly with anomalous couplings than the cross section for the electron and muon channels. The signature for these events was a photon recoiling against the  $E_T$  of the undetected neutrinos. The main disadvantage of the neutrino channel was that the backgrounds were larger than in the other channels.

### A. The $ee$ channel

The  $ee\gamma$  sample was selected from events which satisfied the ELE-2-MAX trigger described in Table I. The data set corresponded to an integrated luminosity of  $14.3 \pm 0.8$  pb $^{-1}$ . From this sample, candidate events were required

to have two electrons in the fiducial region with  $E_T > 17$  GeV. At least one electron had to satisfy the “Tight II” requirements (see Table III) while the other satisfied the “Loose I” requirements. This combination of tight and loose electron selection was possible because the backgrounds from fake electrons were small, relative to the expected signal, when the photon was required to pass the “Loose” requirements (see Table IV) within the fiducial region. After trigger, fiducial region, and particle selection criteria were applied, 10 events with two electrons with  $E_T > 17$  GeV and a photon with  $E_T > 5$  GeV survived. Final selected events were required to have  $E_T^e > 25$  GeV and a photon separated from each electron by  $\Delta\mathcal{R}_{e\gamma} > 0.7$  with  $E_T^\gamma > 10$  GeV. These last two requirements reduced the contribution of radiative events. Four events survived in the final sample. Table XIX indicates the number of events surviving the last few selection criteria. For details on the characteristics of individual events and for event displays see Ref. [41].

Selection Criteria	No. of Surviving Events
Starting Sample	77
Fiducial and Particle ID	15
Trigger Criteria	10
$E_T^{ele} > 25$ GeV	10
$\Delta\mathcal{R}_{e\gamma} > 0.7$	8
$E_T^\gamma > 10$ GeV	4

TABLE XIX. Number of  $ee\gamma$  candidates which passed the selection criteria.

The trigger efficiency for SM  $Z\gamma$  production was estimated using the  $Z \rightarrow ee$  event sample. It was found to be  $0.98 \pm 0.01$ . The acceptance for SM  $Z\gamma$  production and for production via anomalous  $ZZ\gamma$  and  $Z\gamma\gamma$  couplings was estimated using the event generator of Ref. [18] combined with the fast detector simulation discussed in Section III. MRSD-’ structure functions [27] were used in the event generation and the cross section was scaled by a k-factor of 1.34. The geometric acceptance for SM production was 53%. Averaged over  $E_T$  for SM production, the photon identification efficiency was also  $0.53 \pm 0.05$ . With the particle identification criteria, the kinematic, and the fiducial requirements on the electrons and photons described above, the selection efficiency for SM  $Z\gamma$  production was  $0.17 \pm 0.02$  and the expected cross section times efficiency was  $0.20 \pm 0.02$  pb.

The background included contributions from  $Z + \text{jet(s)}$  production where one of the jets mimicked an electron or photon, multijet production where more than one jet was misidentified as a photon or electron, and  $\tau\tau\gamma$  production followed by decay of each  $\tau$  to  $e\bar{\nu}_e\nu_\tau$ .

Processes where jets mimicked photons, jets mimicked electrons, and double and triple fakes contributed to the QCD background. The background and its  $E_T$ -dependence were estimated by counting the number of  $ee + \text{jet(s)}$  and  $e\gamma + \text{jet(s)}$  events, with the electrons and photons passing the signal cuts and with jet transverse energy above 10 GeV and 25 GeV, respectively. The probabilities for jets to mimic EM objects were determined with a procedure similar to that described in Section V C and observed to be approximately  $E_T$  independent (see Fig. 17). Table XX contains the probabilities for a jet to mimic photons and electrons in the CC and EC, and the final probabilities with the direct photon contribution removed. Multiplying these probabilities by the number of jets in these samples led to a background of  $0.43 \pm 0.06$  QCD events.

Type of Fake	CC	EC	Avg. after direct $\gamma$ correction
Jet $\rightarrow \gamma$	$(0.84 \pm 0.08) \times 10^{-3}$	$(0.90 \pm 0.11) \times 10^{-3}$	$(0.65 \pm 0.18) \times 10^{-3}$
Jet $\rightarrow e_{\text{TightII}}$	$(0.62 \pm 0.07) \times 10^{-3}$	$(1.5 \pm 0.2) \times 10^{-3}$	$(0.84 \pm 0.10) \times 10^{-3}$
Jet $\rightarrow e_{\text{LooseI}}$	$(1.7 \pm 0.1) \times 10^{-3}$	$(1.6 \pm 0.2) \times 10^{-3}$	$(1.5 \pm 0.2) \times 10^{-3}$

TABLE XX. Probability for a jet to mimic a photon or electron, averaged over  $E_T$ , for the  $Z\gamma \rightarrow ee\gamma$  and  $Z\gamma \rightarrow \mu\mu\gamma$  electron and photon selection criteria.

The  $E_T$  spectra of the jets allowed the background to be calculated as a function of  $E_T$ . This is shown in Fig. 32(a).  $Z$  boson events where an electron was misreconstructed as a photon and a jet was misreconstructed as the lost electron contributed to a bump in the fake photon at  $E_T \sim 50$  GeV. Thus, the shape of the fake photon sample was parameterized with an exponential function plus a Gaussian. The fit is also shown in Fig. 32 (a).

The  $\tau\tau\gamma$  background was estimated with a sample of ISAJET events passed through the DØGEANT detector simulation and the offline reconstruction algorithm. The total  $\tau\tau\gamma$  background increased with increasing anomalous couplings because more  $Z\gamma \rightarrow \tau\tau\gamma$  events would have been produced along with the  $Z \rightarrow ee\gamma$  events. After normalization with the production cross section and  $\tau$  branching fractions, the expected fraction of the cascading tau

decays in the final  $Z\gamma$  sample was  $f_e = (0.10 \pm 0.05\%)$ , where the uncertainty came from the expected difference in acceptance from using  $Z \rightarrow \tau\bar{\tau} \rightarrow ee\nu\bar{\nu}\nu\bar{\nu}$  Monte Carlo to simulate a background which included photons which radiated from a charged lepton, as well as the uncertainty in cross section and branching ratios. For the SM couplings the  $\tau\bar{\tau}\gamma$  background was negligible.

To summarize, four  $Z\gamma \rightarrow ee\gamma$  candidates were observed. The total background expected was  $0.43 \pm 0.06$  events. This corresponds to an observed signal of  $3.57_{-1.91}^{+3.15} \pm 0.06$  events, where the first uncertainty is statistical and the second is the uncertainty in the background. The observed signal agrees with the SM prediction of  $2.8 \pm 0.3 \pm 0.2$  events, where the first uncertainty reflects systematics of the Monte Carlo model and the second is the uncertainty in the luminosity.

## B. The $\mu\mu$ channel

The  $\mu\mu\gamma$  sample was selected from events which satisfied the MU\_ELE trigger described in Table I. This data set corresponded to an integrated luminosity of  $13.7 \pm 0.7\text{pb}^{-1}$ . At least two muons and one photon were required in the event. One muon was required to satisfy the “Tight III” requirements and the other to satisfy the “Loose II” requirements of Table II. It was required that  $p_T^{\mu_1} > 15 \text{ GeV}/c$  and  $p_T^{\mu_2} > 8 \text{ GeV}/c$ , where  $\mu_1$  and  $\mu_2$  are the higher and lower  $p_T$  muons respectively. The photon, satisfying the “Loose” requirements, was required to have  $E_T > 10 \text{ GeV}$  and to be separated from both muons by  $\Delta\mathcal{R}_{\mu\gamma} > 0.7$ , as in the electron channel. Two candidates for  $Z\gamma \rightarrow \mu\mu\gamma$  passed these selection criteria. Details on the characteristics of the candidates and event displays are in Ref. [41]. Table XXI indicates the number of events which survived the last few selection criteria, after the particle identification and kinematic selection were applied.

Selection Criteria	No. of Surviving Events
Particle ID and Kinematic Selection	4
Trigger Criteria	3
$\Delta\mathcal{R}_{\mu\gamma} > 0.7$	2

TABLE XXI. Number of  $\mu\mu\gamma$  candidates which passed the selection criteria.

The efficiencies were calculated as a function of  $ZZ\gamma$  and  $Z\gamma\gamma$  couplings with the event generator of Ref. [18] combined with the parameterized detector simulation. MRSD-’ structure functions [27] were used in the event generation and the cross section was scaled by a k-factor of 1.34. The level 1 muon trigger efficiency (with two chances to trigger on each event), the photon trigger efficiency curve shown in Fig. 33, and the efficiencies for particle identification criteria as discussed in Section II, were included. The detector acceptance was 20% for SM  $Z\gamma \rightarrow \mu\mu\gamma$  production. The overall efficiency for SM production, for events satisfying the kinematic criteria, was  $0.06 \pm 0.01$ . The cross section times efficiency for SM production was  $0.17 \pm 0.03 \text{ pb}$ . The efficiency increased with anomalous couplings because the muons became more central, increasing their acceptance.

The background consisted of  $\mu\mu + \text{jet(s)}$  events, where the jet was misidentified as a photon, and  $Z \rightarrow \tau\tau$  cascade decays including a final state photon. The backgrounds where a jet mimicked a photon included Drell-Yan production with associated jets,  $Z + \text{jets}$  production and cosmic ray muons (already small because of the tight muon identification criteria) in coincidence with jet events. The contribution to the QCD background from  $b\bar{b}$  production was expected to be negligible due to the muon isolation requirements and the muon  $p_T$  threshold. The QCD background was estimated from a data sample containing a pair of muons satisfying the same muon identification criteria as the signal sample. This sample contained all of the  $\mu\mu + \text{jet}$  backgrounds in the same proportions as the signal sample. The procedure was to count the number of jets of  $E_T > 10 \text{ GeV}$ , in events which pass the selection criteria, and multiply that number by the probability for a jet to mimic a photon from Table XX. Because different triggers were used in collecting the signal and background samples, a scaling factor  $1.3 \pm 0.3$  was necessary to account for differences in the trigger efficiency and integrated luminosities. Fifteen jets passed the selection criteria; eight jets were in the CC and seven in the EC. The result was  $N_{QCD}^\mu = 0.02 \pm 0.01$  expected background events. The  $p_T$  spectrum of the jets in the background sample is shown in Fig. 32(b). The fit made to the  $E_T$  spectrum of the electron channel fakes was used to parameterize the  $E_T$  spectrum of the fakes in the muon channel, with the appropriate normalization, because of the much higher statistics of the former.

The  $\tau\tau\gamma$  background was estimated using the same procedure as was used for the electron channel. The expected fraction of the cascade  $\tau$  decays in the final  $Z\gamma \rightarrow \mu\mu\gamma$  sample was  $1.4 \pm 0.5\%$ . For SM couplings, the  $\tau\tau\gamma$  background

was  $0.03 \pm 0.01$  events.

To summarize, two  $Z\gamma \rightarrow \mu\mu\gamma$  candidates were observed. The total background expected was  $0.05 \pm 0.01$  events. This corresponds to an observed signal of  $1.95_{-1.29}^{+2.62} \pm 0.01$  events, where the first uncertainty is statistical and the second is the uncertainty on the background. The observed signal agrees with the SM prediction of  $2.3 \pm 0.4 \pm 0.1$  events, where the first uncertainty reflects systematics of the Monte Carlo model and the second is the uncertainty in the luminosity. The photon  $E_T$  spectrum for the combined  $ee$  and  $\mu\mu$  data, expected signal and expected background are shown in Fig. 34.

### C. The $\nu\bar{\nu}$ channel

The  $Z + \gamma \rightarrow \nu\bar{\nu}\gamma$  signature was a single photon which recoiled against the  $\cancel{E}_T$  of the unmeasured neutrino pair. The nature of the backgrounds for this channel was very different from the electron and muon channels in that they were larger and included contributions from sources to which the previous channels were immune. One background resulted from unreconstructed cosmic ray and Tevatron beam related muons which deposited energy in the electromagnetic calorimeter through bremsstrahlung. A second important background, occurring at moderately high  $E_T(\gamma)$ , came from  $W \rightarrow e\nu$  where the electron was misidentified as a photon due to a missing track. These backgrounds forced the analysis to use much stronger particle identification criteria and tighter kinematic selection than the  $Z\gamma$  analyses presented above.

The candidate sample was selected from events passing the ELE-HIGH trigger of Table I. A selection on the “event quality” removed events with noisy cells in the calorimeter, second EM objects with  $E_T > 5$  GeV, or when the calorimeter was recovering due to a large pulse from Main Ring associated energy deposition. Both the photon  $E_T$  and the  $\cancel{E}_T$  were required to be greater than 40 GeV to reduce the background from  $W$  boson decays. Events with muons in the central region were rejected to reduce cosmic ray backgrounds. Events with jets of  $E_T$  greater than 15 GeV were also rejected; by limiting the  $p_T$  boost of the events, the kinematic range of  $\cancel{E}_T$  and  $E_T^e$  from the  $W$  boson background was reduced. The strictest photon requirement, “Tight”, was used to reduce the backgrounds from cosmic rays, from beam related muons, and from  $W$  boson decays. Lastly, the calorimeter was searched, in a road about the line defined by the vertex located by the EMVTX package (see Section II C 9) and the energy-weighted center of the photon shower in the CC, for energy deposition consistent with the passage of an unreconstructed cosmic ray which might have radiated the photon. This algorithm (MTC) tracked the muon energy deposition through the longitudinally and azimuthally segmented towers of the calorimeter.

Four events remained after all selection criteria were applied. The photons in the four events had  $E_T$  of 41, 41, 46, and 68 GeV. Table XXII shows the number of events remaining after each of the selection criteria.

Selection Criteria	Number of Events Remaining
Trigger, Event Quality and Kinematics	1887
$ \eta_\gamma  < 1.0$ or $1.5 <  \eta_\gamma  < 2.5$	1637
“Loose” Photon Criteria	1448
$N_\mu^{CF} = 0$	1098
No Jet with $E_T > 15$ GeV	480
“Tight” Photon Criteria	5
MTC selection	4

TABLE XXII. Event selection criteria for the  $Z\gamma \rightarrow \nu\bar{\nu}\gamma$  analysis.

The ELE-HIGH trigger was completely efficient for  $E_T(\gamma) > 40$  GeV. The efficiency for the photon identification criteria (excluding the fiducial requirements), the event quality, the muon and jet vetoes, and the MTC selection criteria were estimated using the  $Z \rightarrow ee$  candidates collected using the same trigger as the signal. The efficiency for the jet veto was cross checked with a Next-to-Leading logarithm  $Z\gamma$  Monte Carlo generator [42]. The calculated efficiency loss agreed with the measurement. Table XXIII contains a summary of these efficiencies. The efficiency for the fiducial selection came from the event generator of Ref. [18] combined with the parameterized detector simulation.

Selection Criteria	CC	Combined	EC
Event Quality		$0.981 \pm 0.002$	
Photon ID Criteria	$0.61 \pm 0.02$		$0.66 \pm 0.05$
$N_{\mu}^{CF} = 0$		$0.988 \pm 0.002$	
No Jet with $E_T > 15$ GeV		$0.84 \pm 0.02$	
MTC Selection	$0.97 \pm 0.02$		–
Total	$0.48 \pm 0.02$		$0.54 \pm 0.04$

TABLE XXIII. Efficiency, excluding photon fiducial requirements, for the  $Z\gamma \rightarrow \nu\nu\gamma$  analysis. The uncertainties indicated are statistical only.

The cosmic ray and beam halo backgrounds, due to unreconstructed muons which radiated a photon as they passed through the calorimeter, was estimated using cosmic ray and beam halo muons identified in the data.

Two samples of this kind of background event which radiated a photon into the CC were identified. The first sample was identified by applying all the selection criteria except for the HITSINFO criteria of the “Tight” photon ID requirements, the CF muon veto, and the MTC requirement. The event was required to have a reconstructed muon. The rejections for the HITSINFO and the MTC selection criteria were determined from this sample. The reconstruction efficiency for the muon background ( $\epsilon_{\text{cosmic } \mu}$ ) were estimated from a second sample of events, dominated by cosmic ray muons, which passed the same selection criteria as the former sample (excluding the requirement that the muon was reconstructed) and failed the EMVTX criteria. The inefficiency was  $1 - \epsilon_{\text{cosmic } \mu} = 0.34 \pm 0.03$ . The background to  $Z\gamma$  was then determined from the number of events in the former sample, modified by the rejection provided by the HITSINFO and MTC criteria and by the factor  $(1 - \epsilon_{\text{cosmic } \mu})/\epsilon_{\text{cosmic } \mu}$ . The resulting expected background was  $1.4 \pm 0.6$  events for CC photons.

For the muon background events with a photon in the EC, a two-sample procedure analogous to that described above for the CC was used to estimate the background due to beam-halo muons. It was measured to be  $0.38 \pm 0.23$  events, where the large fractional uncertainty is due to the low statistics of one of the tagged samples.

The muon background rejection was found to be independent of the photon  $E_T$  for both the CC and EC regions, so the background events were used to make a parameterization of the photon spectrum. The doubly-identified background muons were used for the CC. For the EC, the larger of the two available background samples was used. The result of the fit is shown in Fig. 35 together with the background data.

Another background comes from  $W \rightarrow e\nu$  events where the electron is misidentified as a photon due to tracking inefficiency. The kinematic requirements combined with the jet veto rejected some of the misidentified  $W$  boson decays, but additional rejection was required. It came from the HITSINFO criteria of the “Tight” photon selection. A procedure similar to that used to estimate the background due to muon bremsstrahlung was used in this case. A nearly pure sample of tagged  $W \rightarrow e\nu$  events with  $E_T^e$  and  $\cancel{E}_T$  both greater than 25 GeV was obtained by applying all of the event selection criteria except for the HITSINFO and MTC (CC only) criteria and by requiring an electron with a good track match significance,  $TMS \leq 10$  (see Section II C 5), instead of a photon. The rejection,  $R_H$ , due to HITSINFO came from a sample of  $W \rightarrow e\nu$  events which failed the electron tracking requirement. Including small corrections to account for the fraction of these mistracked  $W$  events, lost from this sample because of an overlapping random track, and to account for cosmic ray bremsstrahlung in this background sample,  $R_H$  was found to be  $48 \pm 12$  ( $43 \pm 14$ ) for the CC (EC). With the measured efficiency of the track finding, the track match significance and the MTC criteria ( $\epsilon_T$ ,  $\epsilon_\sigma$ , and  $\epsilon_{MTC}$ , respectively), the  $W \rightarrow e\nu$  background was simply the number of tagged  $W \rightarrow e\nu$  events times  $(1 - \epsilon_T)/(\epsilon_T \epsilon_\sigma \epsilon_{MTC} R_H)$ . This was found to be  $2.2 \pm 0.6$  ( $1.8 \pm 0.6$ ) events for the CC (EC). The  $E_T$  spectrum of the expected background is shown in Fig. 36. Parameterizations for the expected  $E_T^\gamma$  spectrum of background were derived from the  $W \rightarrow e\nu$  events. They are shown in Fig. 36.

The possible QCD backgrounds included: multijet production, where a jet was misidentified as a photon and the  $\cancel{E}_T$  results from mismeasurement of a jet or from neutrinos in a jet; direct photon production (jet + photon) where a jet contributes to  $\cancel{E}_T$ ; and  $Z + \text{jets} \rightarrow \nu\bar{\nu} + \text{jets}$  where a jet is misidentified as a photon. However, the size of the QCD backgrounds fell rapidly as the photon  $E_T$  and  $\cancel{E}_T$  thresholds were raised. The backgrounds were found to be negligible for  $E_T^\gamma$  and  $\cancel{E}_T \geq 35$  GeV.

The total background was  $3.6 \pm 0.8$  ( $2.2 \pm 0.6$ ) for the CC (EC). It is summarized in Table XXIV.

Background	$N_{bck}^{CC}$	$N_{bck}^{EC}$
Muon Bremsstrahlung	$1.4 \pm 0.6$	$0.38 \pm 0.23$
$W \rightarrow e\nu$	$2.2 \pm 0.6$	$1.8 \pm 0.6$
QCD Sources	negligible	negligible
Total	$3.6 \pm 0.8$	$2.2 \pm 0.6$

TABLE XXIV. Number of expected background events in the CC and EC for the  $Z\gamma \rightarrow \nu\bar{\nu}\gamma$  analysis.

The expected numbers of signal events for SM and for anomalous couplings were estimated using the leading order event generator of Ref. [18] combined with the parameterized detector simulation, including a  $p_T(Z)$  spectrum from the  $Z$  boson data to mimic the effects of the jet veto on the acceptance. The energy scale for the underlying event was determined by comparing the  $p_T$  as determined from the electrons and hadronic recoil in low  $p_T$   $Z \rightarrow ee$  events. As in the charged lepton analyses, the cross section was scaled by a  $k$ -factor of 1.34 and the MRSD-’ structure functions [27] were used in the event generation. A 12% uncertainty in the cross section resulted primarily from the choice of parton distribution functions, modeling of the jet veto, modeling of the detector, and the detector efficiency. Table XXV presents a summary of the expected signal and background as well as the number of events seen with photons in the CC and EC. The SM signal was expected to be  $1.8 \pm 0.2$  events with a  $5.8 \pm 1.0$  event background. For comparison, the expected number of signal events for anomalous couplings was approximately a factor of 9 higher for  $h_{30}^Z = 3$ ,  $h_{40}^Z = 1$ . Four candidates were observed, consistent with the SM expectations. The photon spectra expected for the signal and background, as well as that seen in the data are shown in Fig. 37.

Region	$N_{SM}$	$N_{bck}$	Data
CC ( $ \eta_\gamma  \leq 1.1$ )	$1.4 \pm 0.2$	$3.6 \pm 0.8$	3
EC ( $1.5 \leq  \eta_\gamma  \leq 2.5$ )	$0.39 \pm 0.05$	$2.2 \pm 0.6$	1
Total	$1.8 \pm 0.2$	$5.8 \pm 1.0$	4

TABLE XXV. Number of expected  $\nu\bar{\nu}\gamma$  events assuming SM couplings, number of expected background events, and observed signal.

#### D. Limits on Anomalous $ZZ\gamma$ and $Z\gamma\gamma$ Couplings

To set limits on the anomalous coupling parameters, the observed  $E_T$  spectrum of the photons in the three channels was fit with the MC predictions plus the estimated background (summarized in Table XXVI). The binned likelihood method described in Appendix 2 was used. To exploit the prediction that anomalous couplings lead to an excess of events with high  $E_T$  photons, a high  $E_T$  bin with no events was used in the fit. Common systematic uncertainties, including photon identification efficiency, integrated luminosity, choice of parton distribution functions, and choice of  $p_T(Z)$  distribution were treated as discussed in Appendix 2.

Channel	$ee$	$\mu\mu$	$\nu\bar{\nu}$
$N^{SM}$	$2.8 \pm 0.3 \pm 0.2$	$2.3 \pm 0.4 \pm 0.1$	$1.8 \pm 0.2$
$N^{BG}$	$0.43 \pm 0.06$	$0.05 \pm 0.01$	$5.8 \pm 1.0$
$N^{observed}$	4	2	4

TABLE XXVI. Summary the of  $Z\gamma \rightarrow$  dileptons analyses including the number of SM events expected, expected backgrounds, and number of candidates observed.

The form-factor scale dependence of the result was studied. The chosen value of  $\Lambda = 500$  GeV was close to the sensitivity limit of the experiment for  $h_{20}$  and  $h_{40}$  for the  $ee + \mu\mu$  channels; for larger values of  $\Lambda$  partial wave unitarity was violated for certain values of the coupling parameters allowed at 95% CL. With the  $\nu\bar{\nu}$  and combined analysis,  $\Lambda$  could be extended to 750 GeV without violating unitarity. In that case, tighter limits on anomalous couplings could be obtained.

Figures 38 to 40 show the coupling limits for the  $CP$ -conserving  $ZZ\gamma$  parameters. The shapes of the  $Z\gamma\gamma$

limit contours were similar. Figure 38 shows the results of the fit for the  $ee$  and  $\mu\mu$  channels at 68% and 95% CL. Figure 39 shows the results of the fit for the  $\nu\bar{\nu}$  channels and for the three channels combined at 95% CL. The form factor scale  $\Lambda = 500$  GeV was used in these two figures. Figure 40 shows the 95% CL limits for  $\Lambda = 750$  GeV. The 95% confidence level limits on CP-conserving couplings are given in Table XXVII. Shown are the limits for the  $ee + \mu\mu$  channels, the  $\nu\bar{\nu}$  channel, and the limits from the three analyses combined. Limits on the CP-violating couplings were numerically identical to the corresponding CP-conserving couplings with the single exception that  $-0.86 < h_{10}^Z < 0.87$  (to be compared with  $-0.87 < h_{30}^Z < 0.87$ ) for the  $\nu\bar{\nu}\gamma$  analysis.

$ee + \mu\mu$	$\nu\bar{\nu}$	Combined Limits
Limits with $\Lambda = 500$ GeV		
$-1.8 < h_{30}^Z < 1.8$	$-0.87 < h_{30}^Z < 0.87$	$-0.78 < h_{30}^Z < 0.78$
$-1.9 < h_{30}^\gamma < 1.9$	$-0.90 < h_{30}^\gamma < 0.90$	$-0.81 < h_{30}^\gamma < 0.81$
$-0.5 < h_{40}^Z < 0.5$	$-0.21 < h_{40}^Z < 0.21$	$-0.19 < h_{40}^Z < 0.19$
$-0.5 < h_{40}^\gamma < 0.5$	$-0.22 < h_{40}^\gamma < 0.22$	$-0.20 < h_{40}^\gamma < 0.20$
Limits with $\Lambda = 750$ GeV		
-	$-0.49 < h_{30}^Z < 0.49$	$-0.44 < h_{30}^Z < 0.44$
-	$-0.50 < h_{30}^\gamma < 0.50$	$-0.45 < h_{30}^\gamma < 0.45$
-	$-0.07 < h_{40}^Z < 0.07$	$-0.06 < h_{40}^Z < 0.06$
-	$-0.07 < h_{40}^\gamma < 0.07$	$-0.06 < h_{40}^\gamma < 0.06$

TABLE XXVII. Limits on CP-conserving  $ZZ\gamma$  and  $Z\gamma\gamma$  anomalous coupling parameters for the  $ee + \mu\mu$ ,  $\nu\bar{\nu}$  and combined  $Z\gamma$  analyses. These axes limits are at 95% confidence level with  $\Lambda = 500$  and 750 GeV.

## X. CONCLUSIONS

Four gauge boson pair production processes and corresponding trilinear gauge boson coupling parameters were studied using the data from 1.8 TeV  $\bar{p}p$  collisions collected with the DØ detector during 1992-1993 Tevatron collider run at Fermilab. The data sample corresponded to an integrated luminosity of approximately 14 pb<sup>-1</sup>.

Searches were made for deviations from the SM. This would have been manifest as an enhancement in the production cross section and  $E_T$  spectrum of the bosons. In the analyses of the  $W\gamma$  final states, the photon  $E_T$  spectrum was compared with the expectations of the SM and used to produce limits on anomalous  $WW\gamma$  couplings. A limit on the cross section for  $WW \rightarrow$  dilepton led to a limit on anomalous  $WW\gamma$  and  $WWZ$  couplings. In the  $WW/WZ \rightarrow e\nu$  jet jet analysis, the  $E_T$  spectrum of the  $W$  and  $Z$  bosons was used to produce limits on anomalous  $WW\gamma$  and  $WWZ$  couplings. The  $W\gamma$ ,  $WW$  and  $WW/WZ$  analyses were combined to produce limits on  $WW\gamma$  and  $WWZ$  couplings. Finally, in the analysis of  $Z\gamma$  final states, the photon  $E_T$  spectrum was compared to the expectations of the SM and used to produce limits on anomalous  $ZZ\gamma$  and  $Z\gamma\gamma$  couplings. No deviations from the SM were observed.

The  $W\gamma$  analysis yielded 23 candidate events where the  $W$  boson was identified by its leptonic decay products, a high  $p_T$  electron (11 events) or muon (12 events), and a neutrino inferred by large  $\cancel{E}_T$  in the event. The expected backgrounds for the electron and muon channels were  $2.0 \pm 0.9$  and  $4.4 \pm 1.1$  events, respectively. Using the acceptance for the SM  $W\gamma$  production events, the  $W\gamma$  cross section (for photons with  $E_T^\gamma > 10$  GeV and  $\Delta\mathcal{R}_{\ell\gamma} > 0.7$ ) was calculated from the combined  $e + \mu$  sample to be  $\sigma(W\gamma) = 138_{-38}^{+51}(\text{stat}) \pm 21(\text{syst})$  pb. A binned maximum likelihood fit was performed on the  $E_T^\gamma$  spectrum for each of the  $W(e\nu)\gamma$  and  $W(\mu\nu)\gamma$  samples to set limits on the anomalous coupling parameters. The limits on the CP-conserving anomalous coupling parameters at the 95% CL were  $-1.6 < \Delta\kappa_\gamma < 1.8$  ( $\lambda_\gamma = 0$ ),  $-0.6 < \lambda_\gamma < 0.6$  ( $\Delta\kappa_\gamma = 0$ ) using a form factor scale of  $\Lambda = 1.5$  TeV. The  $U(1)_{EM}$ -only couplings of the  $W$  boson to a photon, which lead to  $\kappa_\gamma = 0$  and  $\lambda_\gamma = 0$ , and thereby  $\mu_W = e/2m_W$  and  $Q_W^e = 0$ , was excluded at the 80% CL, while zero magnetic moment ( $\mu_W = 0$ ) was excluded at the 95% CL.

The search for  $WW$  events where both of the  $W$  bosons decay leptonically to  $e\nu$  or  $\mu\nu$  yielded one candidate event with an expected background of  $0.56 \pm 0.13$  events. The upper limit on the cross section for SM  $W$  boson pair production was estimated to be 87 pb at the 95% CL. The limit on the cross section was translated into limits on the anomalous coupling parameters. The limits on the CP-conserving anomalous coupling parameters were  $-2.6 < \Delta\kappa < 2.8$  ( $\lambda = 0$ ) and  $-2.1 < \lambda < 2.1$  ( $\Delta\kappa = 0$ ) at the 95% CL, using a form factor scale of  $\Lambda = 900$  GeV, where  $\Delta\kappa \equiv \Delta\kappa_\gamma = \Delta\kappa_Z$  and  $\lambda \equiv \lambda_\gamma = \lambda_Z$  were assumed.



The analysis of the  $WW$  and  $WZ$  production events in the electron + jets channels, where one  $W$  boson decayed into  $e\nu$  and the second  $W$  boson or  $Z$  boson decayed into two jets, yielded 84 candidate events with an expected background of  $75.8 \pm 13.3$  events, while the SM predicted  $3.2 \pm 0.6$  signal events. A maximum likelihood fit was performed on the  $p_T$  spectrum of the  $W$  boson, computed from the  $E_T$  of electron and the  $\cancel{E}_T$ , to set limits on the anomalous couplings. The limits on the CP-conserving anomalous coupling parameters were  $-0.9 < \Delta\kappa < 1.1$  ( $\lambda = 0$ ) and  $-0.6 < \lambda < 0.7$  ( $\Delta\kappa = 0$ ) at the 95% CL, using a form factor scale of  $\Lambda = 1.5$  TeV, where  $\Delta\kappa \equiv \Delta\kappa_\gamma = \Delta\kappa_Z$  and  $\lambda \equiv \lambda_\gamma = \lambda_Z$  were assumed.

The  $W\gamma$  production process is sensitive only to the  $WW\gamma$  coupling parameters.  $WZ$  production is sensitive only to the  $WWZ$  couplings. On the other hand,  $W$  pair production is sensitive both to the  $WW\gamma$  and the  $WWZ$  coupling parameters. Using assumptions on the relationship between the  $WW\gamma$  and  $WWZ$  coupling parameters, these three analyses were combined to set the tightest limits on the coupling parameters. A maximum likelihood fit was performed on the three sets of data simultaneously using a common form factor scale of  $\Lambda = 1.5$  TeV and the assumption that  $\Delta\kappa \equiv \Delta\kappa_\gamma = \Delta\kappa_Z$  and  $\lambda \equiv \lambda_\gamma = \lambda_Z$ . The limits obtained at the 95% CL were  $-0.71 < \Delta\kappa < 0.89$  ( $\lambda = 0$ ) and  $-0.44 < \lambda < 0.44$  ( $\Delta\kappa = 0$ ). These are the tightest limits on  $WW\gamma$  and  $WWZ$  couplings presently available.

$Z\gamma$  final states in  $\bar{p}p$  collisions are produced from the  $Z$  boson-quark and photon-quark couplings in the SM. The  $ZZ\gamma$  and  $Z\gamma\gamma$  couplings, which can produce  $Z\gamma$  final states, are absent in the SM. The  $Z\gamma$  analysis yielded a total of 10 candidate events; 4 events with  $Z \rightarrow ee$ , 2 events with  $Z \rightarrow \mu\mu$  and 4 events with  $Z \rightarrow \nu\nu$ . The expected backgrounds for the  $ee$  and  $\mu\mu$  channels were  $0.43 \pm 0.06$  events and  $0.05 \pm 0.01$  events, respectively. The expected background for the  $\nu\nu$  channel was  $5.8 \pm 1.0$  events. The sum of the SM prediction and the expected background was  $2.8 \pm 0.3 \pm 0.2$  ( $2.3 \pm 0.4 \pm 0.1$ ) events for the electron (muon) decay modes and  $7.6 \pm 1.0$  events for the neutrino decay mode. A maximum likelihood fit was performed on the  $p_T$  spectrum of the photons to set limits on the anomalous coupling parameters. The 95% CL axes limits on the CP-conserving coupling parameters are  $-0.78 < h_{30}^Z < 0.78$  ( $h_{40}^Z = 0$ );  $-0.19 < h_{40}^Z < 0.19$  ( $h_{30}^Z = 0$ ),  $-0.81 < h_{30}^\gamma < 0.81$  ( $h_{40}^\gamma = 0$ );  $-0.20 < h_{40}^\gamma < 0.20$  ( $h_{30}^\gamma = 0$ ), using a form factor scale of  $\Lambda = 500$  GeV and  $-0.44 < h_{30}^Z < 0.44$  ( $h_{40}^Z = 0$ );  $-0.06 < h_{40}^Z < 0.06$  ( $h_{30}^Z = 0$ ),  $-0.45 < h_{30}^\gamma < 0.45$  ( $h_{40}^\gamma = 0$ );  $-0.06 < h_{40}^\gamma < 0.06$  ( $h_{30}^\gamma = 0$ ), using a form factor scale of  $\Lambda = 750$  GeV. The limits obtained in this measurement are the most stringent limits on anomalous  $ZV\gamma$  couplings currently available.

All of these limits on the anomalous coupling parameters will be significantly improved when the analyses of the data taken during the 1994-1995 Tevatron collider run, which corresponded to approximately  $80 \text{ pb}^{-1}$ , are completed.

We thank U. Baur, J. Ohnemus, and D. Zeppenfeld for providing us with Monte Carlo generators and much helpful advice. We thank the staffs at Fermilab and collaborating institutions for their contributions to this work, and acknowledge support from the Department of Energy and National Science Foundation (U.S.A.), Commissariat à l'Énergie Atomique (France), State Committee for Science and Technology and Ministry for Atomic Energy (Russia), CNPq (Brazil), Departments of Atomic Energy and Science and Education (India), Colciencias (Colombia), CONACyT (Mexico), Ministry of Education and KOSEF (Korea), CONICET and UBACyT (Argentina), and the A.P. Sloan Foundation.

## XI. APPENDIX 1: TRILINEAR GAUGE BOSON COUPLING PARAMETERS

### A. $WW\gamma$ and $WWZ$ coupling parameters

The tree-level Feynman diagrams for  $q\bar{q} \rightarrow W\gamma$ ,  $q\bar{q} \rightarrow WW$  and  $q\bar{q} \rightarrow WZ$  production processes are shown in Figs. 1, 2 and 6. A formalism has been developed to describe the  $WW\gamma$  and  $WWZ$  vertices for the most general gauge boson self-interactions [7,15]. The Lorentz invariant effective Lagrangian for the gauge boson self-interactions contains fourteen dimensionless coupling parameters, seven each for  $WW\gamma$  and  $WWZ$ :

$$\begin{aligned} \mathcal{L}_{WWV}/g_{WWV} = & ig_1^V (W_{\mu\nu}^\dagger W^\mu V^\nu - W_\mu^\dagger V_\nu W^{\mu\nu}) \\ & + i\kappa_V W_\mu^\dagger W_\nu V^{\mu\nu} + i \frac{\lambda_V}{M_W^2} W_{\lambda\mu}^\dagger W_\nu^\mu V^{\nu\lambda} \\ & - g_4^V W_\mu^\dagger W_\nu (\partial^\mu V^\nu + \partial^\nu V^\mu) \\ & + g_5^V \epsilon^{\mu\nu\rho\alpha} \left( W_\mu^\dagger \overset{\leftrightarrow}{\partial}_\rho W_\nu \right) V_\sigma \\ & + i\tilde{\kappa}_V W_\mu^\dagger W_\nu \tilde{V}^{\mu\nu} + \frac{i\tilde{\lambda}_V}{M_W^2} W_{\lambda\mu}^\dagger W_\nu^\mu \tilde{V}^{\nu\lambda}, \end{aligned}$$

where  $W^\mu$  denotes the  $W^-$  field,  $W_{\mu\nu} = \partial_\mu W_\nu - \partial_\nu W_\mu$ ,  $V_{\mu\nu} = \partial_\mu V_\nu - \partial_\nu V_\mu$ ,  $\tilde{V}_{\mu\nu} = \frac{1}{2}\epsilon_{\mu\nu\rho\alpha}V^{\rho\alpha}$ , and  $(A \overset{\leftrightarrow}{\partial}_\mu B) = A(\partial_\mu B) - (\partial_\mu A)B$ ,  $V = \gamma, Z$  and  $M_W$  is the mass of the  $W$  boson. The overall couplings  $g_{WWV}$  are  $g_{WW\gamma} = -e$  and  $g_{WWZ} = -e(\cot\theta_w)$  as in the SM, where  $e$  and  $\theta_w$  are the positron charge and the weak mixing angle. The couplings  $\lambda_V$  and  $\kappa_V$  conserve  $C$  and  $P$ . The couplings  $g_4^V$  are odd under  $CP$  and  $C$ ,  $g_5^V$  are odd under  $C$  and  $P$ , and  $\tilde{\kappa}_V$  and  $\tilde{\lambda}_V$  are odd under  $CP$  and  $P$ .

In the SM, all the couplings are zero with the exception of  $g_1^V$  and  $\kappa_V$  ( $g_1^\gamma = g_1^Z = \kappa_\gamma = \kappa_Z = 1$ ). Electromagnetic gauge invariance restricts  $g_1^\gamma, g_4^\gamma$  and  $g_5^\gamma$  to the SM values of 1, 0, and 0. The  $SU(2)_L \times U(1)_Y$  gauge invariance requires  $\lambda = \lambda_\gamma = \lambda_Z$  and  $\tilde{\lambda} = \tilde{\lambda}_\gamma = \tilde{\lambda}_Z$ . If the photon and  $Z$  boson couplings are assumed to be equal, then  $g_1^Z = g_1^\gamma = 1$  and  $g_4^Z = g_4^\gamma = g_5^Z = g_5^\gamma = 0$ .

With the non-SM coupling parameters, the amplitudes for the gauge boson pair production grow with energy, eventually violating tree-level unitarity. Using dipole form factors for anomalous couplings,

$$\Delta\kappa(s) = \frac{\Delta\kappa}{(1 + \hat{s}/\Lambda^2)^2}$$

with a form factor scale,  $\Lambda$ , the unitarity is restored. The scale,  $\Lambda$ , is constrained by

$$\Lambda \leq \left[ \frac{6.88}{(\kappa - 1)^2 + 2\lambda^2 + 2\tilde{\lambda}^2} \right]^{1/4} \text{TeV}, \quad (11.1)$$

if the photon and  $Z$  boson couplings are assumed to be equal.

The  $CP$ -conserving  $WW\gamma$  coupling parameters are related [8] to the magnetic dipole moment ( $\mu_W$ ) and electric quadrupole moment ( $Q_W^e$ ) of the  $W$  boson:

$$\mu_{W+} = \frac{e}{2M_W}(1 + \kappa_\gamma + \lambda_\gamma)$$

$$Q_{W+}^e = -\frac{e}{M_W^2}(\kappa_\gamma - \lambda_\gamma).$$

The  $CP$ -violating  $WW\gamma$  coupling parameters are related to the electric dipole moment ( $d_W$ ) and magnetic quadrupole moment ( $Q_W^m$ ) of the  $W$  boson:

$$d_{W+} = \frac{e}{2M_W}(\tilde{\kappa}_\gamma + \tilde{\lambda}_\gamma)$$

$$Q_{W+}^m = -\frac{e}{m_W^2}(\tilde{\kappa}_\gamma - \tilde{\lambda}_\gamma).$$

The  $CP$ -violating  $WW\gamma$  couplings  $\tilde{\lambda}_\gamma$  and  $\tilde{\kappa}_\gamma$  are tightly constrained by measurements of the neutron electric dipole moment to  $|\tilde{\kappa}_\gamma|, |\tilde{\lambda}_\gamma| < 10^{-3}$  [43].

## B. $ZZ\gamma$ and $Z\gamma\gamma$ Couplings

Theoretical calculations of the tree-level cross section for  $Z\gamma$  production for SM and anomalous couplings have been performed [18]. Assuming only electromagnetic gauge invariance and Lorentz invariance, the vertex function for the  $ZZ\gamma$  and  $Z\gamma\gamma$  interaction can be described with the following form:

$$\begin{aligned} \Gamma_{\alpha\beta\mu}^{Z\gamma V} = & C_V(h_1^V(q_2^\mu g^{\alpha\beta} - q_2^{\mu\beta}) \\ & + \frac{h_2^V}{m_Z^2}P^\alpha((P \cdot q_2)g^{\mu\beta} - q_2^\mu P^\beta) \\ & + h_3^V\epsilon^{\mu\alpha\beta\rho}q_{2\rho} + \frac{h_4^V}{m_Z^2}P^\alpha\epsilon^{\mu\beta\rho\sigma}P_\rho q_{2\sigma}), \end{aligned}$$

where  $V$  indicates a photon or  $Z$  boson,  $C_Z$  is  $(P^2 - q_1^2)/M_Z^2$  and  $C_\gamma$  is  $P^2/M_Z^2$ ,  $q_1$  and  $q_2$  are the momenta of the outgoing particles and  $P$  is the momentum of the virtual boson. An overall normalization factor of  $g_{ZZ\gamma} = g_{Z\gamma\gamma} = e$ ,

left out in the equation, is used. These couplings are  $C$  odd dimensionless functions of  $q_1^2$ ,  $q_2^2$ , and  $P^2$ ; i.e.  $\hat{s}$ . In addition,  $h_1^V$  and  $h_2^V$  are  $P$  even, and thus violate  $CP$ . The other pair,  $h_3^V$  and  $h_4^V$ , are  $CP$  conserving.

In order to avoid violating  $S$ -matrix unitarity, the couplings should asymptotically approach zero (their SM value) at high energies [14,44]. Therefore, the  $ZV\gamma$  couplings have to be energy-dependent and are thus modified with form factors  $h_i^V(q_1^2, q_2^2, P^2)$  which vanish at high  $q_1^2$ ,  $q_2^2$ , or  $P^2$ . However, since  $q_1^2 \approx m_Z^2$ ,  $q_2^2 \approx 0$  and  $P^2 = \hat{s}$ , only the high  $\hat{s}$  behavior should be included in the form factor for the  $q\bar{q} \rightarrow Z\gamma$  diagrams. The convention [18] is to use a generalized dipole form factor such that:

$$h_i^V(m_Z^2, 0, \hat{s}) = \frac{h_{i0}^V}{(1 + \hat{s}/\Lambda^2)^n}.$$

The constraints on the  $h_{i0}^V$  can be derived from partial wave unitarity of the general  $f\bar{f} \rightarrow Z\gamma$  process [31], [45]. Assuming only one coupling is non-zero at a time, the following unitarity limits can be derived for  $\Lambda \gg m_Z$  [18], [46]:

$$|h_{10}^{Z/\gamma}|, |h_{30}^{Z/\gamma}| < \frac{(\frac{2}{3}n)^n}{(\frac{2}{3}n - 1)^{n-3/2}} \frac{0.126/0.151 \text{TeV}^3}{\Lambda^3}$$

$$|h_{20}^{Z/\gamma}|, |h_{40}^{Z/\gamma}| < \frac{(\frac{2}{5}n)^n}{(\frac{2}{5}n - 1)^{n-5/2}} \frac{2.1/2.5 \cdot 10^{-3} \text{TeV}^5}{\Lambda^5}.$$

From the above equations, unitarity is satisfied for  $n > 3/2$  for  $h_{1,3}^V$ , and  $n > 5/2$  for  $h_{2,4}^V$ . In this paper  $n = 3$  for  $h_{1,3}^V$ , and  $n = 4$  for  $h_{2,4}^V$  are used. This choice ensures the same asymptotic energy behavior for the  $h_{1,3}^V$  and  $h_{2,4}^V$  couplings. The dependence of results on the choice of  $n$  is discussed in [18].

The anomalous couplings  $h_i^V$  are related to the  $Z\gamma$  transition dipole and quadrupole moments. The  $CP$ -even combinations of  $h_3^V$  and  $h_4^V$  correspond to the electric dipole and magnetic quadrupole transition moments; the  $CP$ -odd combinations of  $h_1^V$  and  $h_2^V$  correspond to magnetic dipole and electric quadrupole transition moments. The relations between the couplings and moments depends on both the center of mass energy  $\sqrt{\hat{s}}$  and on the momentum of the final state photon [47]. They are:

$$\begin{aligned} d_{Z_T} &= -\frac{e}{\sqrt{2}} \frac{k^2}{M_Z^3} (h_{30}^Z - h_{40}^Z), \\ Q_{Z_T}^e &= \frac{e}{M_Z^2} \sqrt{10} (2h_{10}^Z), \\ \mu_{Z_T} &= -\frac{e}{\sqrt{2}} \frac{k^2}{M_Z^3} (h_{10}^Z - h_{20}^Z), \\ Q_{Z_T}^m &= \frac{e}{M_Z^2} \sqrt{10} (2h_{30}^Z), \end{aligned}$$

where  $d_{Z_T}$  ( $\mu_{Z_T}$ ) is the transition electric (magnetic) dipole moment,  $Q_{Z_T}^e$  ( $Q_{Z_T}^m$ ) is the transition electric (magnetic) quadrupole moment, and  $k$  is the photon energy.

## XII. APPENDIX 2: BINNED LIKELIHOOD FIT

A binned likelihood fit was applied to the  $p_T$  spectra of  $\gamma$  and  $W$  to set limits on the anomalous coupling parameters. The observed numbers of events ( $N_i$ ) in a particular  $p_T$  bin can be described in terms of the numbers of expected signal events ( $n_i$ ) and background events ( $b_i$ ) using a Poisson distribution function:

$$P_i = \frac{(n_i + b_i)^{N_i}}{N_i!} e^{-(n_i + b_i)},$$

where  $n_i$  and in some cases  $b_i$  are functions of the anomalous coupling parameters.

The uncertainties in the  $n_i$  and  $b_i$  were incorporated by convoluting with Gaussian distributions:

$$P'_i = \int_{-\infty}^{\infty} \int_{-\infty}^{\infty} \left( \frac{(f_n n_i + f_b b_i)^{N_i}}{N_i!} e^{-(f_n n_i + f_b b_i)} \right) \frac{1}{2\pi\sigma_n\sigma_b} e^{-\frac{(f_n-1)^2}{2\sigma_n^2}} e^{-\frac{(f_b-1)^2}{2\sigma_b^2}} df_n df_b,$$

where  $f_n$  and  $f_b$  are multiplicative factors to  $n_i$  and  $b_i$  with mean values of 1.0;  $\sigma_n$  and  $\sigma_b$  are the fractional uncertainties of  $n_i$  and  $b_i$ . These uncertainties include the uncertainties in the integrated luminosity and the theoretical prediction of the signal and background cross sections. To exploit the prediction that anomalous couplings lead to an excess of events with high  $E_T$  photons or jets (depending on the analysis), a bin with no events at high  $E_T$  was used in the fit. The bin boundary was selected sufficiently above the highest observed transverse momentum event in the data sample that the detector resolution could not move the last data point across the boundary. For more detail, see [41]. The joint probability of all  $p_T$  bins is then

$$P = \prod_{i=1}^{N_{max}} P'_i,$$

where  $N_{max}$  is the number of  $p_T$  bins. The log likelihood function of this joint probability is defined as

$$\mathcal{L} = -\ln(P).$$

The limits on the coupling parameters were obtained by maximizing this quantity. The 95% confidence level limit on the parameters of the log-likelihood function (the coupling parameters for the case here) is the contour where the log-likelihood is 1.92 lower than the maximum.

---

\* Visitor from IHEP, Beijing, China.

† Visitor from Universidad San Francisco de Quito, Quito, Ecuador.

- [1] H. Aihara *et al.*, Summary of the Working Subgroup on Anomalous Gauge Boson Interactions of the DPF Long-Range Planning Study, published in *Electroweak Symmetry Breaking and Beyond the Standard Model*, eds. T. Barklow, S. Dawson, H. Haber and J. Siegrist (World Scientific). Fermilab Preprint Pub-95/031, (1995).
- [2] DØ Collaboration, S. Abachi *et al.*, Phys. Rev. Lett. **75**, 1034 (1995).
- [3] DØ Collaboration, S. Abachi *et al.*, Phys. Rev. Lett. **75**, 1023 (1995).
- [4] DØ Collaboration, S. Abachi *et al.*, Phys. Rev. Lett. **77**, 3303 (1996).
- [5] DØ Collaboration, S. Abachi *et al.*, Phys. Rev. Lett. **75**, 1028 (1995).
- [6] DØ Collaboration, S. Abachi *et al.*, Fermilab-Pub-97/047-E, submitted to Phys. Rev. Lett., (1997).
- [7] K. Hagiwara, R. D. Peccei, D. Zeppenfeld, and K. Hikasa, Nucl. Phys. **B282**, 253 (1987).
- [8] K. Kim and Y.-S. Tsai, Phys. Rev. D **7**, 3710 (1973).
- [9] R. W. Brown and K. O. Mikaelian, Phys. Rev. D **19**, 922 (1979); R. W. Brown, K. O. Mikaelian and D. Sahdev, Phys. Rev. D **20**, 1164 (1979).
- [10] U. Baur and D. Zeppenfeld, Nucl. Phys. **B308**, 127 (1988).
- [11] UA2 Collaboration, J. Alitti *et al.*, Phys. Lett. B **277**, 194 (1992).
- [12] CDF Collaboration, F. Abe *et al.*, Phys. Rev. Lett. **74**, 1936 (1995).
- [13] J. Ohnemus, Phys. Rev. D **44**, 1403 (1991).
- [14] C. H. Llewellyn Smith, Phys. Lett. B **46** 233 (1973); J. M. Cornwall, D. N. Levin and G. Tiktopoulos, Phys. Rev. Lett. **30**, 1268 (1973).
- [15] K. Hagiwara, J. Woodside, and D. Zeppenfeld, Phys. Rev. D **41**, 2113 (1990).
- [16] J. Ohnemus, Phys. Rev. D **44**, 3477 (1991).
- [17] CDF Collaboration, F. Abe *et al.*, Phys. Rev. Lett. **75**, 1017 (1995).
- [18] U. Baur and E. L. Berger, Phys. Rev. D **47**, 4889, (1993).
- [19] CDF Collaboration, F. Abe *et al.*, Phys. Rev. Lett. **74**, 1941 (1995).
- [20] DØ Collaboration, S. Abachi *et al.*, Nucl. Instrum. Methods **A338**, 185 (1994).
- [21] DØ Collaboration, S. Abachi *et al.*, Nucl. Instrum. Methods **A324**, 53 (1993); H. Aihara *et al.*, Nucl. Instrum. Methods **A325**, 393 (1993).

- [22] F. Carminati *et al.*, “GEANT Users Guide V3.14,” CERN Program Library, December 1991 (unpublished).
- [23] T. Sjöstrand, “PYTHIA 5.6 and Jetset 7.3 Physics and Manual,” CERN-TH.6488/92, 1992, (unpublished).
- [24] F. Paige and S. Protopopescu, BNL Report BNL38034, 1986 (unpublished), release V6.49.
- [25] R. Raja, “Proceedings of the Workshop on Detector Simulation for the SSC”, Argonne, IL (1987).
- [26] J. Bantly *et al.* Report No. FERMILAB-TM-1930, 1995 (unpublished).
- [27] A.D. Martin, R.G. Roberts and W.J. Stirling, Phys. Rev. D **47**, 867 (1993).
- [28] DØ Collaboration, S. Fahey, “Proceedings of the American Physical Society Division of Particles and Fields Meeting,” Albuquerque (1994), ed. S. Seidel.
- [29] Particle Data Group, R. M. Barnett *et al.*, Review of Particle Properties, Phys. Rev. D **54**, 1, 1996.
- [30] T.D. Lee, Phys. Rev. **140**, 967 (1965).
- [31] U. Baur and D. Zeppenfeld, Phys. Lett. B **201**, 383, (1988).
- [32] Particle Data Group, L. Montanet *et al.*, Phys. Rev. D **50**, 1173 (1994). The weighted average of the  $W \rightarrow e\nu$  and  $W \rightarrow \mu\nu$  branching fraction data is used in the  $WW \rightarrow$  dileptons analysis.
- [33] E. Laenen, J. Smith, and W. L. van Neerven, Phys. Lett. B **321**, 254 (1994). For the  $t\bar{t}$  background, the central value estimate of the cross section was used.
- [34] P. B. Arnold and R. P. Kauffman, Nucl. Phys. **B349**, 381 (1991).
- [35] DØ Collaboration, S. Abachi *et al.*, Phys. Rev. Lett. **72**, 2138 (1994) and S. Abachi *et al.*, Phys. Rev. D **52**, 4877 (1995). The kinematic properties of this  $t\bar{t}$  candidate are discussed in detail here.
- [36] H. Johari, Ph. D. thesis, Northeastern University, 1995 (unpublished).
- [37] CDF Collaboration, F. Abe *et al.*, Phys. Rev. Lett. **70**, 4042 (1993).
- [38] W. Giele, E. Glover and D. Kosower, Nucl. Phys. **B 403**, 633, (1993)
- [39] K. Hagiwara *et al.*, Phys. Rev. D **48**, 2182, (1993)
- [40] C. Wendt, in the proceedings of the International Symposium on Vector Boson Self-Interactions, Los Angeles, CA, eds. U. Baur, S. Errede, and T. Muller, (February 1996) p. 285.
- [41] G. L. Landsberg, Ph. D. thesis, State University of New York at Stony Brook, 1994, (unpublished).
- [42] J. Ohnemus, Phys. Rev. D **51**, 1068 (1995).
- [43] F. Boudjema, K. Hagiwara, C. Hamzaoui and K. Numata, Phys. Rev. D **43**, 2223 (1991).
- [44] J. M. Cornwall, D. N. Levin, G. Tiktopoulos, Phys. Rev. D **10**, 1145, (1974); S. D. Joglekar, Amm. of Phys. **83**, 427, (1974).
- [45] K. Hagiwara and D. Zeppenfeld, Nucl. Phys. **B274**, 1, (1986).
- [46] H. Czyz, K. Kolodziej, and M. Zralek, Z. Phys. **C43**, 97, (1989).
- [47] F. Boudjema, private communication.

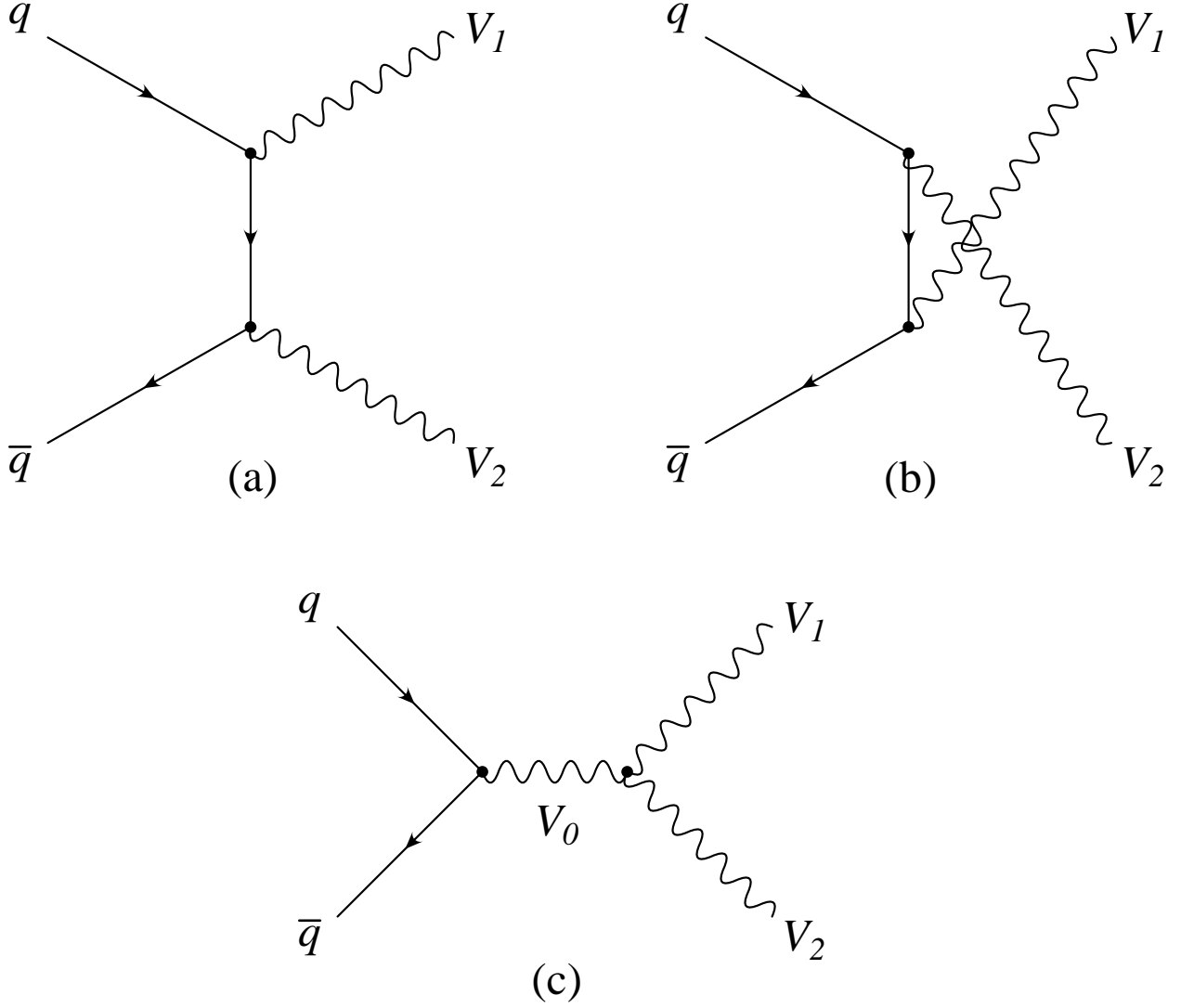


FIG. 1. Leading-order Feynman diagrams for vector boson pair production. The assignment of  $V_0$ ,  $V_1$ , and  $V_2$  depends on the final state:  $W\gamma$ ,  $WW$ ,  $WZ$  or  $Z\gamma$ .

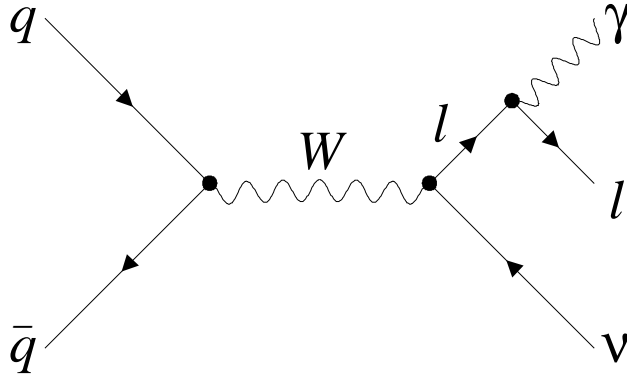


FIG. 2. The leading-order radiative Feynman diagram for  $W\gamma$  production where the photon is the result of bremsstrahlung from a final state lepton.

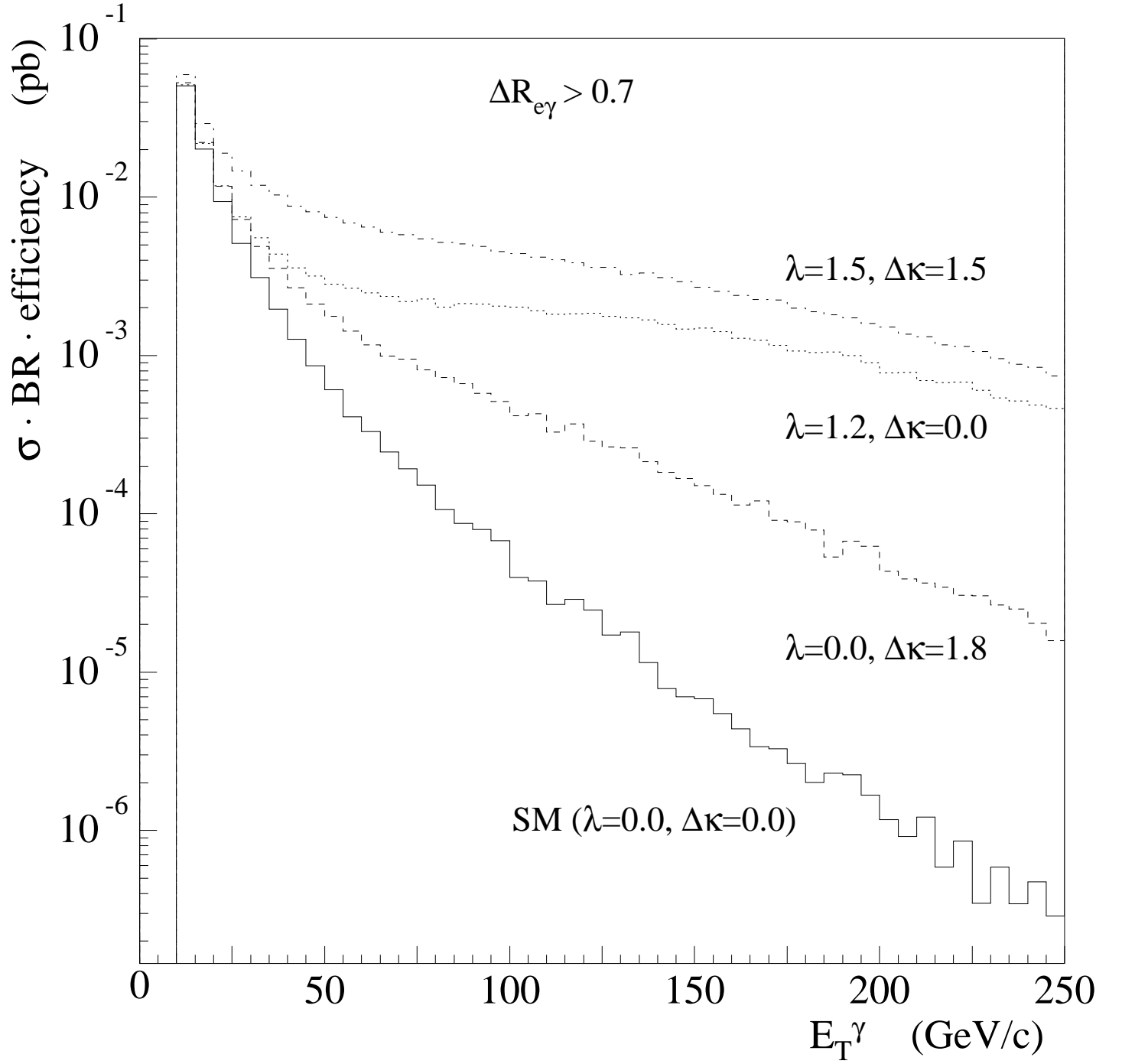


FIG. 3. The predicted  $E_T$  spectrum of photons in the  $W\gamma$  production for SM and anomalous  $WW\gamma$  couplings. Radiative diagrams are included. The requirement that  $\Delta R_{e\gamma} > 0.7$  has been made; otherwise the cross section diverges at low  $E_T^\gamma$ .



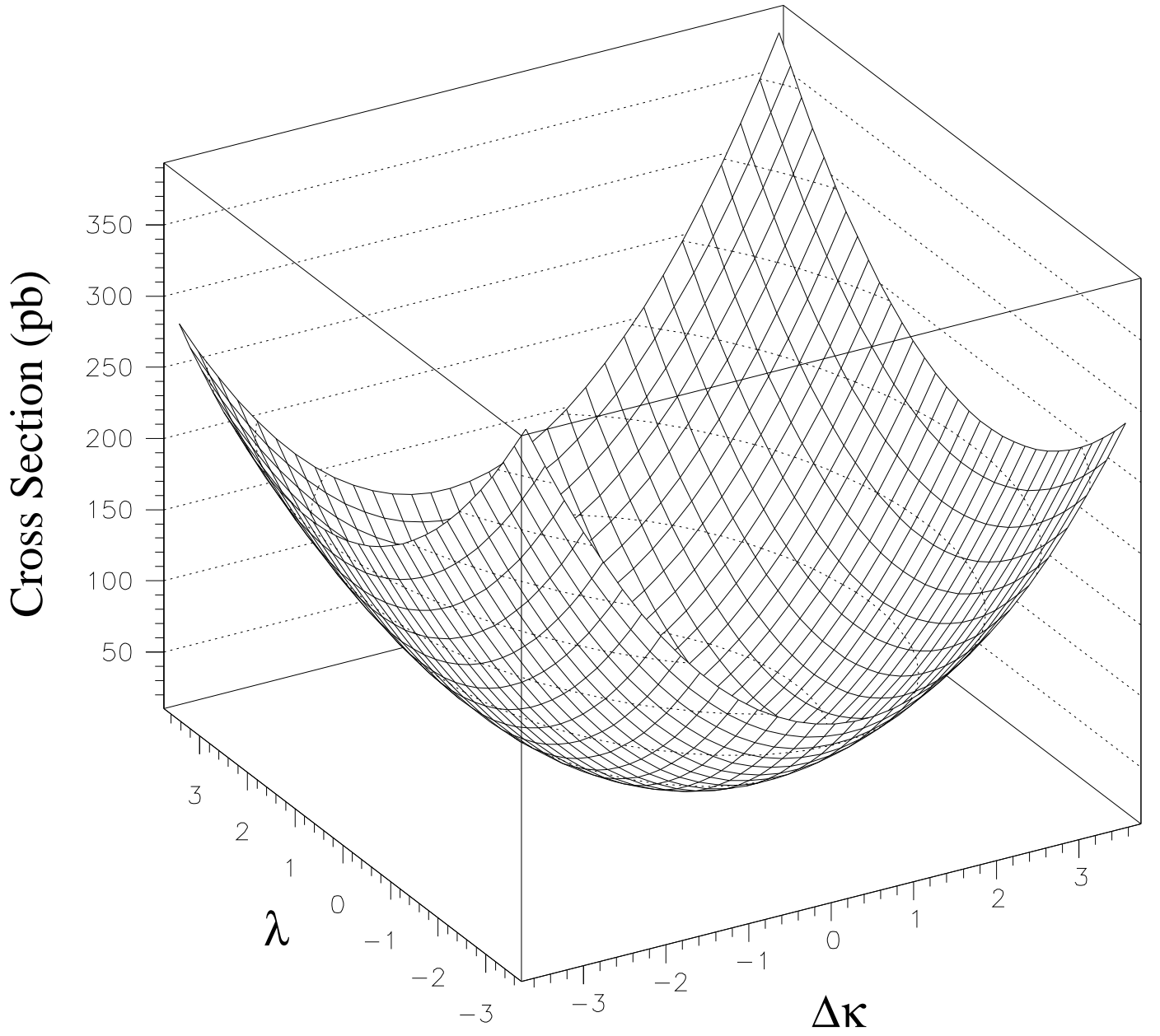


FIG. 4. The predicted cross section for  $WW$  production as a function of anomalous coupling parameters  $\lambda$  and  $\Delta\kappa$ , assuming the  $WWZ$  and  $WW\gamma$  couplings are equal, with  $\Lambda = 1000$  GeV.

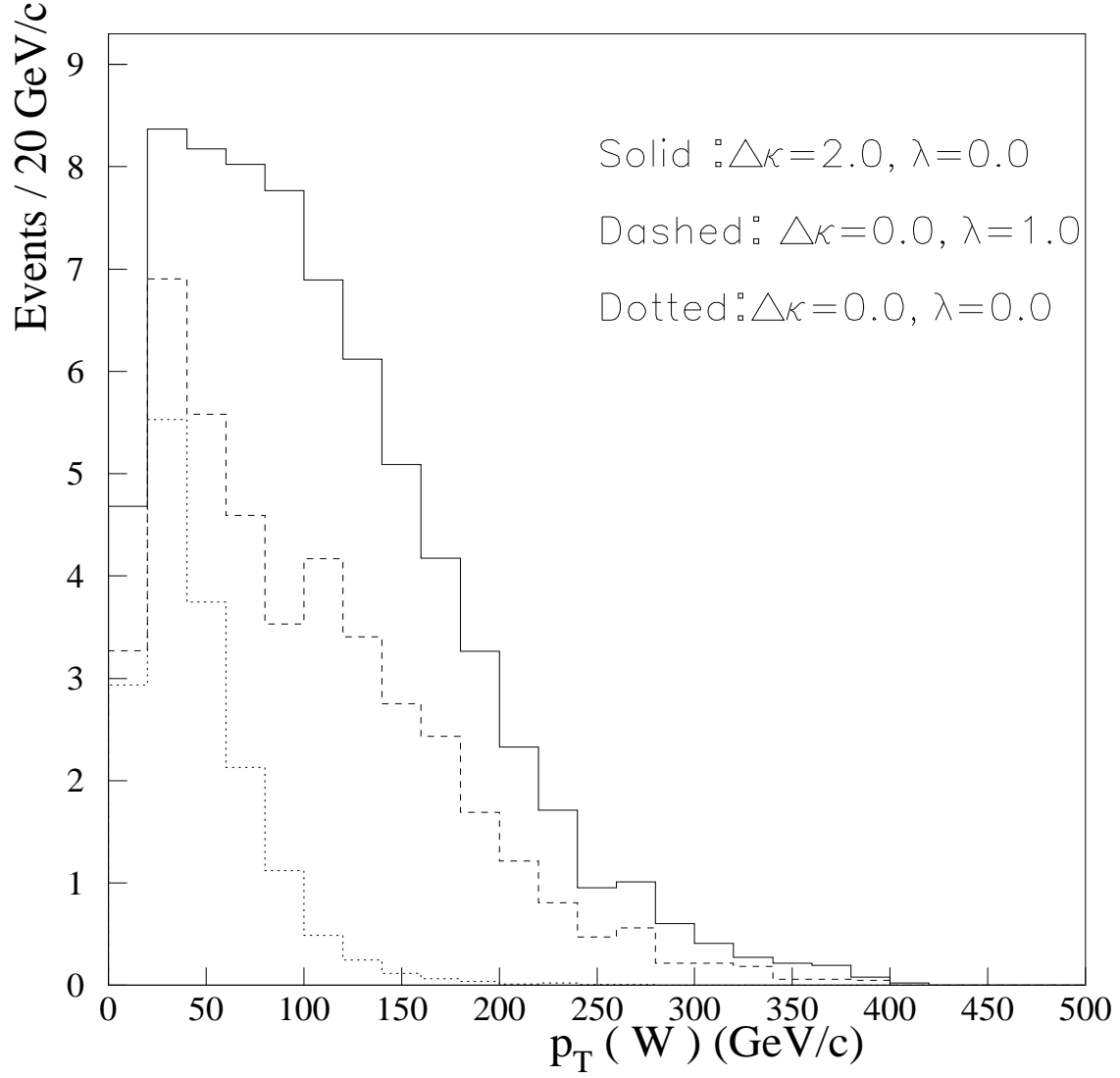


FIG. 5. The  $p_T$  spectrum of  $W$  bosons in  $WW/WZ$  production corresponding to approximately  $10 \text{ pb}^{-1}$  of collisions. The theoretical assumptions for the anomalous coupling spectra are that  $\lambda_\gamma = \lambda_Z$  and  $\Delta\kappa_\gamma = \Delta\kappa_Z$ , with  $\Lambda = 1000 \text{ GeV}$ .

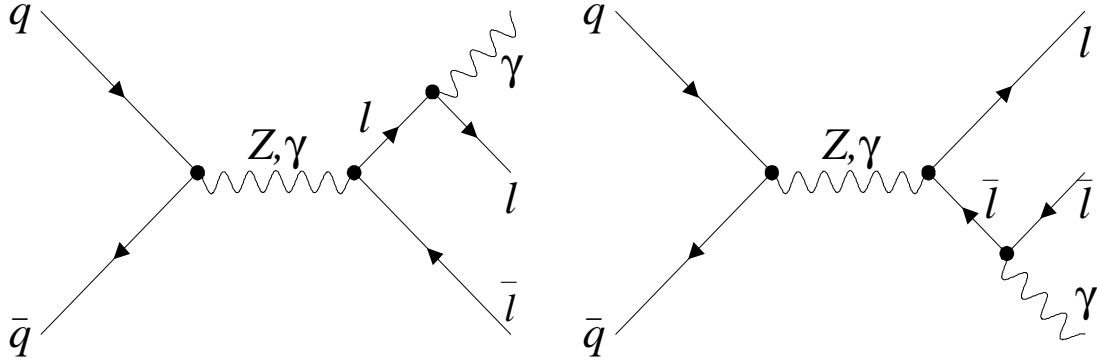


FIG. 6. The leading-order radiative Feynman diagrams for  $Z\gamma$  production where the photon is the result of bremsstrahlung from a final state lepton. This decay mode only applies to final states involving charged leptons.

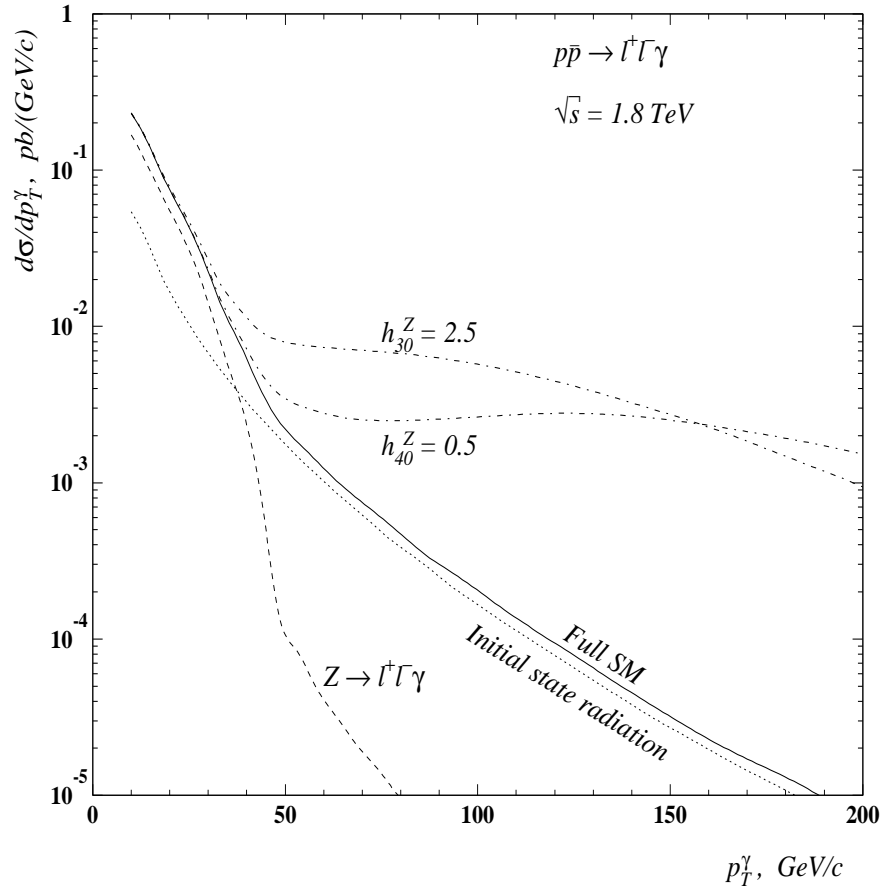


FIG. 7. The  $p_T^\gamma$  spectrum,  $d\sigma/dp_T^\gamma$ , for SM  $Z\gamma$  events from final state radiation (dashed line), initial state radiation (dotted line), the combination of initial state and final state radiation (solid line) as well as for two anomalous  $ZZ\gamma$  couplings.

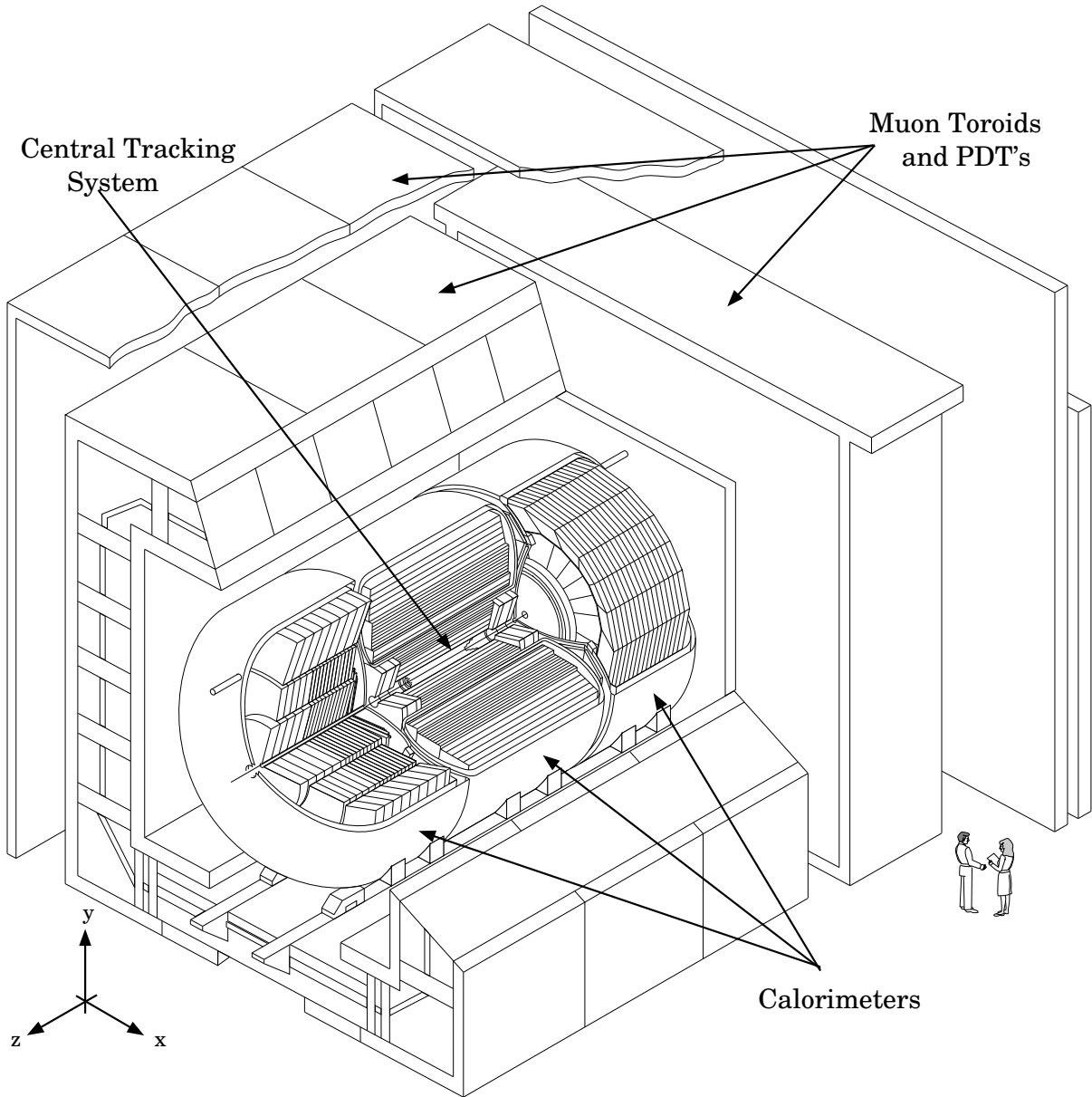


FIG. 8. Perspective view of the DØ detector. Also shown are the movable support platform, the Tevatron beampipe centered within the detector and the Main Ring beampipe which penetrates the muon system and calorimeter above the detector center.

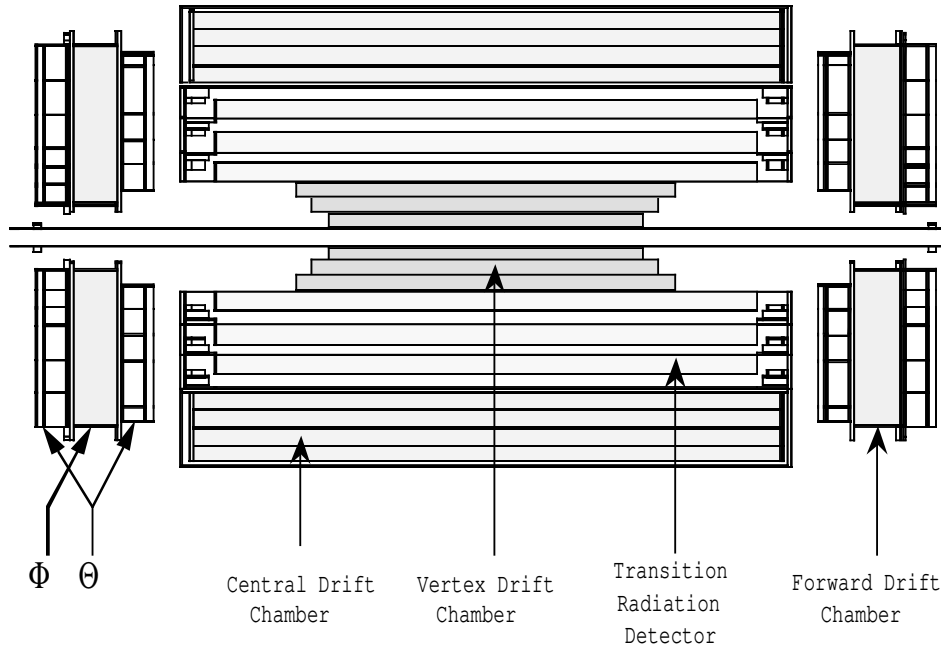


FIG. 9. The DØ central tracking detector system.

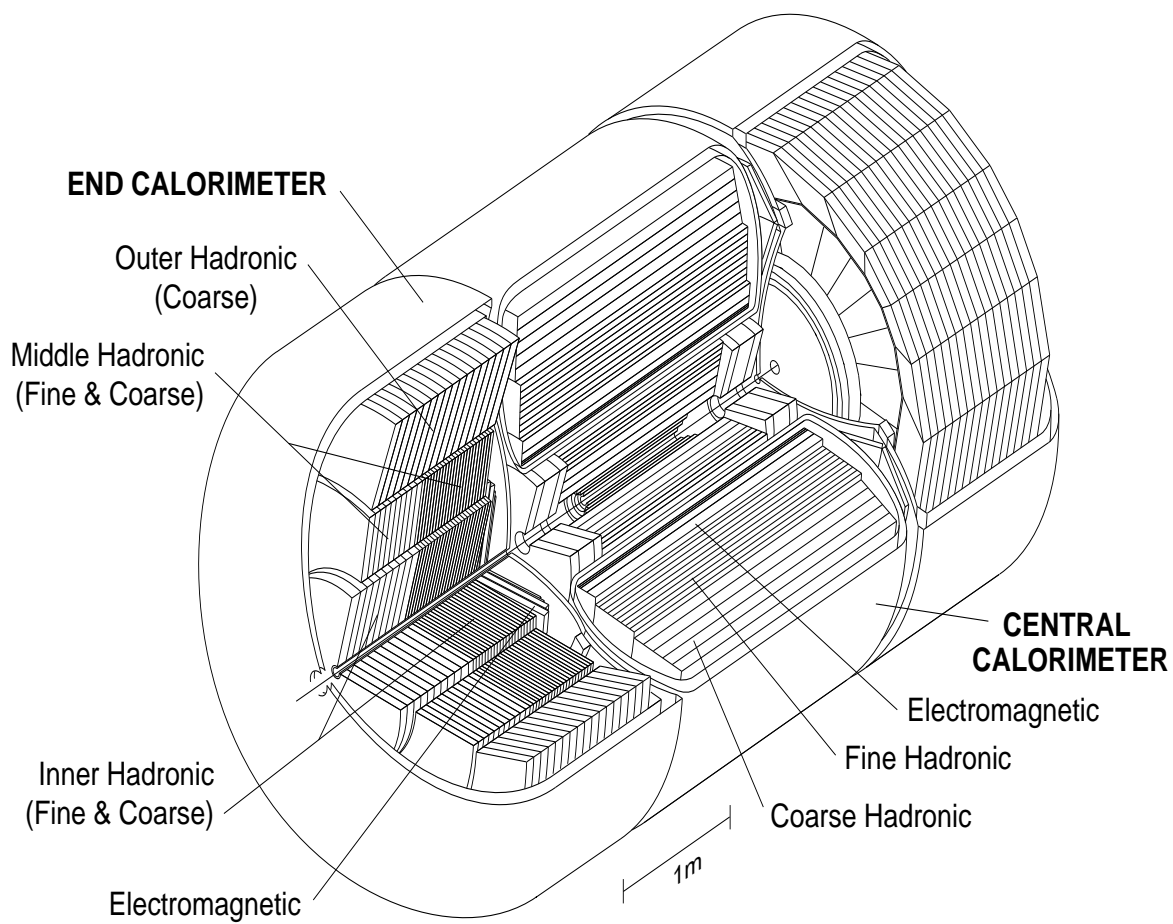


FIG. 10. The DØ calorimeters.

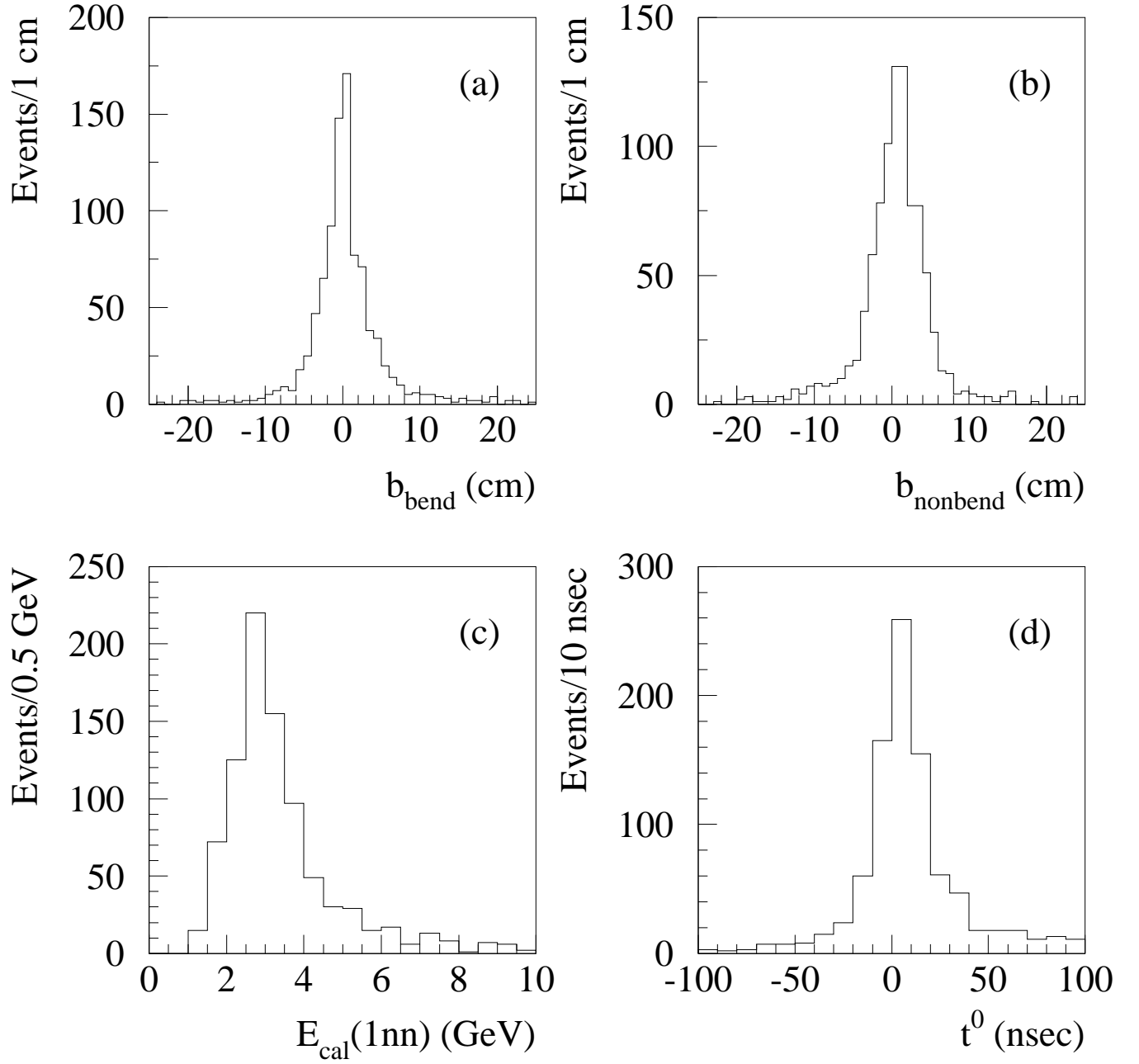


FIG. 11. Muon selection variables including (a) the bend view impact parameter, (b) the nonbend view impact parameter, (c) the energy in the calorimeter tower plus the nearest neighboring towers around the muon, and (d) the  $t_0$  resulting from the track fit with the muon time-of-origin as a parameter.



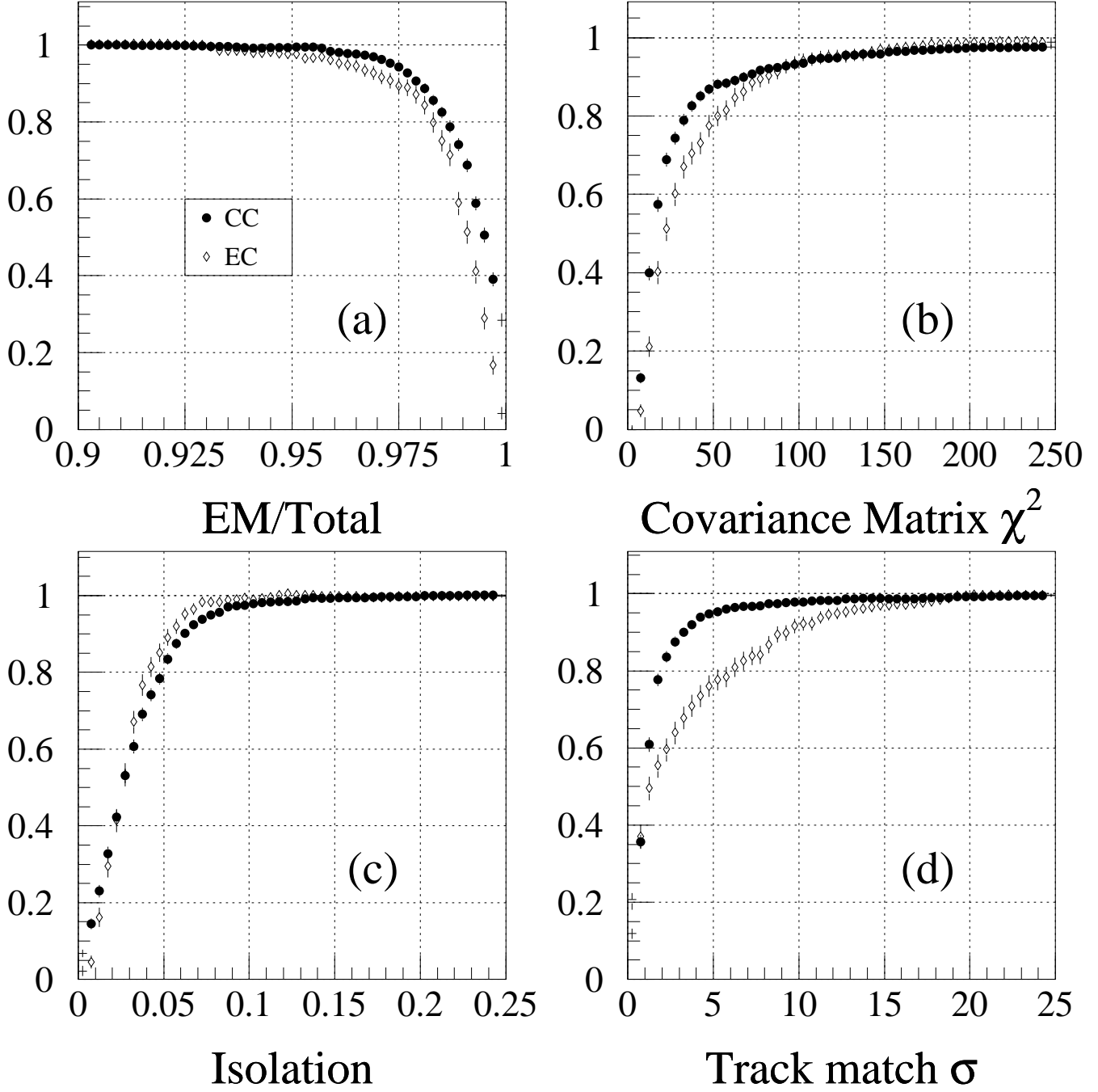


FIG. 12. Electron selection efficiencies for (a) the electron selection efficiency as a function of the fraction of the energy deposited in the EM calorimeter, (b) the H-matrix  $\chi^2$ , (c) the isolation variable  $f_{iso}$ , and (d) the track-match-significance,  $TMS$ . The solid circles are for CC electrons and the open diamonds are for EC electrons.

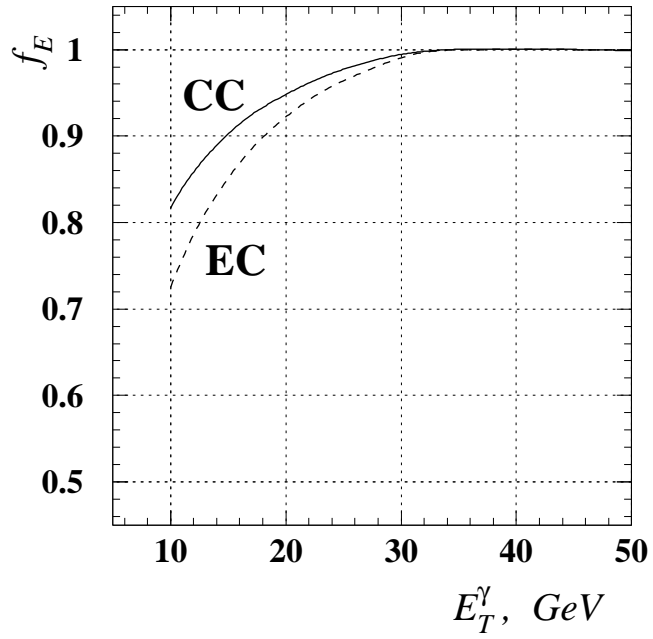


FIG. 13. The efficiency of the “Loose” photon H-matrix  $\chi^2$  selection criteria as a function of  $E_T^\gamma$ .

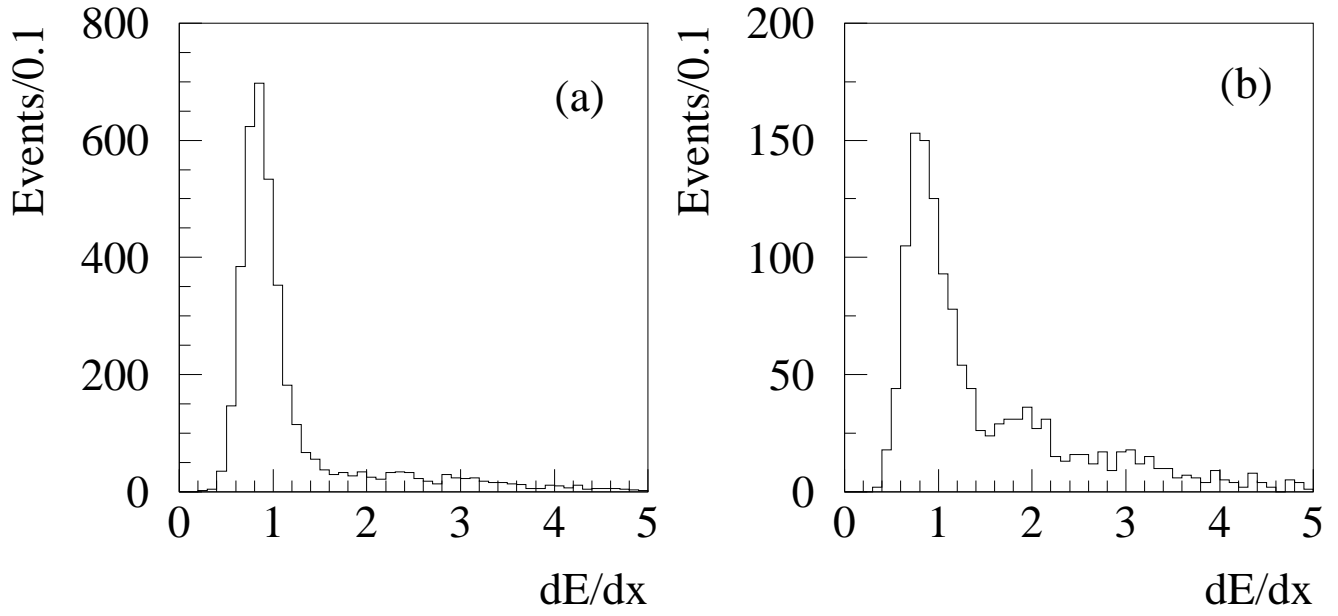


FIG. 14. (a) the  $dE/dx$  measured in the CDC for electrons from Z boson decays. (b) the  $dE/dx$  measured in the CDC for EM clusters in an inclusive jet sample.

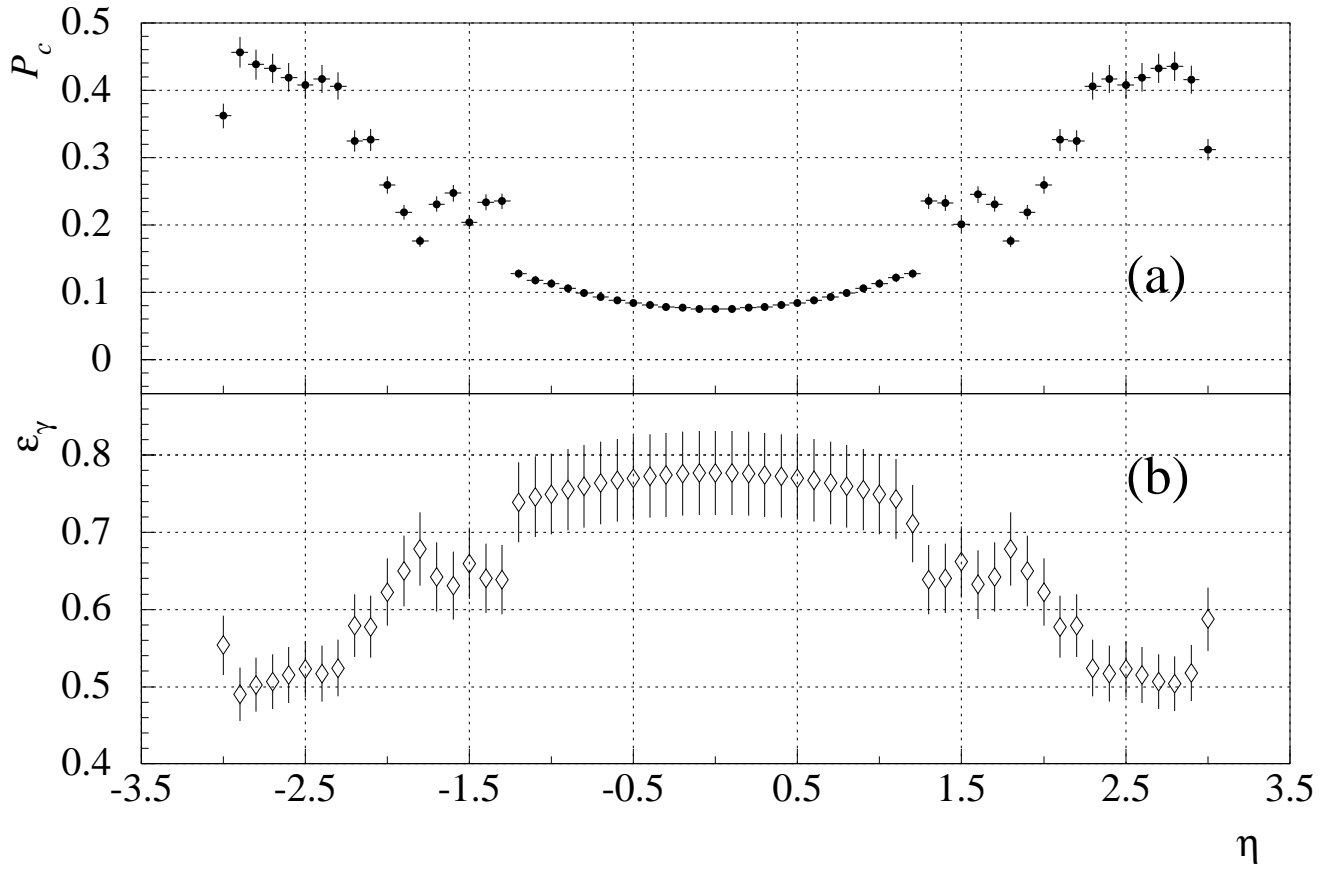


FIG. 15. (a)  $\eta$ -dependent probability for photon conversion ( $P_c$ ) in the material in front of the CDC and FDC ; (b)  $\eta$ -dependent efficiency of the photon identification ( $\epsilon_\gamma$ ) for high  $p_T$  photons for the  $Z\gamma$  “Loose” selection criteria. The uncertainty shown includes the statistical uncertainty plus a common systematic uncertainty of 5%.

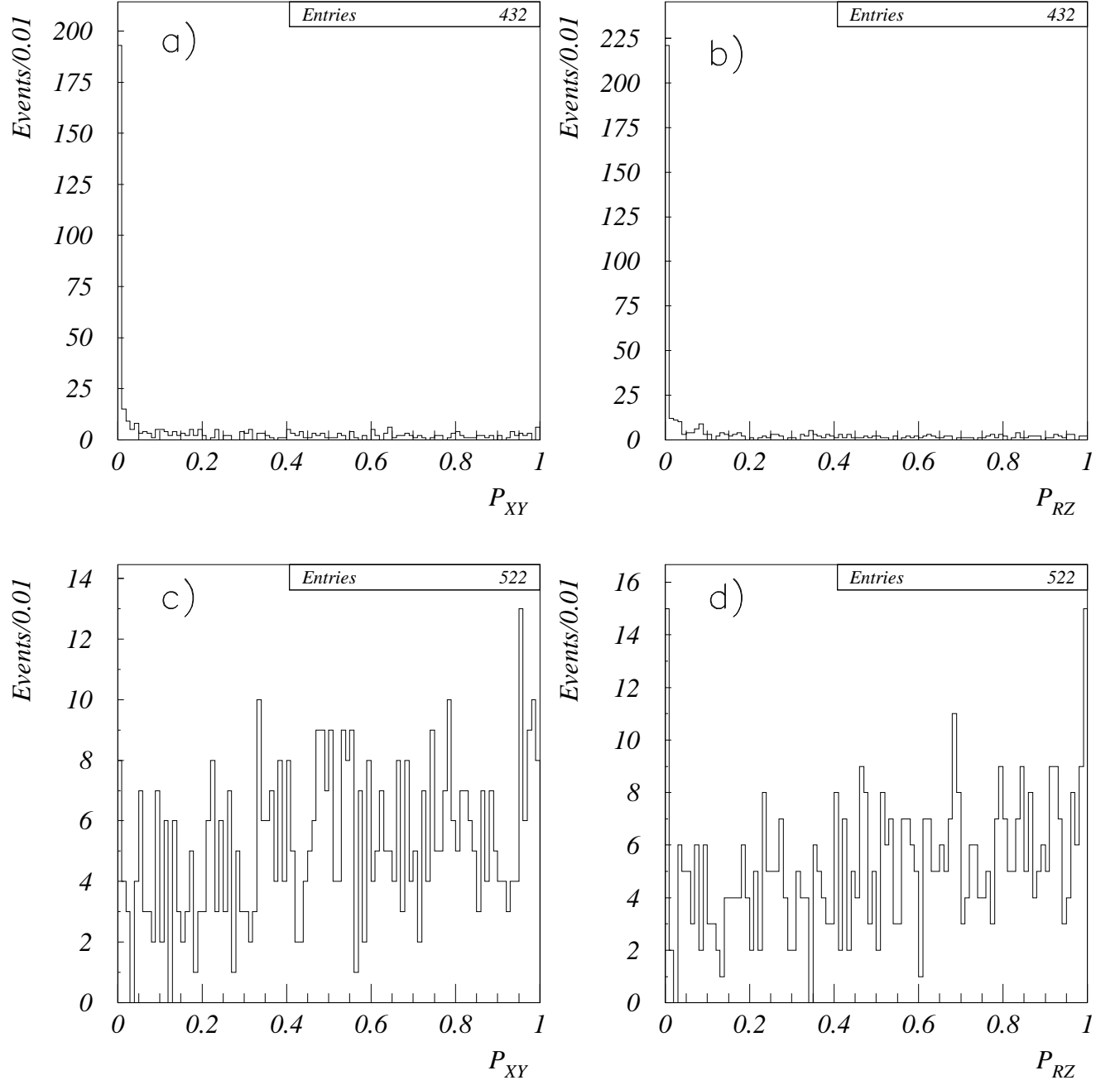


FIG. 16. Probability distributions  $P_{XY}$  and  $P_{RZ}$ . (a) and (b) are from photons resulting from cosmic ray bremsstrahlung. (c) and (d) are from electrons from  $Z$  boson decays.

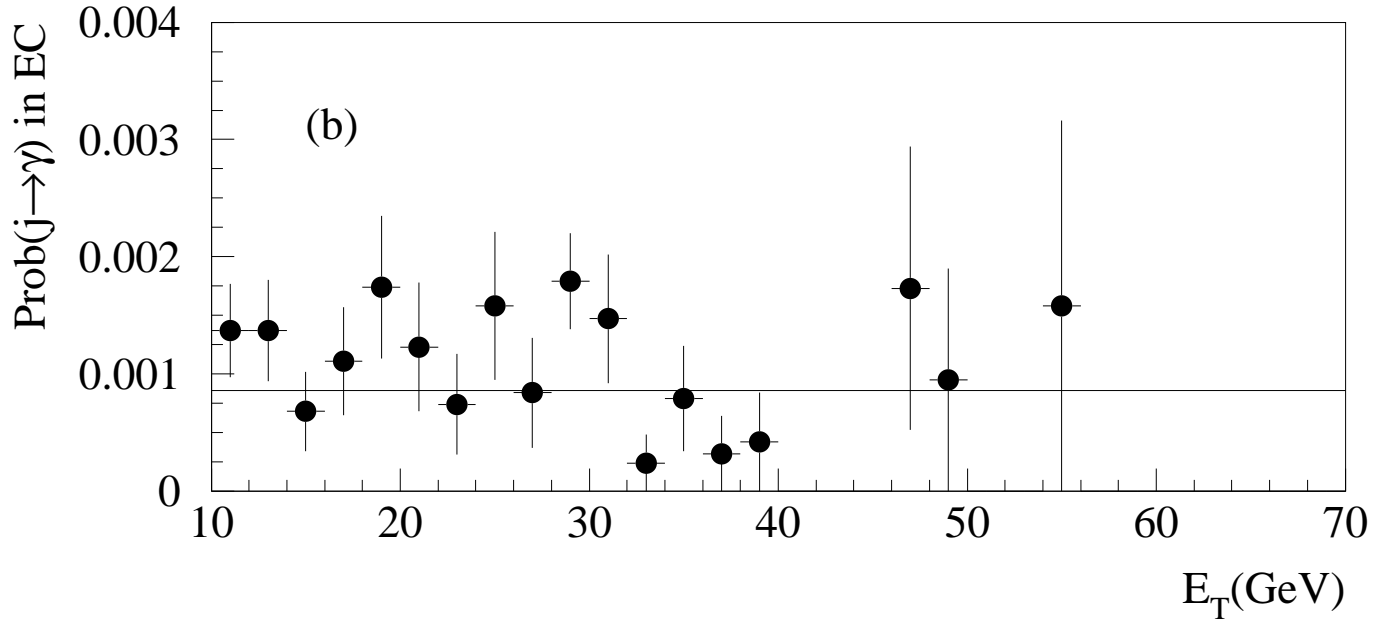
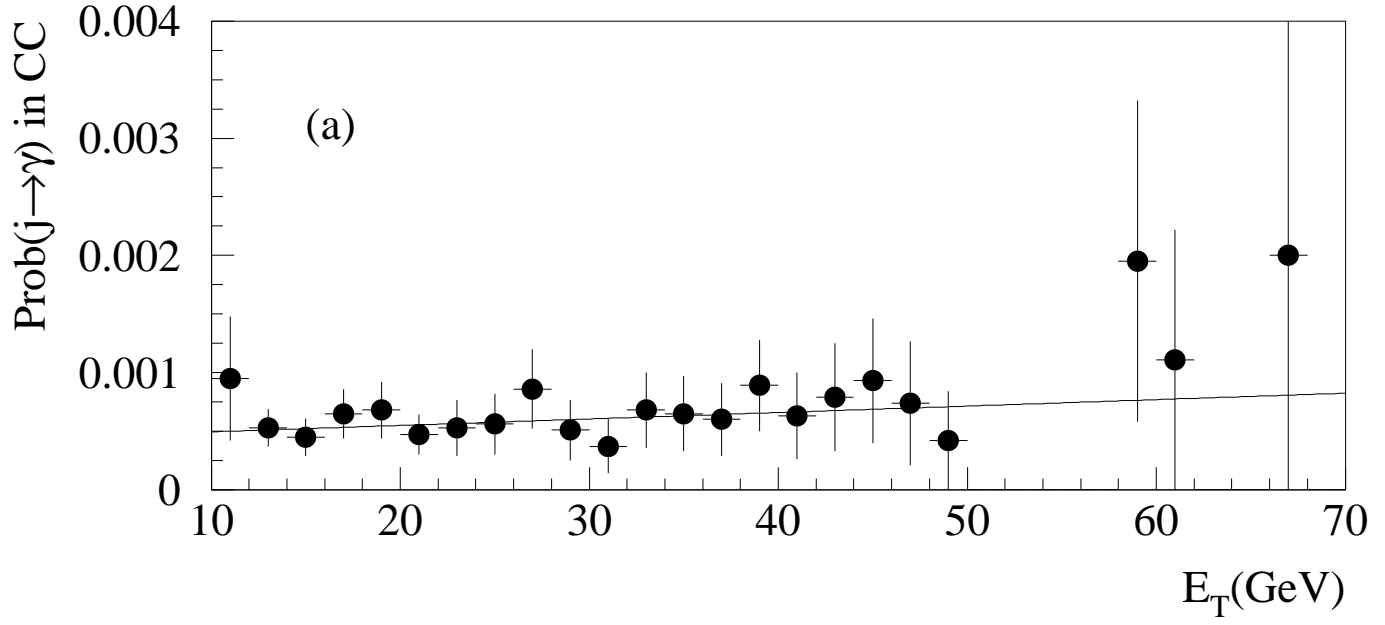


FIG. 17. The probability of a jet to be misidentified as a photon as a function of  $E_T$  (before the removal of the contribution from direct photons) for the “Loose” photon selection criteria in the CC (a) and EC (b).

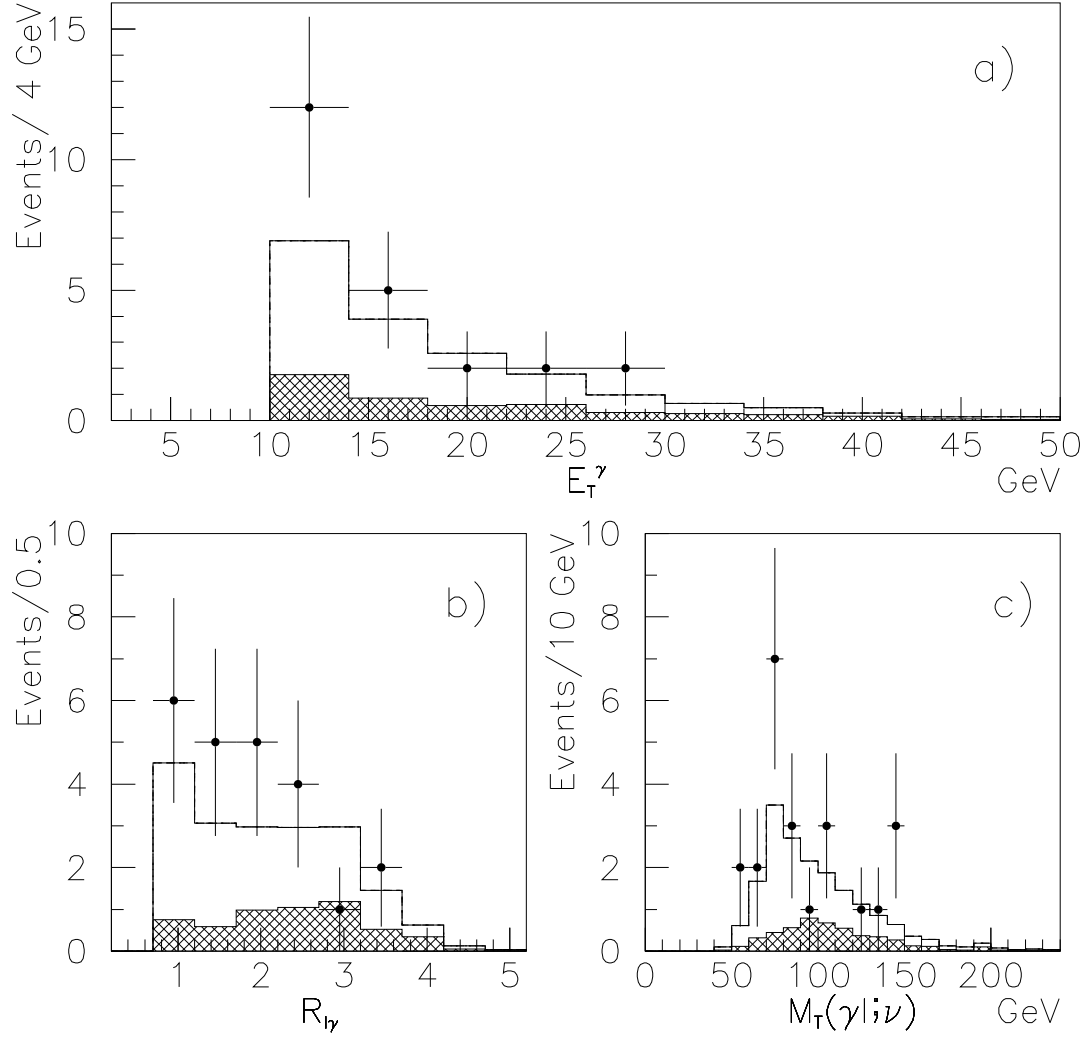


FIG. 18. Distribution of (a)  $E_T^\gamma$ , (b)  $\Delta R_{l\gamma}$  and (c)  $M_T(\gamma\ell;\nu)$  for the  $W(e\nu)\gamma + W(\mu\nu)\gamma$  combined sample. The points are data. The shaded areas represent the estimated background, and the solid histograms are the expected signal from the Standard Model plus the estimated background.

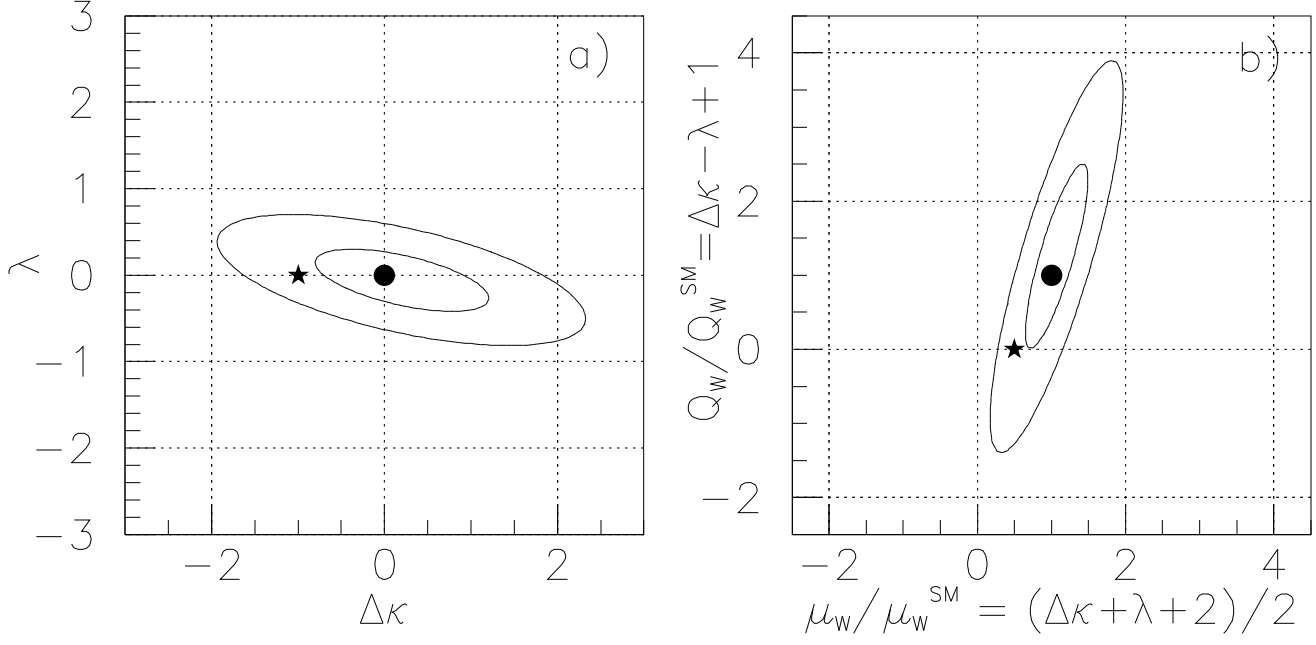


FIG. 19. Limits on (a) CP-conserving anomalous coupling parameters  $\Delta\kappa$  and  $\lambda$ , and on (b) the magnetic dipole,  $\mu_W$ , and electric quadrupole,  $Q_W^e$ , moments. The ellipses represent the 68% and 95% CL exclusion contours. The symbol, ●, represents the Standard Model values, while the symbol, ★, indicates the  $U(1)_{EM}$ -only coupling of the  $W$  boson to a photon,  $\Delta\kappa = -1$  and  $\lambda = 0$  ( $\mu_W = e/2m_W$  and  $Q_W^e = 0$ ).



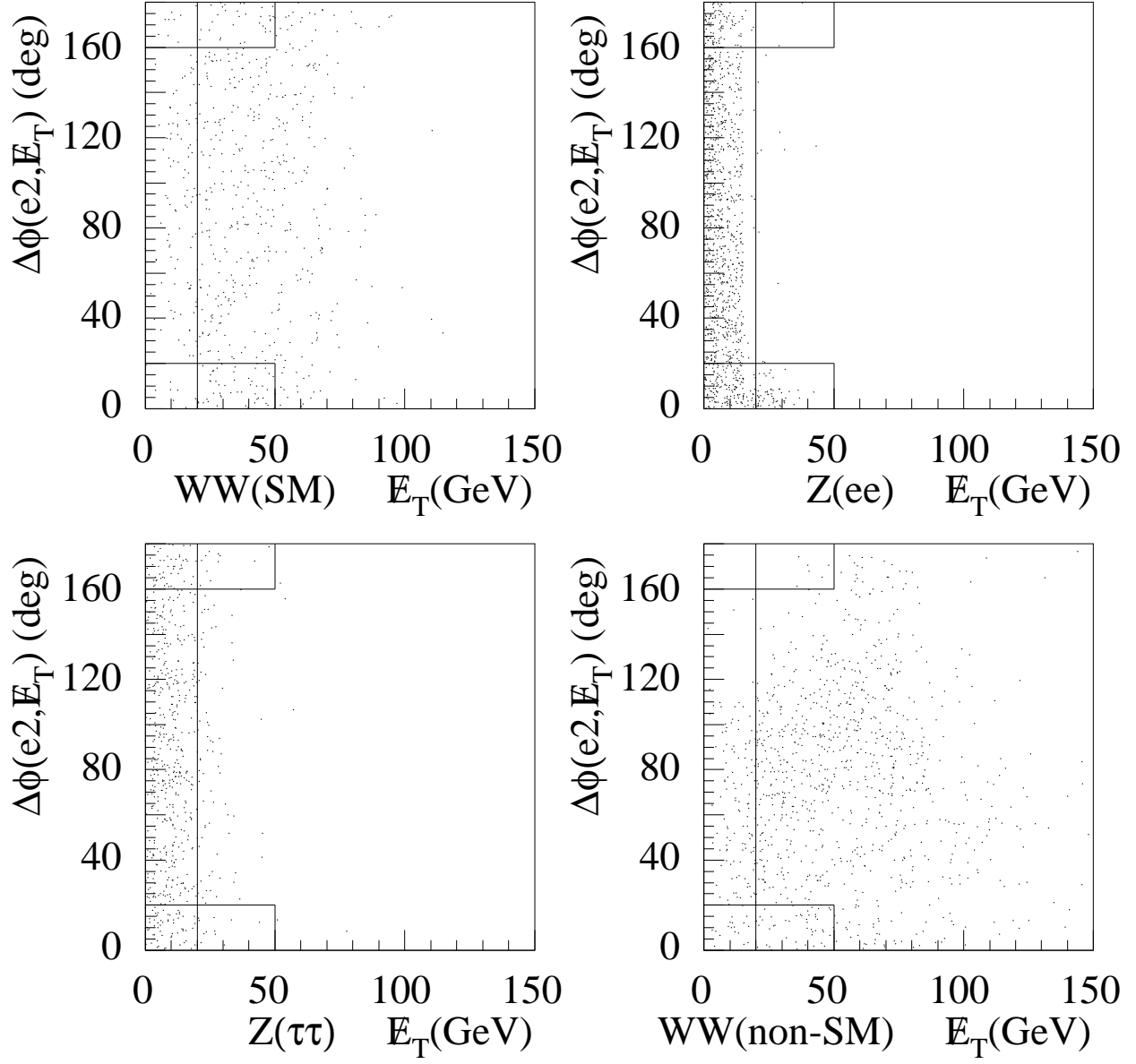


FIG. 20.  $\Delta\phi(p_T^e, \cancel{E}_T)$  vs  $\cancel{E}_T$  distributions for  $WW \rightarrow (e\nu)(e\nu)$  with the SM couplings,  $Z \rightarrow ee$ ,  $Z \rightarrow \tau\tau \rightarrow ee\nu\bar{\nu}\nu\bar{\nu}$  and  $WW \rightarrow ee\nu\bar{\nu}$  with the non-SM couplings.

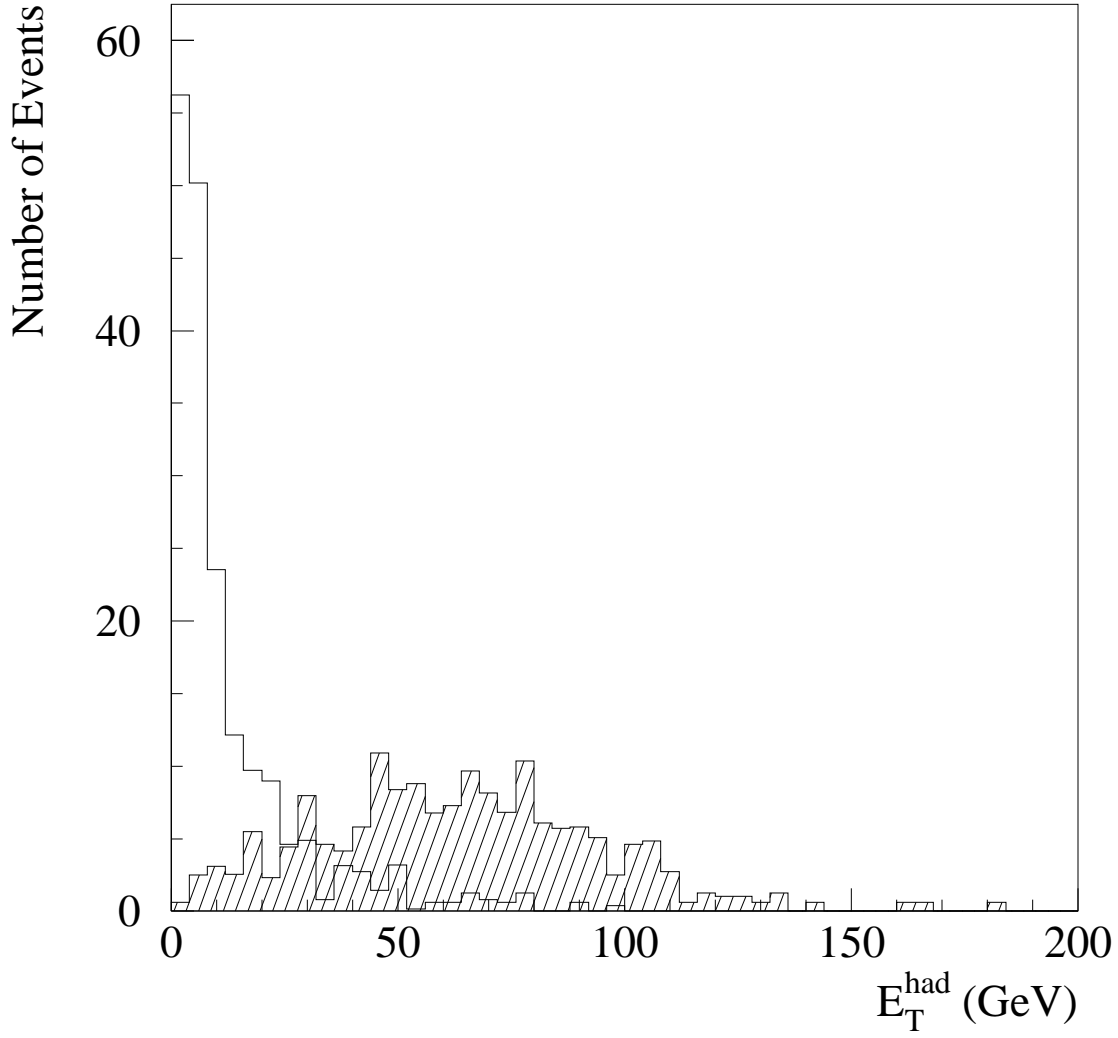


FIG. 21.  $E_T^{\text{had}}$  for Monte Carlo  $WW$  (open histogram) and  $t\bar{t}$  events (shaded histogram) with  $M_{t\text{op}} = 160 \text{ GeV}/c^2$  ( $\int L dt \sim 20 \text{ fb}^{-1}$ ). Events with  $E_T^{\text{had}} \geq 40 \text{ GeV}$  were rejected.

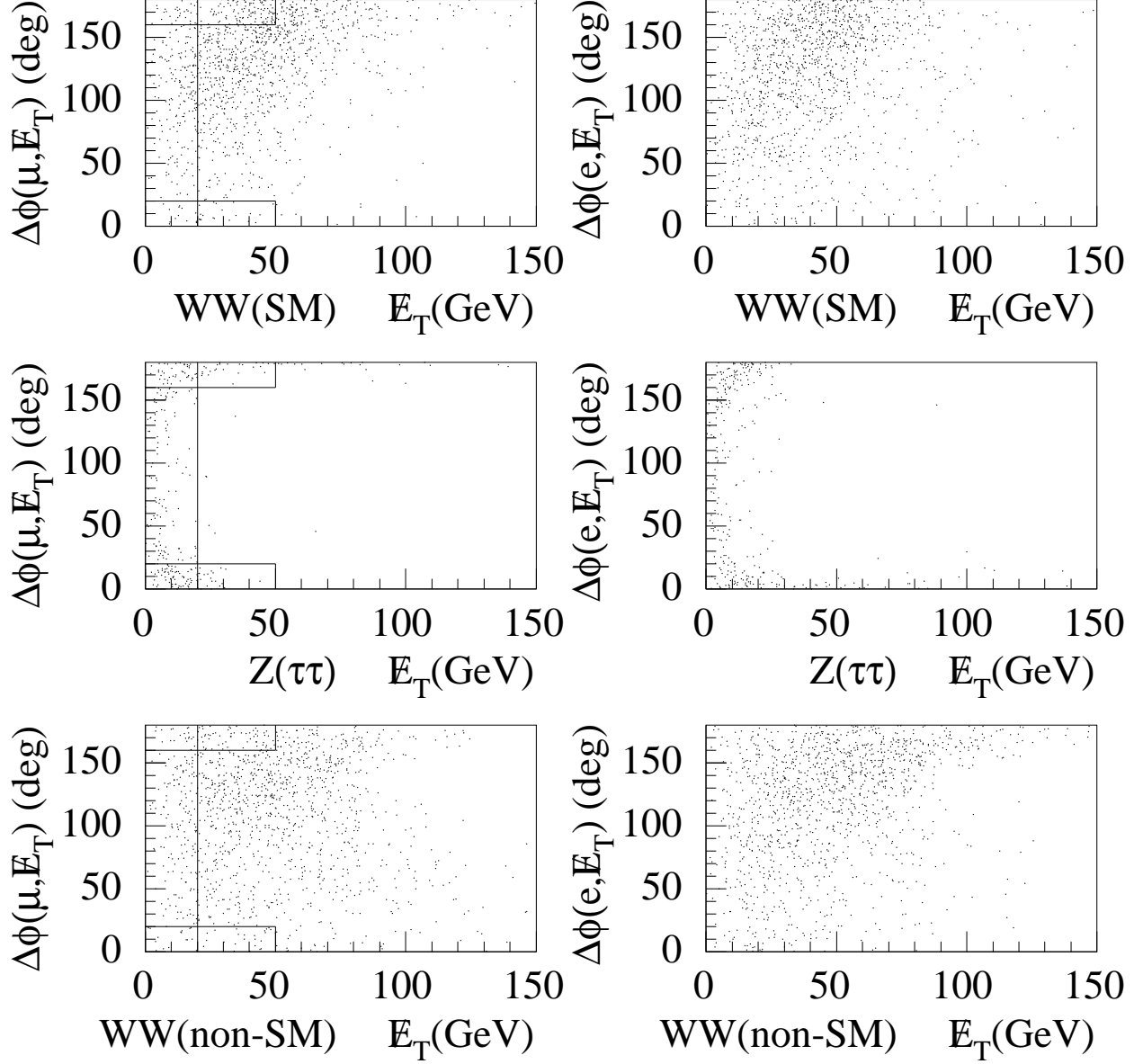


FIG. 22.  $\Delta\phi(p_T^\ell, E_T)$  vs  $E_T$  distributions for  $WW \rightarrow e\mu$  with the SM couplings,  $Z \rightarrow \tau\tau \rightarrow e\mu\nu\bar{\nu}\nu\bar{\nu}$  and  $WW \rightarrow e\mu$  with non-SM couplings.

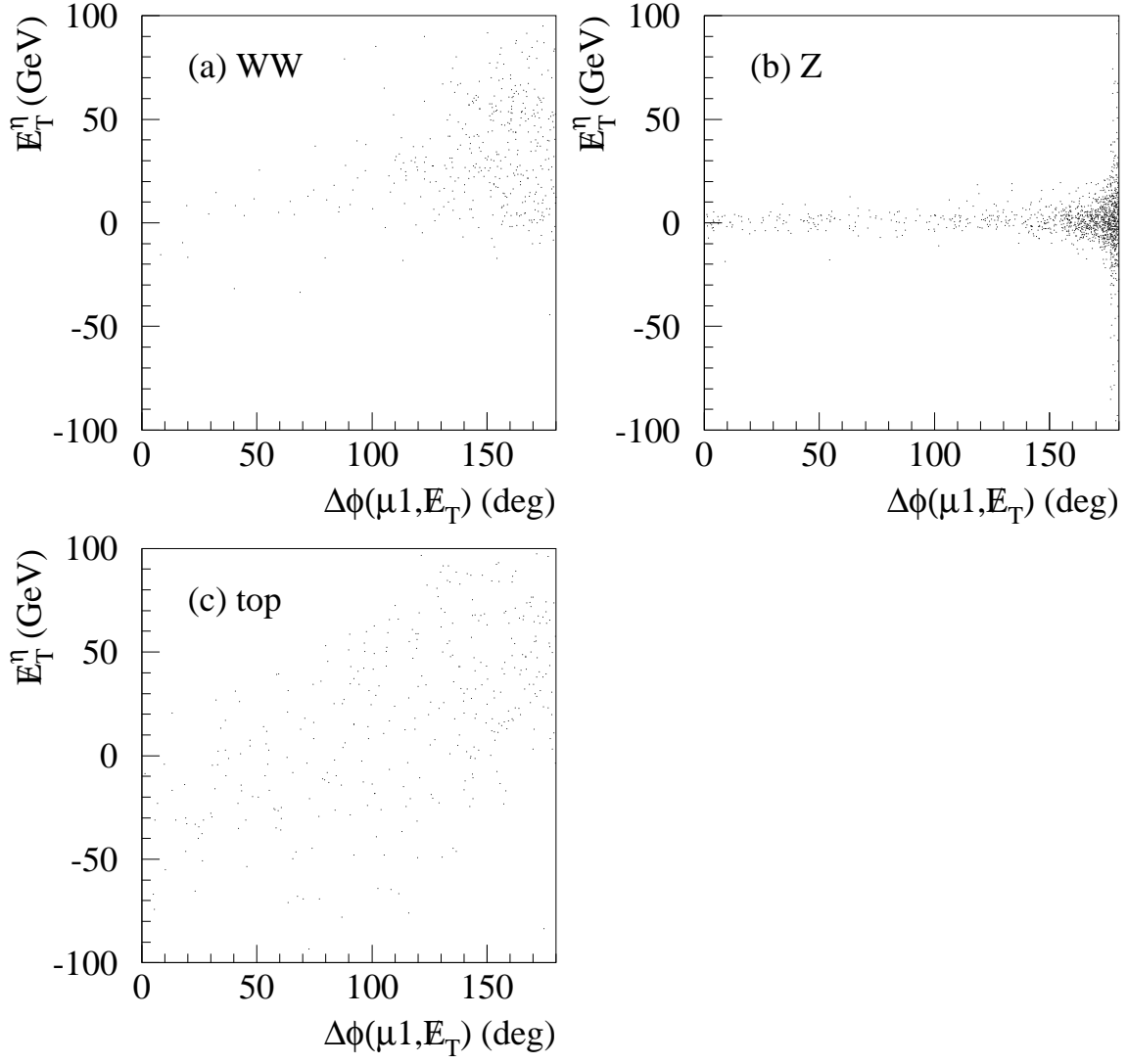


FIG. 23.  $E_T^{\text{miss}}$  vs  $\Delta\phi(p_T^{\mu 1}, E_T)$  distributions for  $WW \rightarrow \mu\mu\nu\bar{\nu}$  with SM couplings,  $Z \rightarrow \mu\mu$ , and  $t\bar{t}$  events.

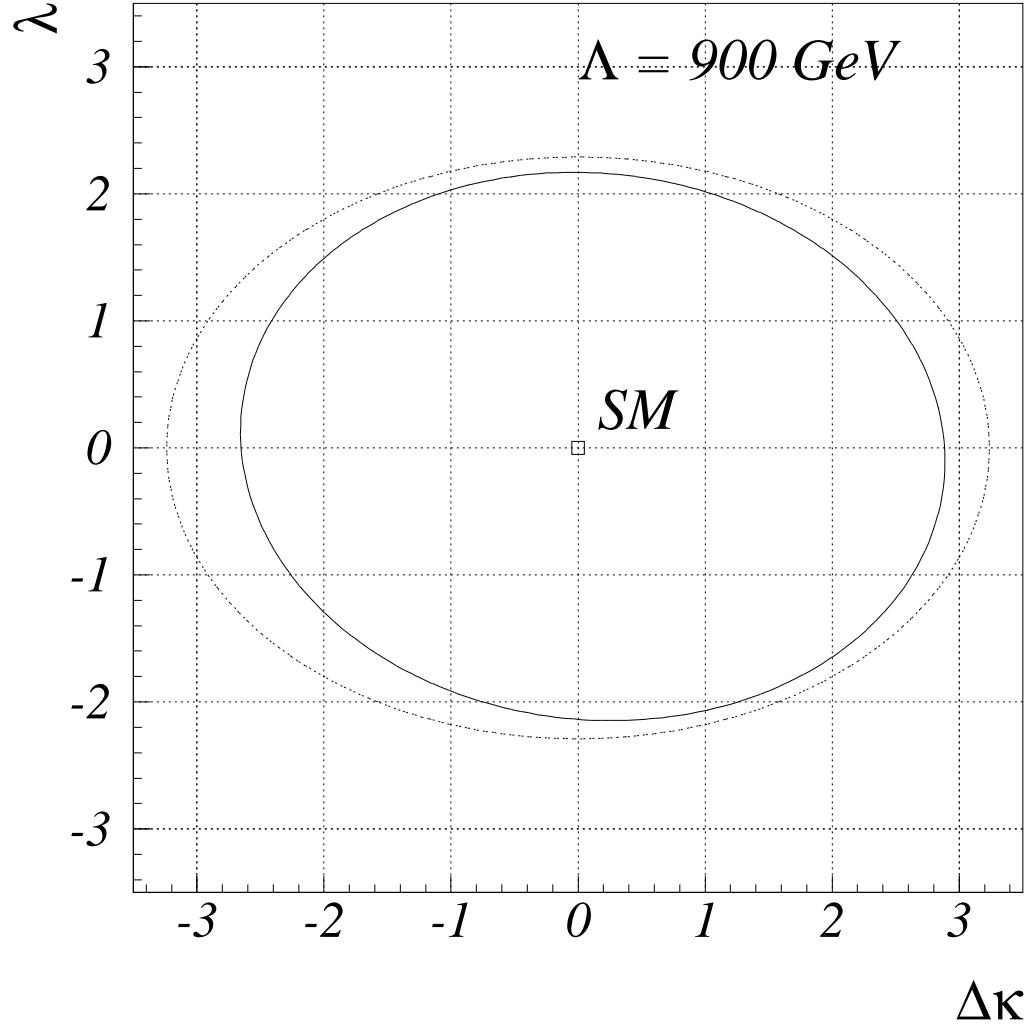


FIG. 24. 95% CL limits on the CP-conserving anomalous couplings  $\lambda$  and  $\Delta\kappa$ , assuming that  $\lambda_\gamma = \lambda_Z$  and  $\Delta\kappa_\gamma = \Delta\kappa_Z$ . The dotted contour is the unitarity limit for the form factor scale  $\Lambda = 900$  GeV which was used to set the coupling limits.

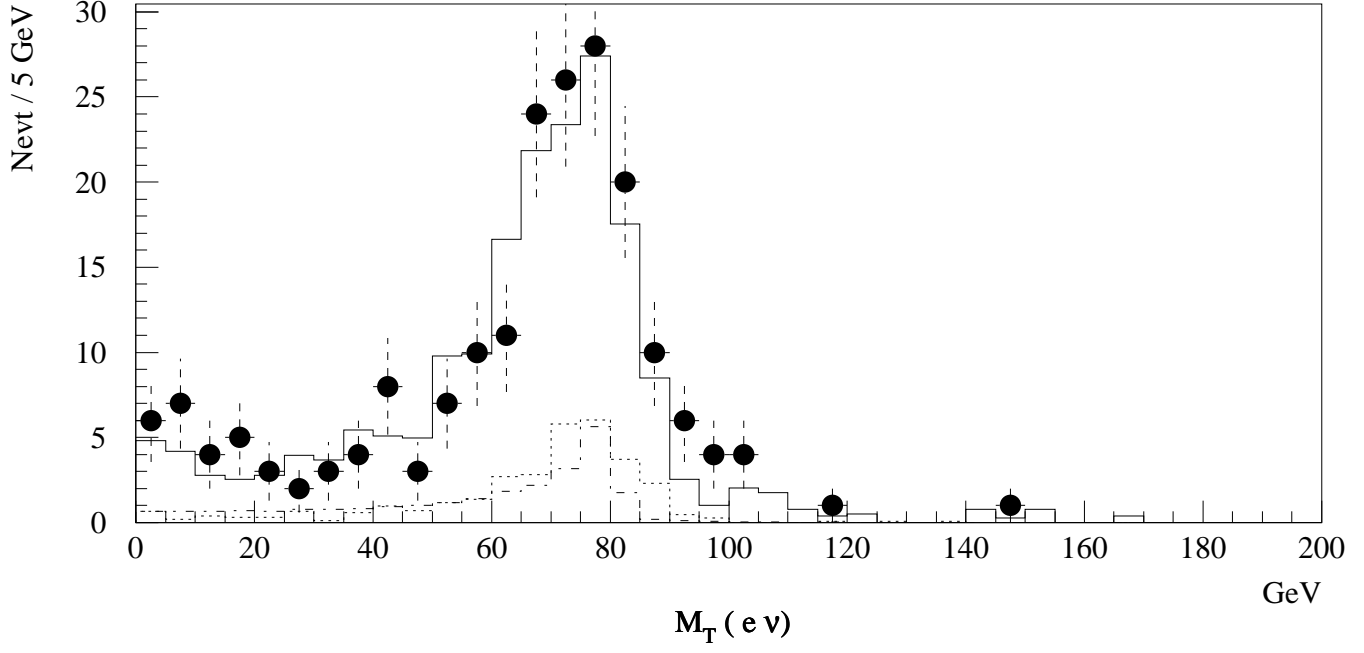


FIG. 25. The distribution of the transverse mass of the electron and  $\cancel{E}_T$  for the data (points), major backgrounds (solid line), 10 times SM  $WW$  signal (dotted), and  $WW$  with  $\Delta\kappa = 2$   $\lambda = 0$  (dot-dash). The backgrounds are normalized as described in the text.

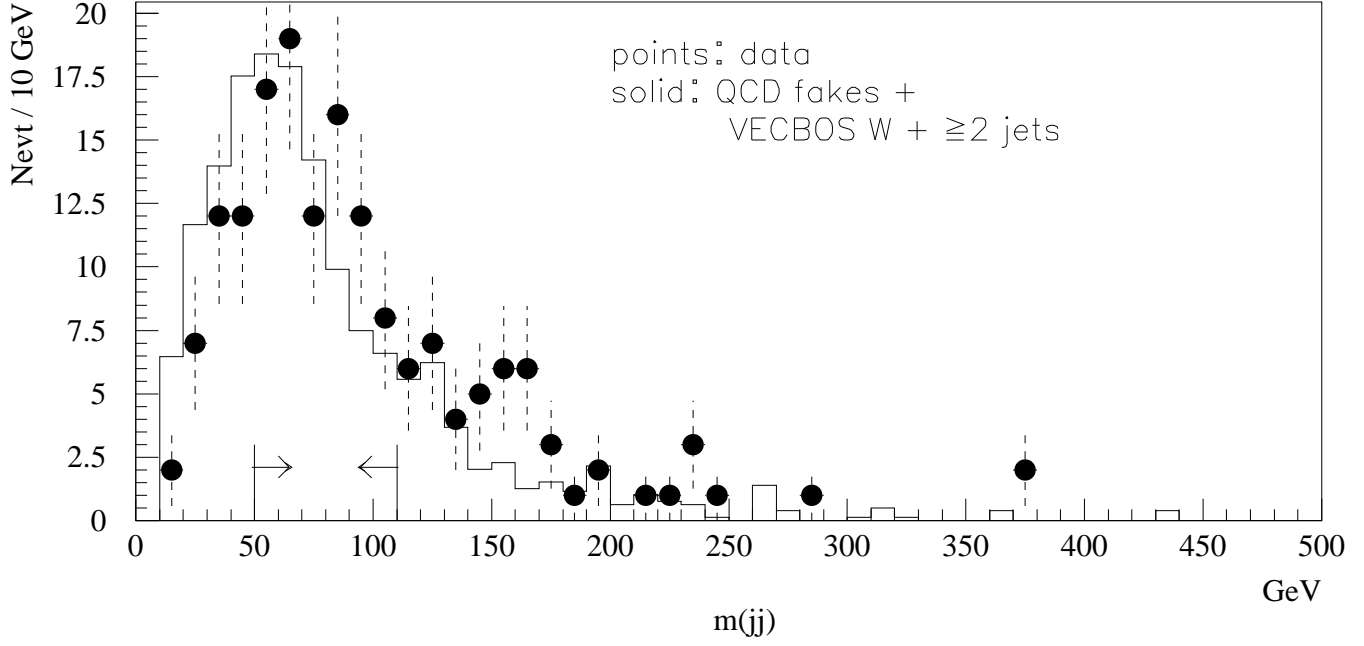


FIG. 26. The distribution of the dijet invariant mass for the data and major backgrounds. The backgrounds are normalized as described in the text. The arrows indicate the region accepted by the dijet mass selection criterion.

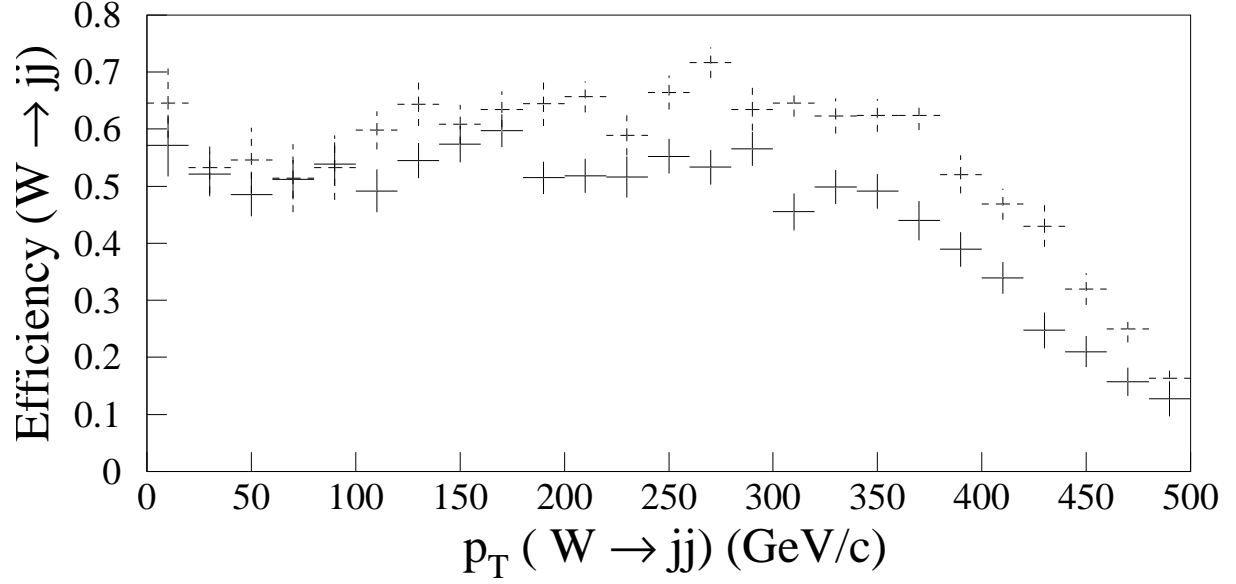


FIG. 27. Efficiency for reconstructing the dijets and for the dijet mass selection for  $W \rightarrow jj$  vs.  $p_T(W)$ . The solid crosses are the results from ISAJET. The dashed crosses are results from PYTHIA.



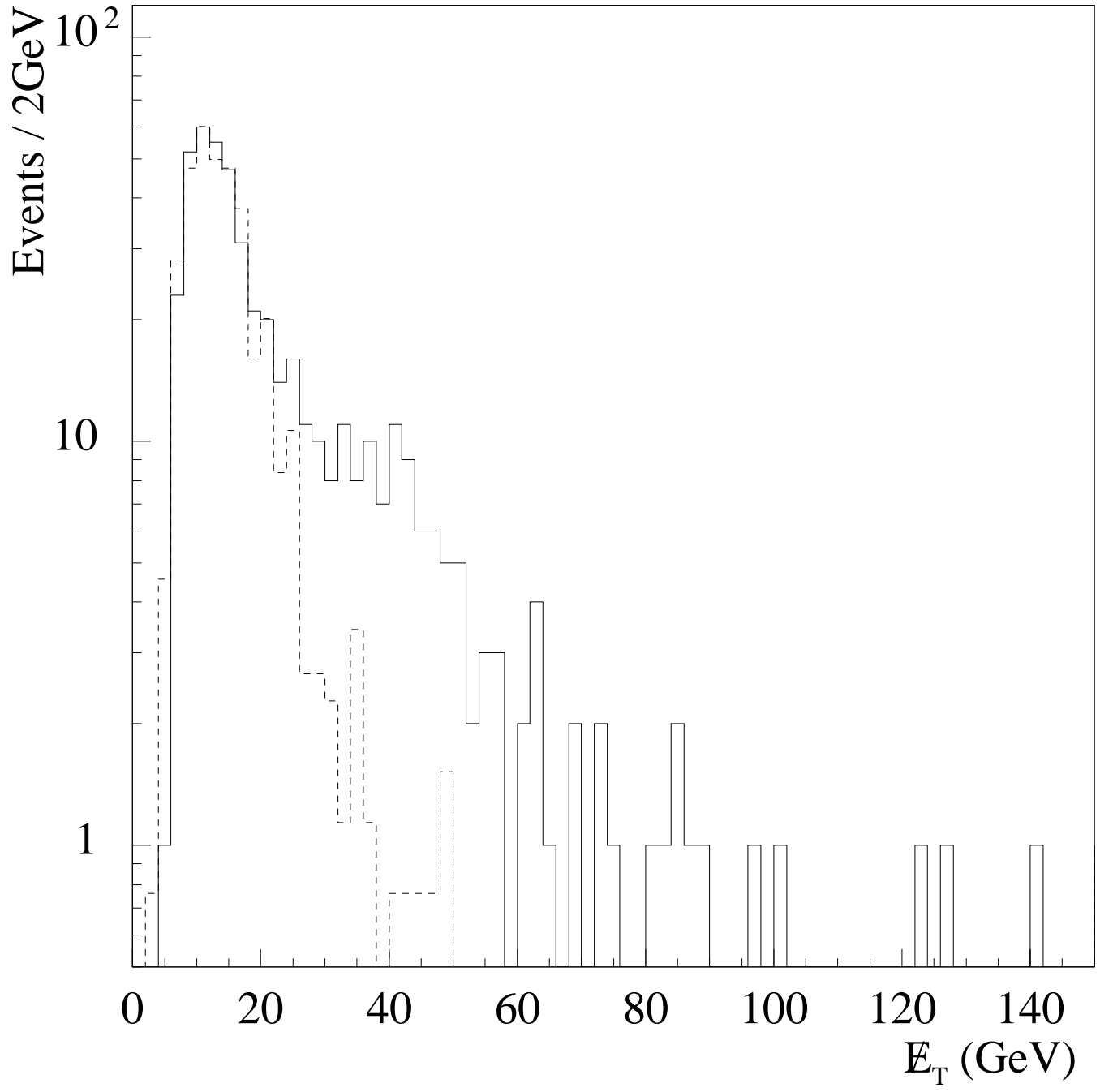


FIG. 28. Distribution of the  $E_T$  for the  $WW/WZ$  candidates (solid) and the QCD fake sample (dashed) before the dijet mass selection.

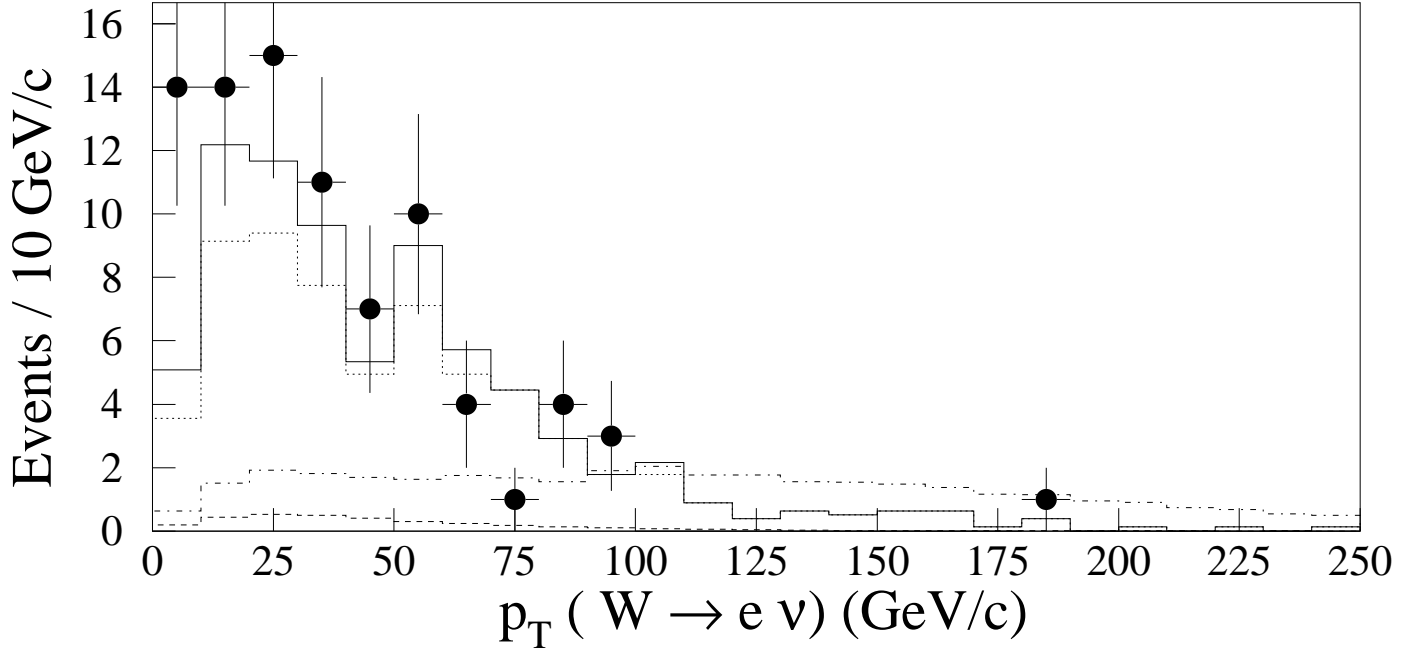


FIG. 29.  $p_T$  distributions of the  $e\nu$  system: data (points),  $W + \geq 2$  jets background (dotted), total background (solid), and Monte Carlo predictions for the SM (dashed) and non-SM couplings  $\Delta\kappa = 2$   $\lambda = 0$  (dot-dashed)  $WW$  production.

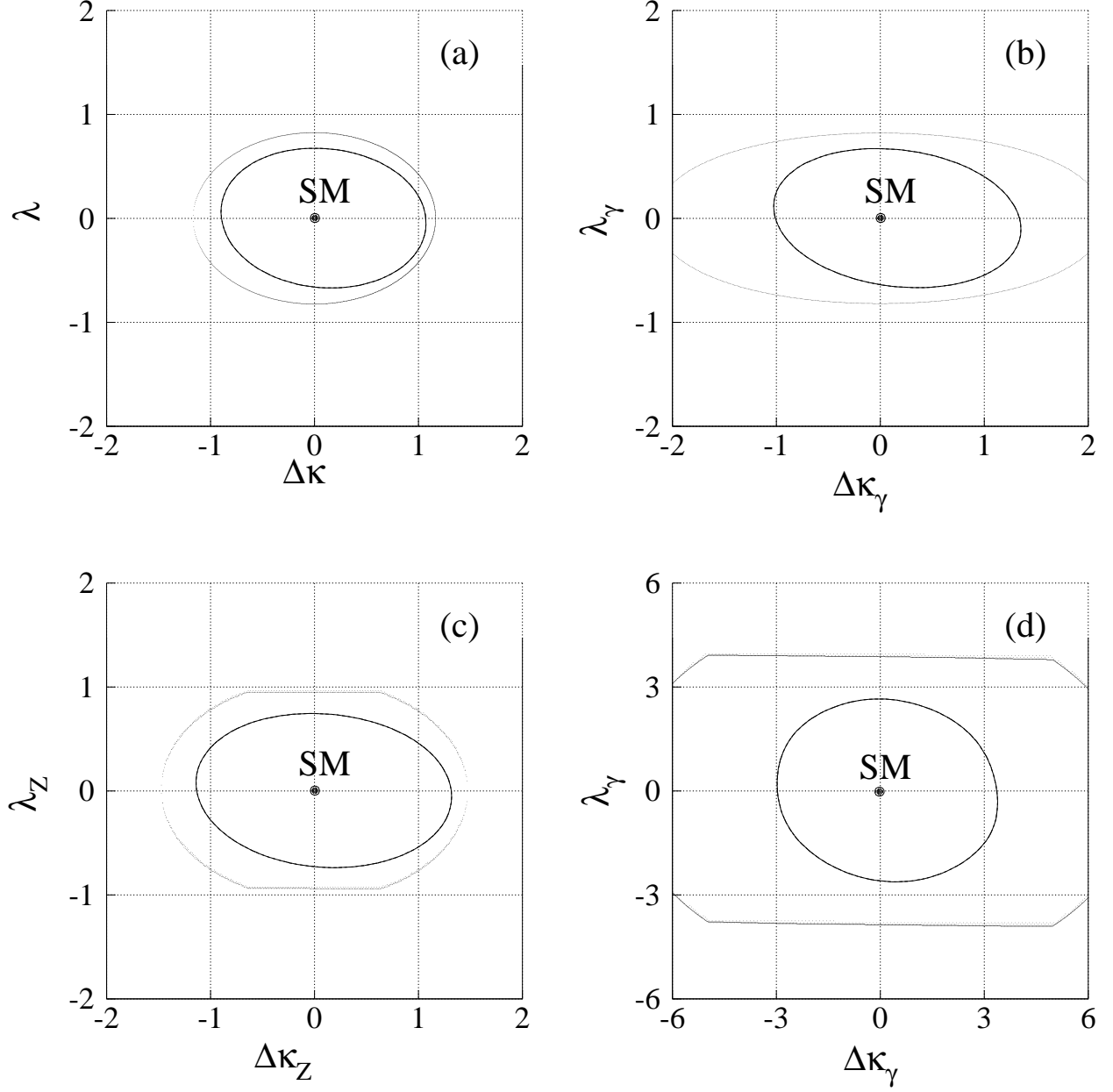


FIG. 30. Contour limits on anomalous coupling parameters at the 95% CL (inner curves) and limits from  $S$ -matrix unitarity (outer curves) for the assumptions a)  $\lambda_\gamma = \lambda_Z$  and  $\Delta\kappa_\gamma = \Delta\kappa_Z$ , b) HISZ relations, c) SM  $WW\gamma$  couplings and d) SM  $WWZ$  couplings.  $\Lambda = 1500$  GeV was used for (a), (b), and (c).  $\Lambda = 1000$  GeV was used for (d).

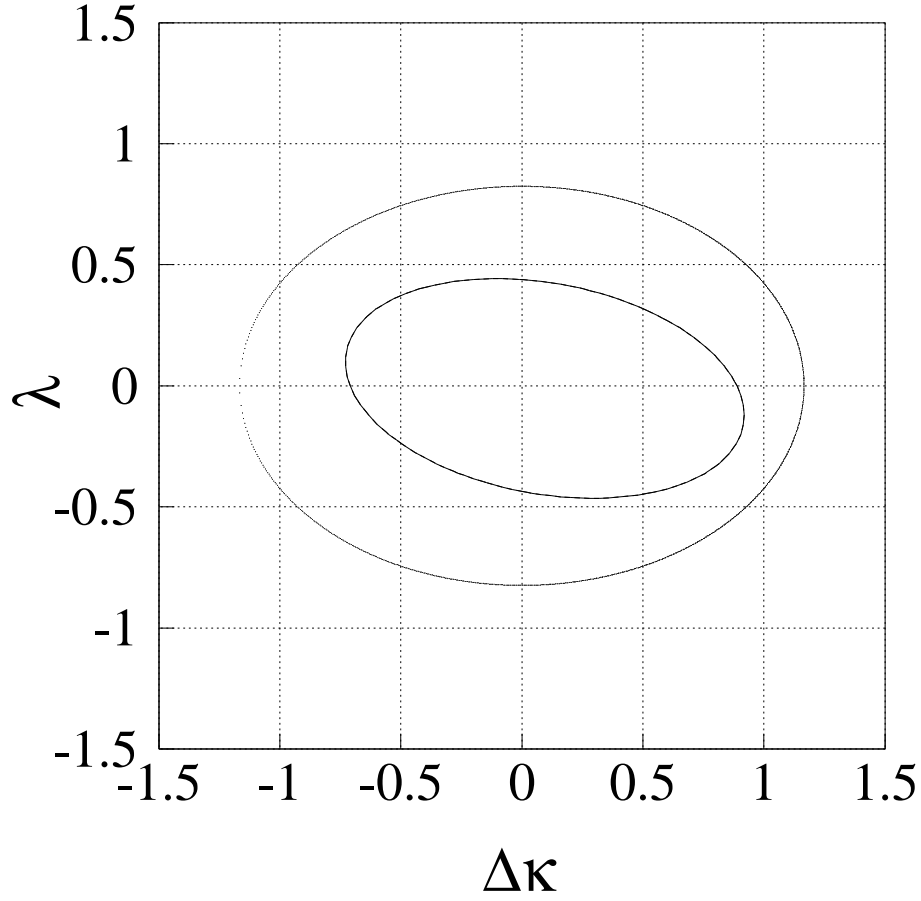


FIG. 31. 95% CL limits (inner contour) on  $\lambda$  and  $\Delta\kappa$ , assuming the  $WW\gamma$  and  $WWZ$  couplings are equal and  $\Lambda = 1500$  GeV, from the combined  $W\gamma$ ,  $WW$ , and  $WZ$  results. The outer contour is the limit from  $s$ -matrix unitarity.

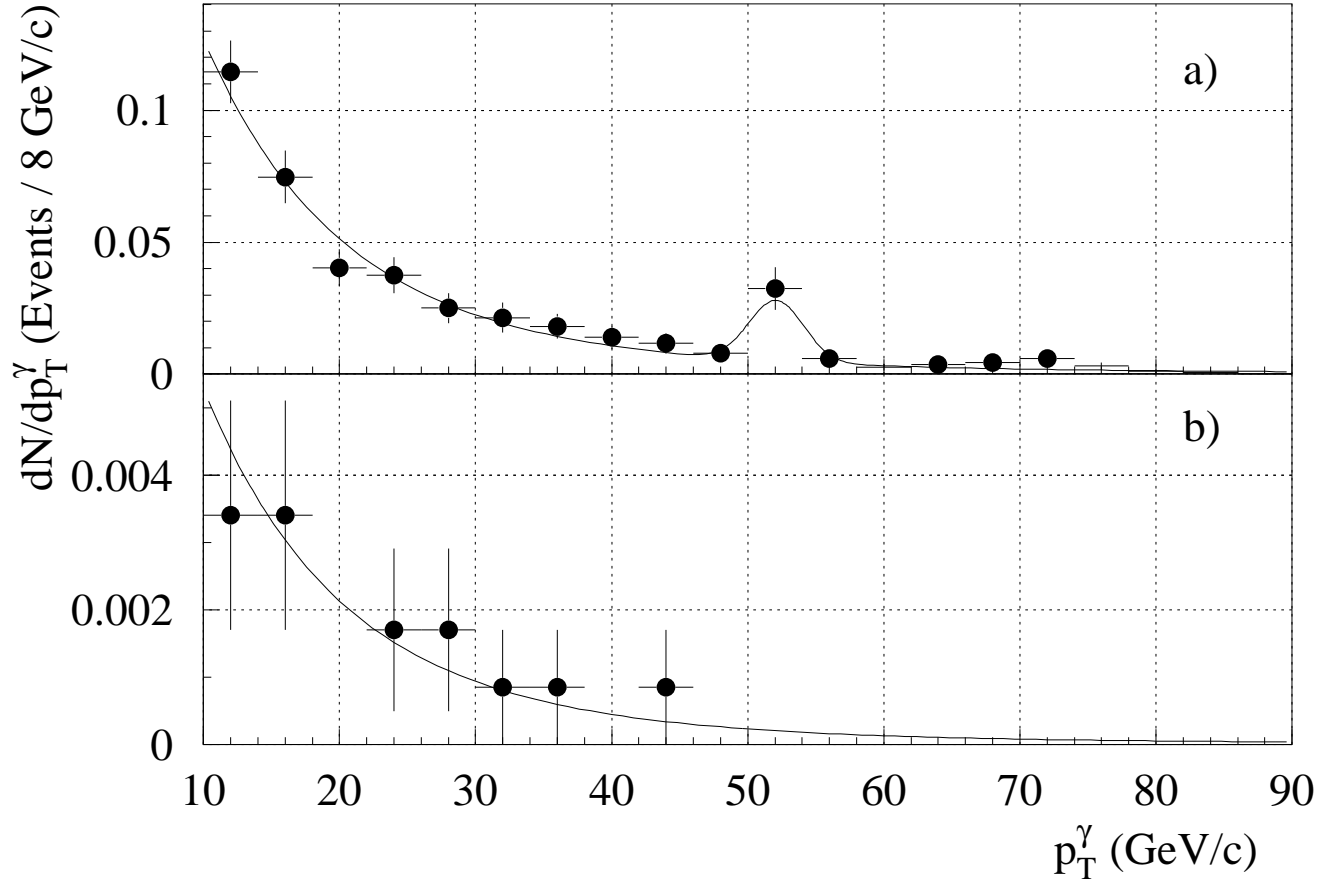


FIG. 32. a) QCD background in the  $ee\gamma$  channel. The bump around 50 GeV/c is due to the electrons from  $Z$  boson decays where a jet mimics an electron and an electron mimics a photon. b) QCD background in the  $\mu\mu\gamma$  channel. The fit is described in the text.

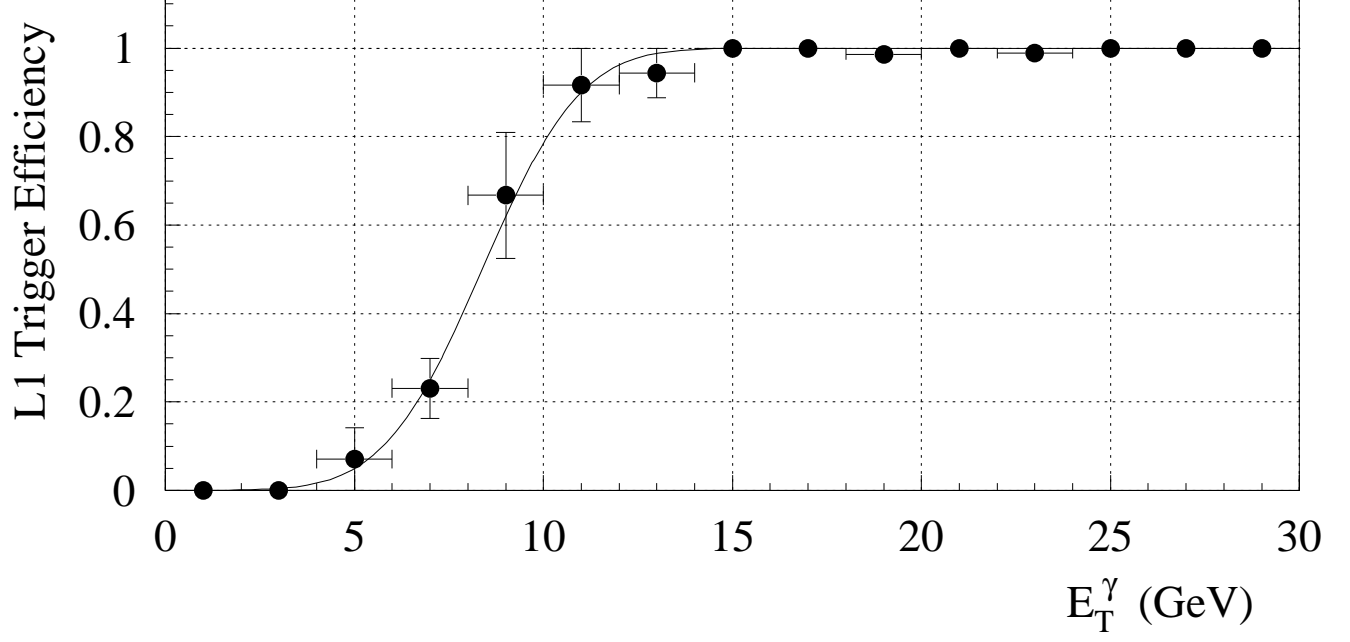


FIG. 33. Efficiency as a function of photon  $E_T$  for the level 1 EM trigger with threshold at 7 GeV. The minimum allowed photon  $E_T$  is 10 GeV.

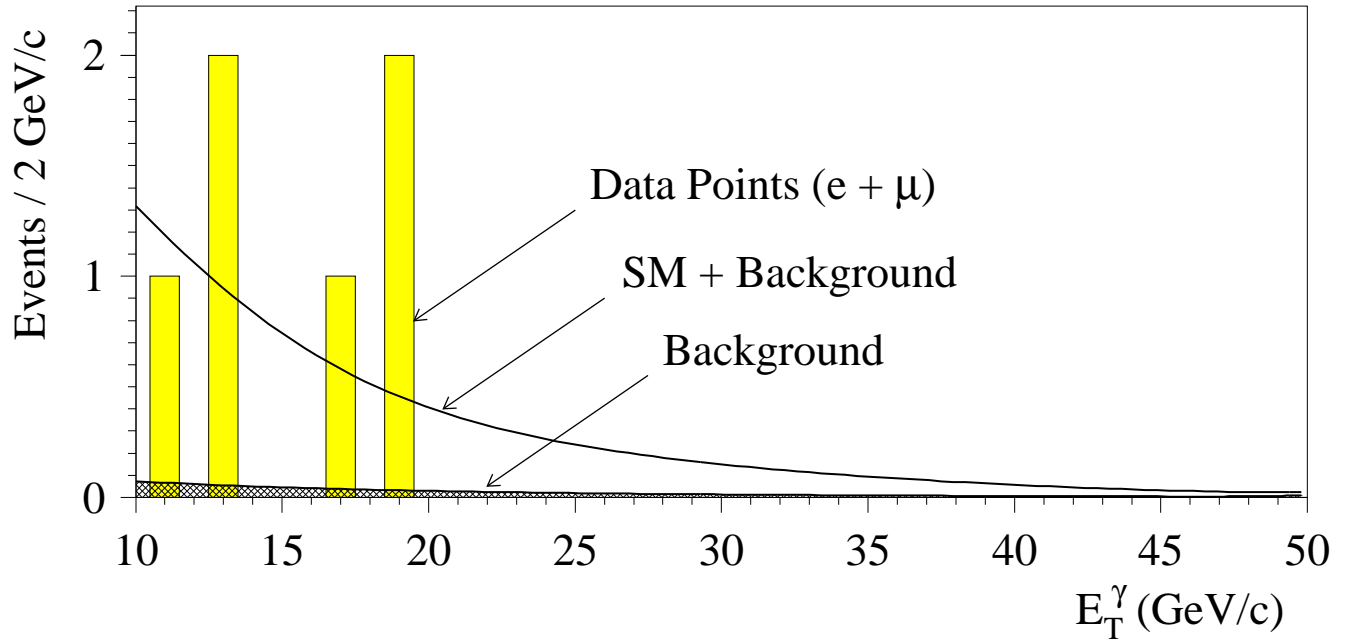


FIG. 34. Transverse energy spectrum of photons in  $ee\gamma$  and  $\mu\mu\gamma$  events. The shadowed bars correspond to the data, the hatched curve represents the total for background, and the solid line shows the sum of SM predictions and background.

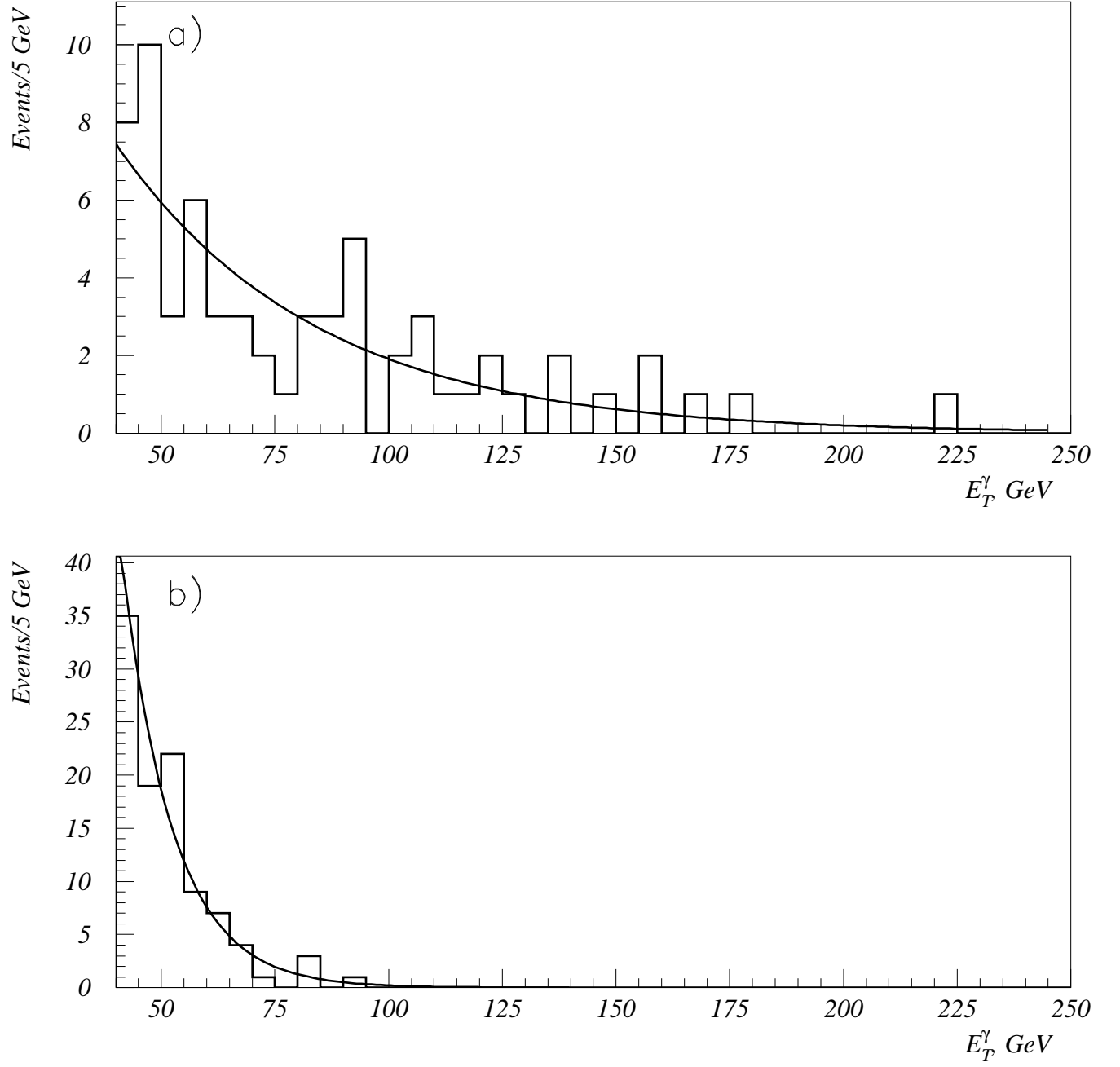


FIG. 35. Shape of the bremsstrahlung photon spectrum for the background due to cosmic ray and beam halo muons in the a) CC and b) EC calorimeters. The solid lines are the resulting fitted parameterizations.



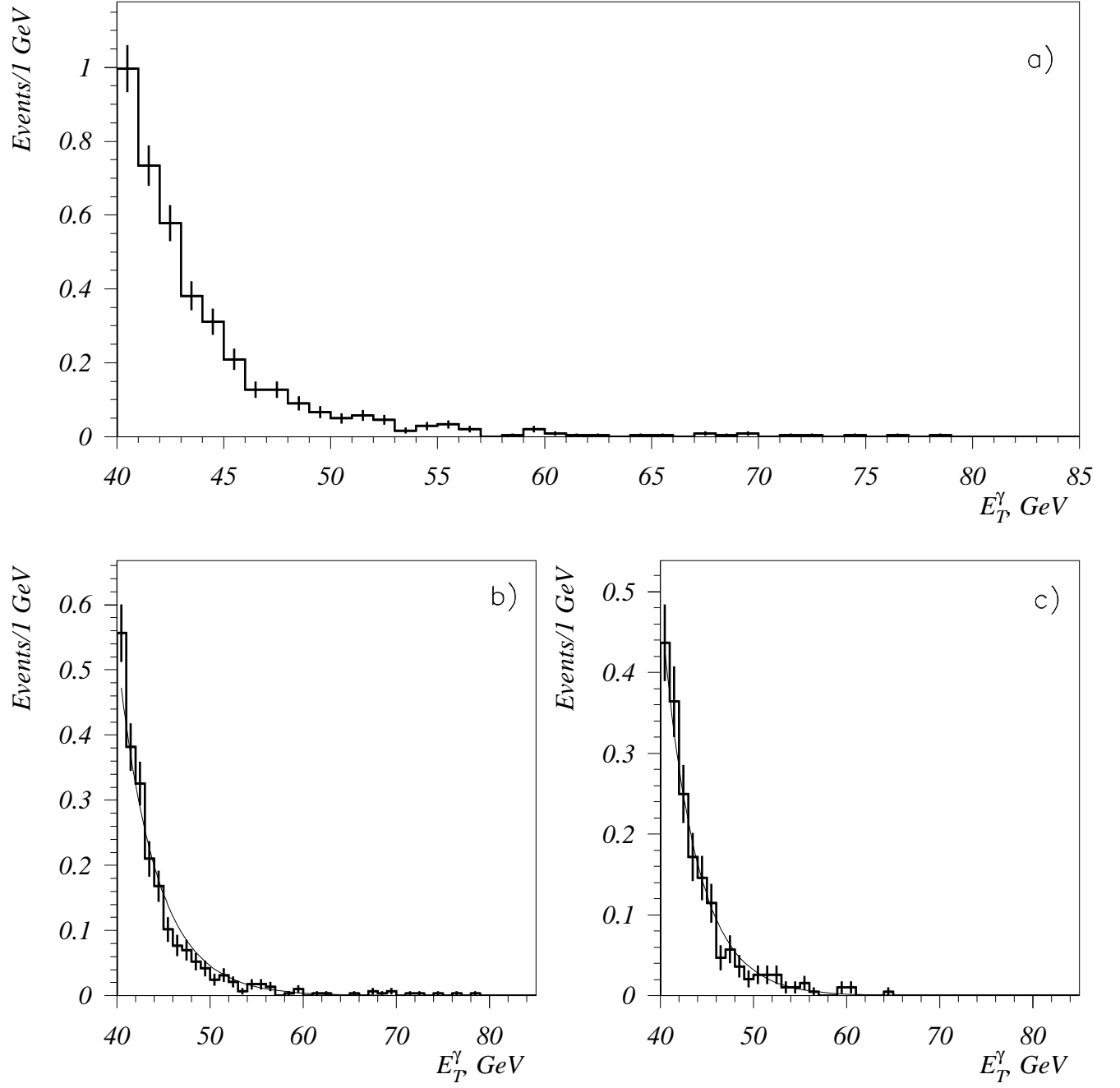


FIG. 36. Shape of the photon spectrum for the background due to  $W \rightarrow e\nu$  in the  $Z\gamma \rightarrow \nu\nu\gamma$  analysis. (a) is the spectrum in the CC and EC. (b) and (c) are the individual spectra in the CC and EC where the fits to the background are shown (lines).

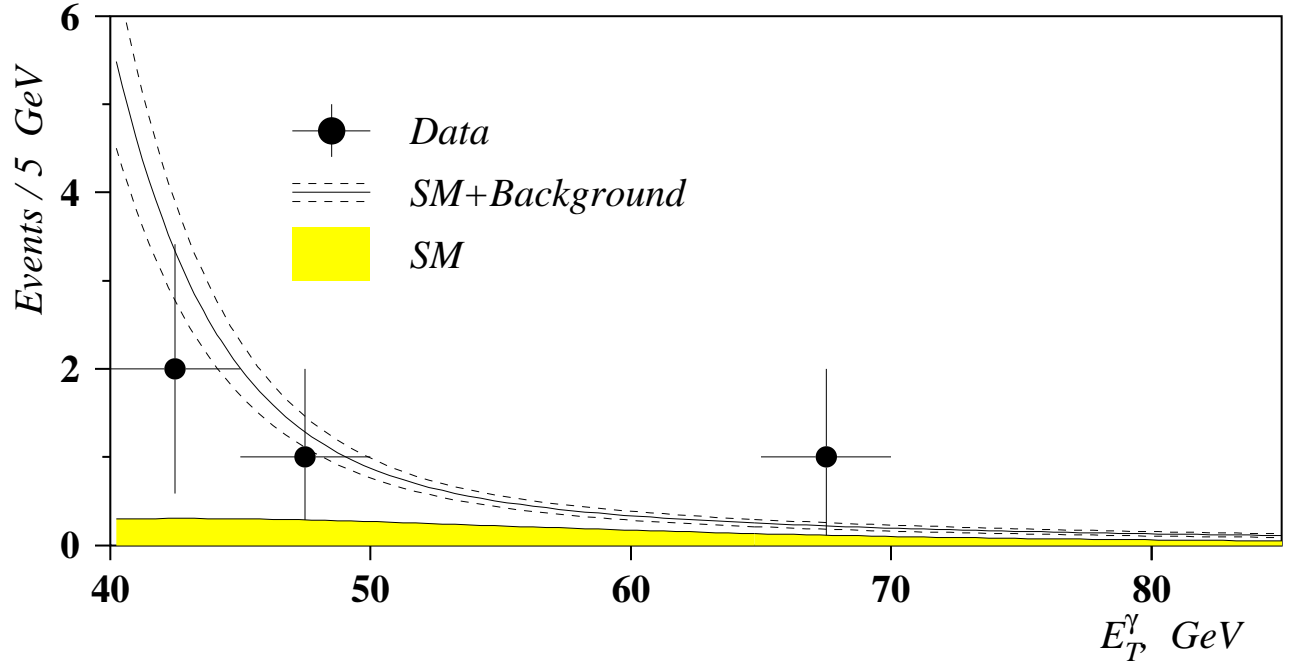


FIG. 37. The photon  $E_T$  spectra for the  $Z\gamma \rightarrow \nu\nu\gamma$  data (points), the background (solid line), the expected signal (shaded), and the sum of the expected signal and background with uncertainties (dotted).

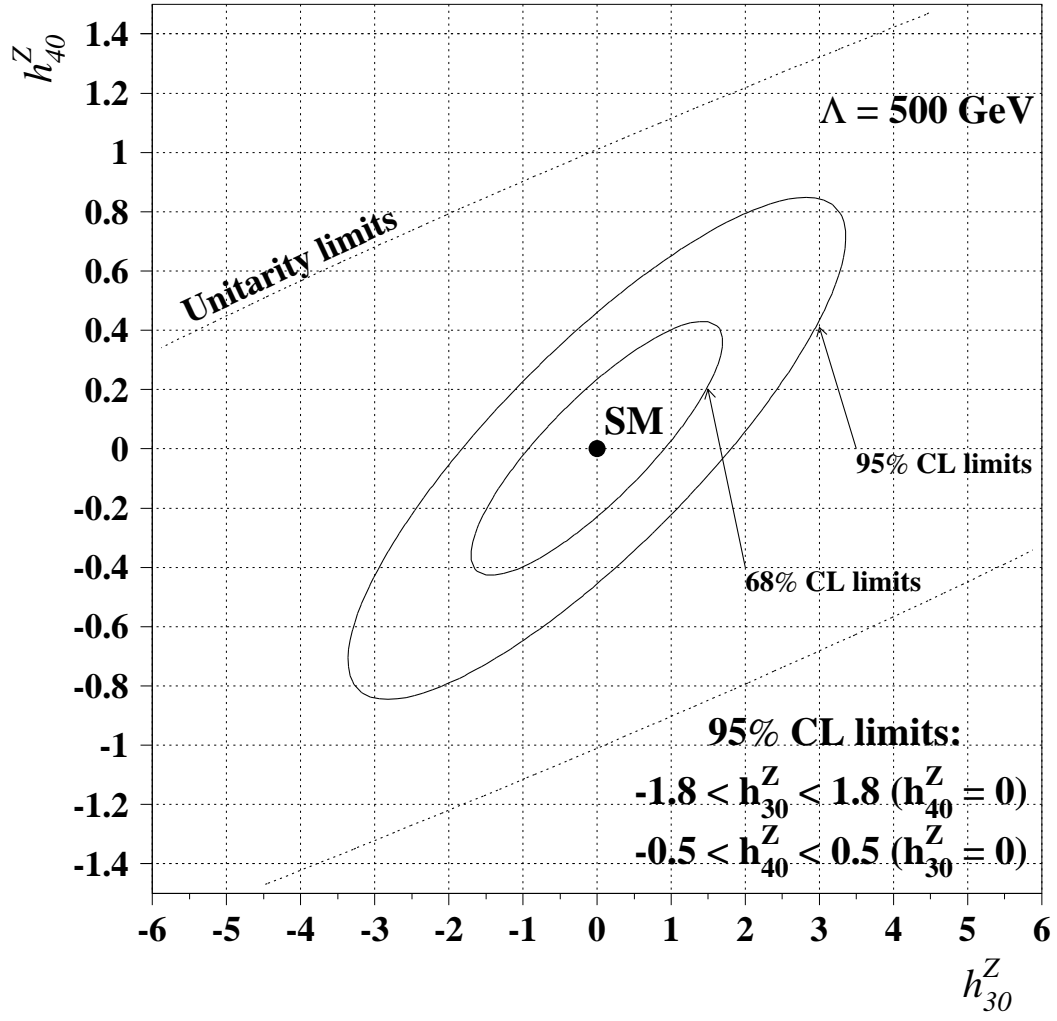


FIG. 38. Limits on the  $CP$ -conserving anomalous  $ZZ\gamma$  coupling parameters  $h_{30}^Z$  and  $h_{40}^Z$ . The solid ellipses represent 68% and 95% CL exclusion contours for the  $ee$  and  $\mu\mu$  combined analysis. The dashed curve shows limits from partial wave unitarity for  $\Lambda = 500 \text{ GeV}$ .

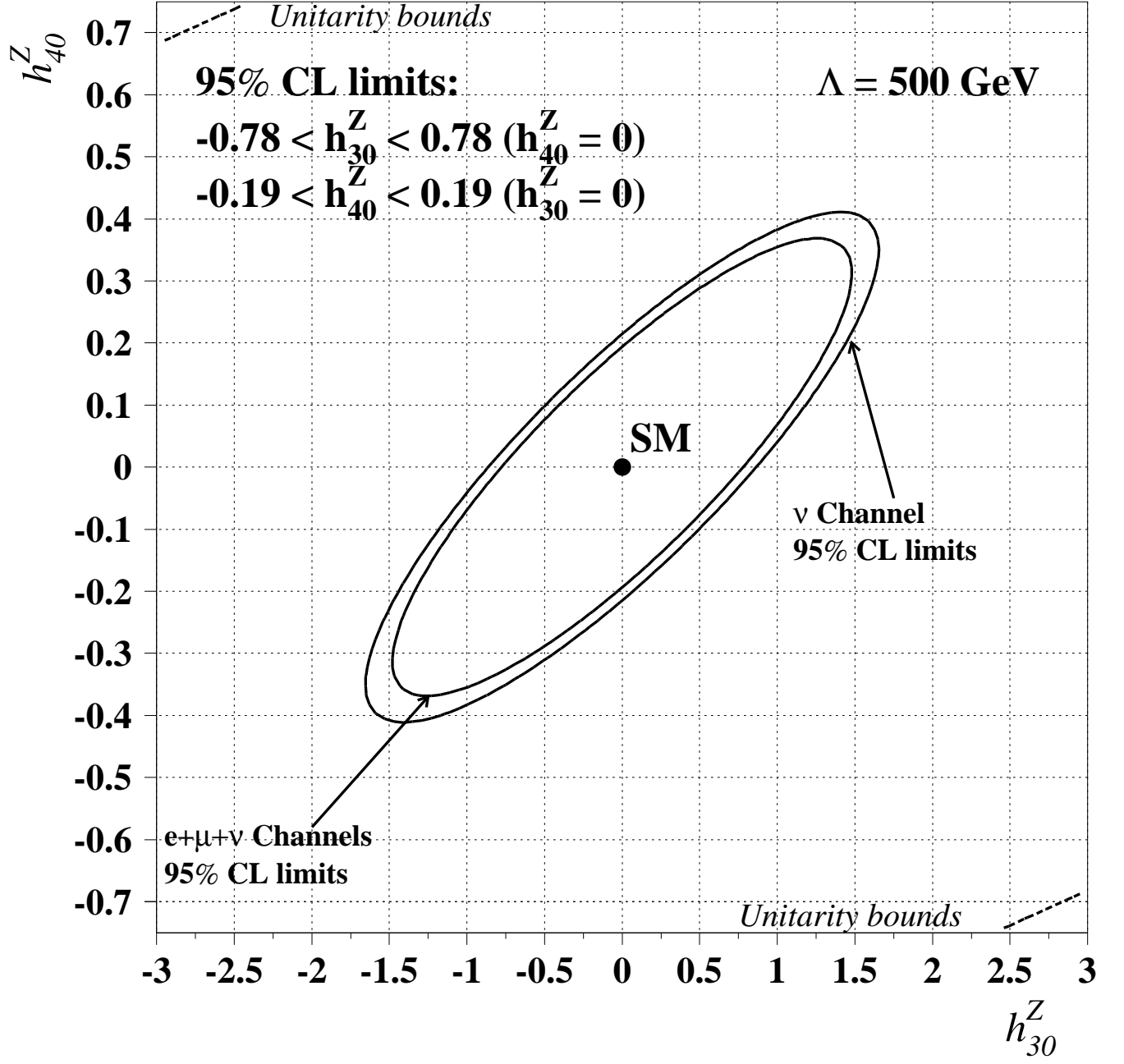


FIG. 39. Limits on the  $CP$ -conserving anomalous  $ZZ\gamma$  coupling parameters  $h_{30}^Z$  and  $h_{40}^Z$ . The solid ellipses represent the 95% CL exclusion contours for the  $\nu\bar{\nu}$  and for combined  $ee$ ,  $\mu\mu$ , and  $\nu\bar{\nu}$  analyses. The dashed curve shows limits from partial wave unitarity for  $\Lambda = 500$  GeV.

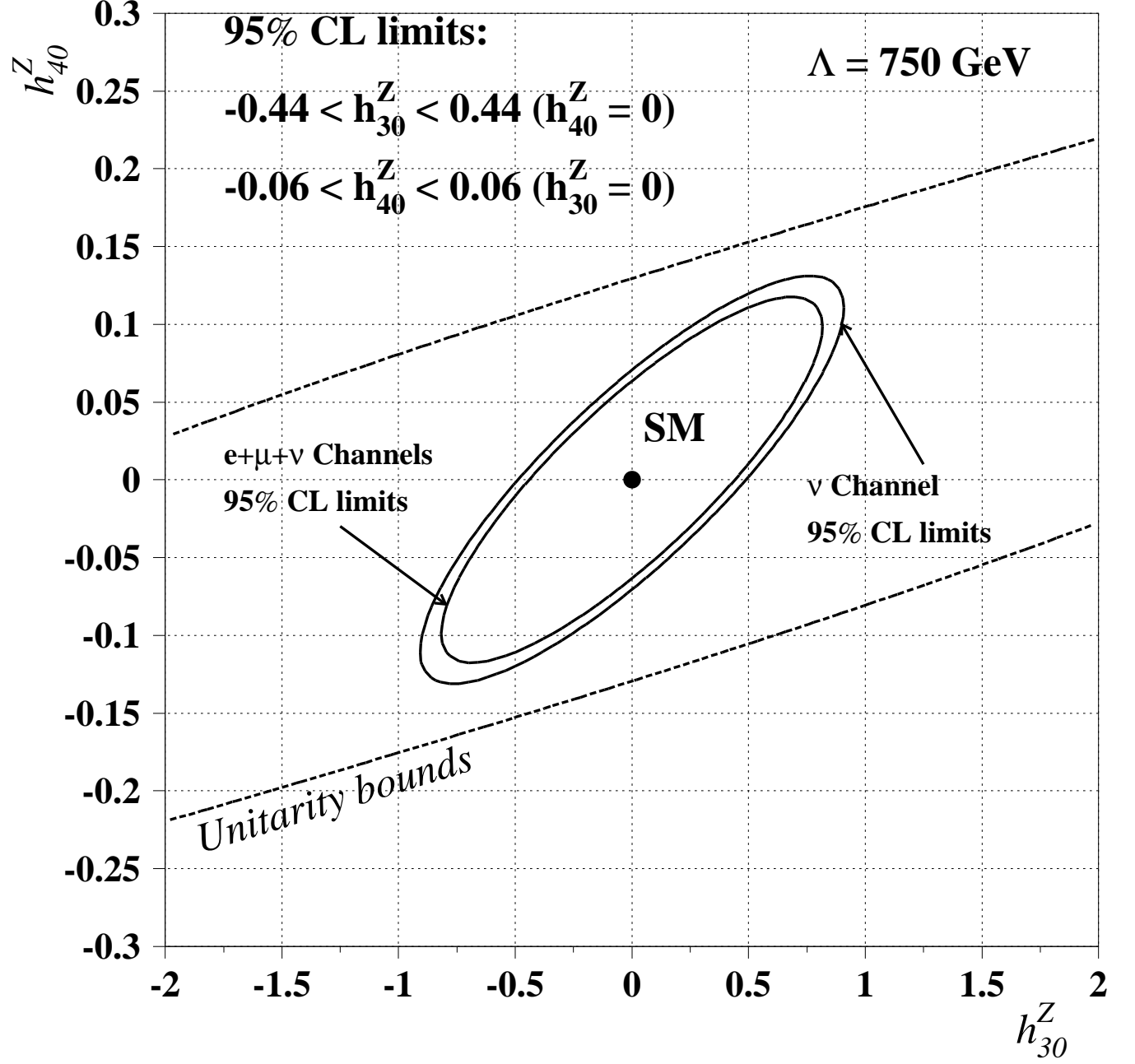


FIG. 40. Limits on the  $CP$ -conserving anomalous  $ZZ\gamma$  coupling parameters  $h_{30}^Z$  and  $h_{40}^Z$ . The solid ellipses represent the 95% CL exclusion contours for the  $\nu\bar{\nu}$  and for the combined  $ee$ ,  $\mu\mu$ , and  $\nu\bar{\nu}$  analysis. The dashed curve shows limits from partial wave unitarity for  $\Lambda = 750 \text{ GeV}$ .